To The Graduate Counsil:

I am submitting herewith a dissertation written by Panagiotis G. Datskos entitled "Effect of temperature and density on electron attachment and ionization processes". I have examined the final copy of this dissertation for form and content and recommend that it be accepted in partial fulfillment for the degree of Doctor of Philoshophy, with a major in Physics.

L. G. Christophorou

L. G. Christophorou, Major Professor

We have read this dissertation
and recommended its acceptance

J. Jellison

Marshall Pace

John Georghiou

Accepted for the Counsil:

Lew Minkel

Vice Provost
and Dean of The Graduate School

EFFECT OF TEMPERATURE AND DENSITY ON ELECTRON ATTACHMENT AND IONIZATION PROCESSES

A Dissertation

Presented for the

Doctor of Philosophy

Degree

The University of Tennessee, Knoxville

Panagiotis George Datskos

December 1988

Acknowledgments

The author wishes to express his gratitude to Professor L. G. Christophopou for his aid and guidance throughout the entirety of this research.

Thanks are also extended to Dr. S. R. Hunter, Dr. H. Faidas, and to Mr. J. G. Carter for valuable assistance.

The author acknowledges his appreciation to the Physics Department of The University of Tennessee, Knoxville, for a teaching assistantship throughout the years of his graduate studies and to the Health and Safety Research Division of Oak Ridge National Laboratory for providing the facilities and support for this work.

It is with a deep debt of gratitude that the author thanks his wife for her understanding and invaluable help.

Abstract

The total electron attachment rate constant $k_a(\langle\epsilon\rangle, T)$ for $n-C_4F_{10}$ and for $n-C_6F_{14}$ has been measured in a buffer gas of Ar using an electron swarm technique in the mean electron energy range, $\langle\epsilon\rangle$, 0.41 to 4.81 eV, over the temperature range, T, 300 to 750 K and over the total gas number density, N_t, 2.25 to 12.88 $\times 10^{19}$ $molecules/cm^3$. The measured $k_a(\langle\epsilon\rangle, T)$ and the total electron attachment cross section $\sigma_a(\epsilon, T)$ obtained from them are reported and discussed. The $k_a(\langle\epsilon\rangle, T)$ for $n-C_4F_{10}$ first decrease slowly with T between 300 to 400 K then decrease precipitously between 400 and $\approx$ 500 K and subsequently increase for $T \geq 500$ K. The $k_a(\langle\epsilon\rangle, T)$ for $n-C_6F_{14}$ initially increase slowly with T between 300 and 400 K, then decrease precipitously between 400 and $\approx$ 550 K and subsequently decrease for $T \geq 550$ K. For both molecules the overall variation of $k_a(\langle\epsilon\rangle, T)$ with T depends on $\langle\epsilon\rangle$ and was independent of N_t except for $n-C_4F_{10}$ which exhibits an increase with N_t for $T \leq 500$ K. From the measured dependence of $k_a(\langle\epsilon\rangle, T)$ for $n-C_4F_{10}$ on N_t and T the contribution of the nondissociative and dissociative electron attachment to $k_a(\langle\epsilon\rangle, T)$ was determined as a function of $\langle\epsilon\rangle$. From the analysis of these results the effect of temperature on nondissociative electron attachment was quantified.

The total electron attachment rate constant $k_a(\langle\epsilon\rangle, T)$ for SO_2F_2 in N_2 has been measured as a function of $\langle\epsilon\rangle$ (0.046 to 0.911 eV), temperature (300 to 700 K) and total gas number density (2.25 to 6.44 $\times 10^{19}$ $molecules/cm^3$). From the measured $k_a(\langle\epsilon\rangle, T)$ the $\sigma_a(\epsilon, T)$ were determined. At $T = 300$ K the $\sigma_a(\epsilon, T)$ exhibits a maximum at ≈ 0.22 eV which is due to dissociative electron attachment and an increase below ≈ 0.1 eV which is due to the formation of parent anions

at near zero energies. At $T = 400\ K$ the $\sigma_a(\epsilon, T)$ posseses only one main peak at $\approx 0.13\ eV$ which shifts to lower ϵ with increasing T so that at 700 K the peak is located at $\approx 0.03\ eV$. The value $\sigma_a(\epsilon_{max}, T)$ of $\sigma_a(\epsilon, T)$ at the peak increases by a factor of 32 as T increases from 300 to 700 K. The analysis of the present results and earlier similar work leads to the conclusion that the increase of the dissociative electron attachment with temperature is due to the increase of the internal energy (principally vibrational) of the molecule.

The ionization onset, I_f, for TMPD (N,N,N′,N′-tetramethyl-p-phenylenediamene) molecules in ethane has been measured for the first time in the number density, N, range 0.09 to $8.01 \times 10^{21}\ molecules/cm^3$ and over the temperature T range 293 to 413 K, using a multiphoton ionization conductivity technique. The I_f was found to depend on both N and T in the ranges studied. At a fixed $T(= 373K)$, I_f was found first to decrease with increasing N and then to level off at number densities of $\approx 5.96 \times 10^{21}\ molecules/cm^3$. For $N \geq 6.84 \times 10^{21}\ molecules/cm^3$ and $T = 293\ K$ the I_f was found to increase with increasing number density. At a constant number density ($N = 3.55 \times 10^{21}\ molecules/cm^3$) I_f decreased with increasing T between 323 and 413 K.

Contents

List of Tables

List of Figures

Chapter 1

Introduction

1.1 General Considerations

The interaction of low-energy (0 - 10 eV) electrons with atoms and molecules has been of great interest, for reasons both fundamental and practical, over the past twenty five years. The intense recent activity has resulted in new advances which enriched the knowledge on the structure of matter, and accelerated the advancement of broad areas of physics, chemistry, and biology. It also opened up new possibilities for applications in many fundamental areas of technology and energy, radiation sciences, electrical engineering, the space, the atmosphere, and the environment (Christophorou and Hunter, 1984). The existing literature in this field is voluminous. A detailed treatment of the various aspects of the subject may be found in the recent review by Christophorou (1984).

The collision between a low energy (0 - 10 eV) electron and a molecule (or atom) may lead to the formation of a negative ion. Negative ions are of intrinsic physical interest in that they can provide basic information on atoms and molecules (*e.g.*, molecular structure, electron affinities and bond dissociation energies). In chemistry, negative ions are important intermediates in radiation-induced reactions. In biology, they play a basic role in clarifying concepts used in theoretical treatments of biological action of molecules.

The interaction of a photon with an atom or molecule may result in the formation of a positive ion and an electron (ionization of the species), or in the

electronic excitation of that species. When more than one photon is required for this to occur then multiphoton ionization (MPI) or multiphoton excitation (MPE) processes take place. The probability of MPI or MPE processes to happen compared to single-photon processes is so low, that it will be significant and observable only at very high photon fluxes.

The study of the ionization mechanism and the determination of the ionization threshold of a molecule (or atom) in different environments, provide information about the effect that the medium has on charge-separated states (*i.e.*, electron-ion pairs, free and quasi-free electrons, Rydberg states, positive and negative ions).

Knowledge of how the properties of an isolated molecule (or atom) change as it finds itself in different environments and under different thermodynamic conditions is an important step in the effort to link physics and chemistry and both with biology (Christophorou and Siomos, 1984).

In the ensuing sections, a brief outline of the electron attachment processes will be given with an emphasis on energy rich ("hot") molecules and the importance of negative ion studies will be highlighted. Also processes that can lead to creations of charge-seperated states are discussed with emphasis on multiphoton ionization of molecules in media that range from dilute gases to dense gases to supercritical gases and finally to liquid-phase environments.

1.2 Electron Attachment Processes to "Hot" Molecules

1.2.1 Modes of Production of Negative Ions

Molecules can attach free electrons in both the gaseous and the condensed phase. The lifetime of these can range from 10^{-15} to $10^{-2}s$ (Christophorou, 1978), and their formation processes strongly depend on the environment (Christophorou and Siomos, 1984).

Molecules capture free electrons through electron attachment proceses such as (Christophorou *et al.*, 1984): resonance free-electron attachment (Christophopou,

1971), ion-pair formation (Christophorou, 1971; Massey, 1976), free-electron capture by dipolar molecules (Christophorou *et al.*, 1984; Lane, 1980), free-electron capture by molecular clusters (Wegener, 1974) and bound electron capture by molecules (Christophorou *et al.*, 1984).

Resonance free-electron attachment to molecules occurs essentially in two different ways: (a) dissociatively and (b) nondissociatively. The basic dissociative and nondissociative processes through which fragment and parent negative ions are formed (in a collision of a molecule with a low energy electron) take place via Negative Ion Resonance States (NIRSs), which are nonstationary states, for the electron-molecule system, such as (Christophorou *et al.*, 1984): shape or single-particle resonances, core-excited shape resonances (type II), nuclear-excited Feshbach resonances and electron-excited Feshbach resonances. The resonance electron attachment processes (a) and (b) may be classified according to the internal state of excitation of the electron capturing molecule as (Christophorou, 1980; Christophorou *et al.*, 1984): free electron attachment to ground state molecules, free electron attachment to "hot" (rotationally and/or vibrationally excited) molecules and free electron attachment to electronically excited molecules.

Electron attachment processes for a molecule $ABCD$ are profoundly affected by increases in the internal energy of the electron capturing species. At elevated temperatures, a fraction of the total number of molecules $ABCD$ in the ground electronic state is in higher rotational, j, and/or vibrational, v, states. The interaction of a slow electron $e(\epsilon)$, of energy ϵ, with a molecule $ABCD(G; v \geq 0; j \geq 0)$ in its ground electronic state G, in the vibrational state v, and in the rotational state j, may be considered as proceeding through the formation of a transient negative ion $ABCD^{-*}(G \text{ or } E;\ v' \geq 0; j' \geq 0)$, in either the ground or an excited electronic state, possessing some vibrational ($v' \geq 0$) and some rotational ($j' \geq 0$) excitation, with an electron capture cross section $\sigma_c^{v'j}(\epsilon)$. This formation of $ABCD^{-*}$ and the ensuing channels may be represented as (Christophorou, 1980; Christophorou *et*

al., 1984):

$$e(\epsilon)+ABCD(G;v>0;j>0) \underset{\tau_a^{-1}}{\overset{\sigma_c^{v,j}(\epsilon)}{\rightleftharpoons}} ABCD^{-*}(G \text{ or } E;v'>0;j'>0)$$

$$\xrightarrow{p_1} ABCD + e(\epsilon) \tag{1.1}$$

$$\xrightarrow{p_2} ABCD^{(*)} + e(\epsilon') \tag{1.2}$$

$$\xrightarrow{p_3} AB^{(*)} + CD^- \tag{1.3a}$$

$$ABC^{(*)} + D^- \tag{1.3b}$$

$$AB^{(*)} + CD^{-*} \longrightarrow CD^{(*)} + e \tag{1.3c}$$

$$\longrightarrow C^{(*)} + D^- \tag{1.3d}$$

$$\xrightarrow{p_4} ABCD^- + \text{energy} \tag{1.4}$$

where $\sigma_c^{v,j}(\epsilon)$ is the cross section for formation of the transient anion $ABCD^{-*}$, τ_a^{-1} is the rate constant for $ABCD^{-*}$ to decay by autodetachment and p_1, p_2, p_3, p_4 are the probabilities for $ABCD^{-*}$ to decay to the corresponding channels. The asterisk indicates excess internal energy and the asterisk in parenthesis indicates possible increase in the internal energy of the corresponding species, and $\epsilon'(\leq \epsilon)$ is the energy of scattered electron. Reactions (1.1) and (1.2) represent respectively indirect elastic and inelastic scattering of the electron by the molecule $ABCD$. Reactions (1.3) are classified as dissociative electron attachment, leading to stable fragment negative ions and for a polyatomic molecule this reaction can lead to simultaneous multiple fragmentation. Reactions (1.3c) and (1.3d) represent dissociative electron attachment processes which can lead to metastable negative ion fragments which may autodetach the electron and/or autodissociate. And the reaction (1.4) represents parent anion formation which can occur when the electron affinity of $ABCD$ is greater than zero ($EA \geq 0$). (The electron affinity, EA, of a

molecule is defined as the energy difference between the neutral molecule plus an electron at rest at infinity, and the molecular negative ion, when both are in their lowest excitation state). The excess internal energy of the transient parent negative ion $ABCD^{-*}$ must be removed, usually by a collision with another molecule or atom, so that the transient anion can relax into a lower, stable (with respect to autoionization), state. The cross section for the formation of the transient negative ion $ABCD^{-*}(G \text{ or } E;\ v' \geq 0, j' \geq 0)$ and the probability of the ensuing channels are profoundly affected by the vibrational and rotational quantum states accessed by the molecule (see next subsection).

The electronic motion in a molecule is much faster than the nuclear motion, and therefore it is possible to express the molecular wavefunction (in the Born-Oppenheimer approximation) as a product $\Psi(\mathbf{r},\mathbf{R}) = \phi(\mathbf{r},\mathbf{R})\xi(\mathbf{R})$, combining both the electronic coordinate $\mathbf{r}$ and the nuclear coordinate $\mathbf{R}$ (Oppenheimer, 1928; Hasted and Mathur, 1984). This enables the application of the Franck-Condon principle in electron attachment processes (Christophorou *et al.*, 1984). These processes are then permitted to proceed by vertical transitions between potential energy curves (surfaces) from the equilibrium position of the molecules. In Fig. 1.1 are illustrated schematically for a diatomic (or diatomic-like) molecule, the resonance nondissociative and dissociative electron attachment processes. The magnitude, energy dependence and shape of cross section for these processes provide useful information about the negative ion state(s) of AX^- (Christophorou *et al.*, 1984).

1.2.2 Dissociative and Nondissociative Electron Attachment and the Effect of Temperature on them

A number of authors (*e.g.*, Bardsley *et al.*, 1964, 1966; O'Malley, 1966; Chen, 1967; Chen and Peacher, 1967) have treated the dissociative electron attachment to diatomic molecules within the resonance electron scattering formalism. The application of this theory, however, to electron attachment to polyatomic structures is only possible when these polyatomic molecules can be considered as "diatomic-like"

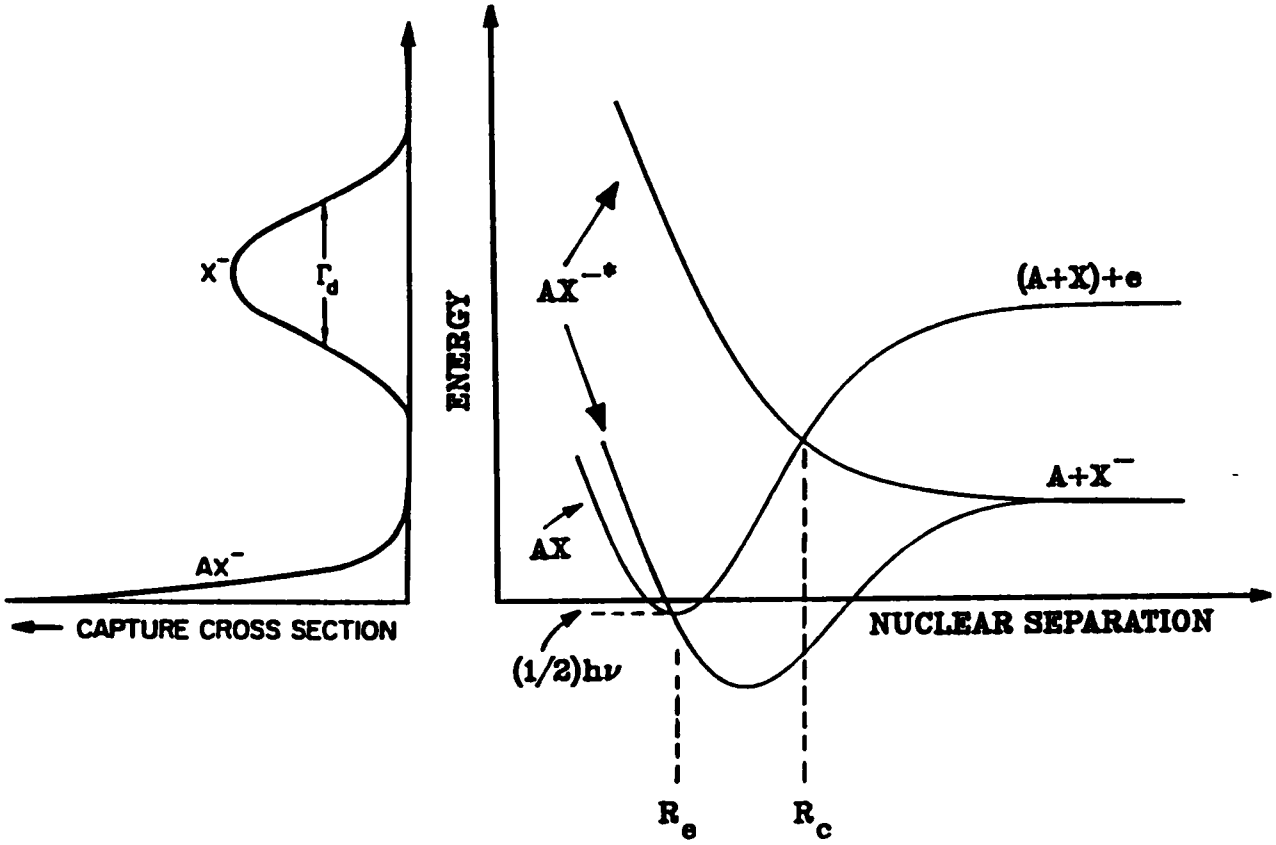

Figure 1.1: Schematic diagram illustrating the resonance nondissociative and dissociative electron attachment processes and the dependencies of their respective electron attachment cross section on the electron energy. (From Christophorou *et al.*, 1984.)

molecules. Within the scope of this theory the cross section $\sigma_{da}(\epsilon)$ for dissociative electron attachment as a function of the electron energy, ϵ, may be presented as

$$\sigma_{da}(\epsilon) = \sigma_c'(\epsilon)p'(\epsilon) \tag{1.5}$$

where $\sigma_c'(\epsilon)$ is the cross section for capture of an electron by the molecule leading into the metastable negative-ion state and $p'(\epsilon)$ is the probability that the transient anion will decay by stable negative-ion fragments (dissociative attachment). O'Malley (1966) has calculated an expression for $\sigma_{da}(\epsilon)$ for the case of a diatomic molecule AX initially in a vibrational level (v) with a purely repulsive negative-ion state AX^{-*} (upper curve in Fig. 1.1) given by O'Malley (1966)

$$\sigma_{da}^{v}(\epsilon) = \frac{4\pi^2\overline{g}}{k^2}\frac{\Gamma_{aX}}{\Gamma_d}\left|\overline{\chi}_v(R_\epsilon)\right|^2 \mathrm{e}^{-\rho(\epsilon)} \tag{1.6}$$

with

$$\sigma_c'(\epsilon) = \frac{4\pi^2\overline{g}}{k^2}\frac{\Gamma_{aX}}{\Gamma_d}\left|\overline{\chi}_v(R_\epsilon)\right|^2 \tag{1.7}$$

and,

$$p'(\epsilon) = \mathrm{e}^{-\rho(\epsilon)} \tag{1.8}$$

In Eqn 1.7, $\overline{g}$ is a statistical factor, k is the electron wavenumber, Γ_a is the total autodetachment width, $\Gamma_{a,X}$ is the partial autodetachment width for the state X, Γ_d is the dissociative electron attachment resonance width and $\overline{\chi}_v(R)$ is the initial vibrational wave function which corresponds to the level v evaluated at the internuclear distance R_ϵ at which electrons of energy ϵ can reach the negative ion state. The quantity $p'(\epsilon)$ has been defined explicitly by many authors (see for example, Chen, 1966; O'Malley, 1966) as

$$p'(\epsilon) = \exp\left(-\int_{R_\epsilon}^{R_c} dR\frac{\Gamma_a(R)}{\hbar v(R)}\right) \simeq \mathrm{e}^{-\frac{\tau_s}{\tau_a}} \tag{1.9}$$

and is the probability that AX^{-*} will not autoionize while separating from the point of formation at an internuclear distance R_ϵ to the point at an internuclear distance R_c where the potential energy curves of AX and AX^- cross (see Fig 1.1). The time needed for AX^{-*} to separate from R_ϵ to R_c is

$$\tau_s = \int_{R_\epsilon}^{R_c}\frac{dR}{v(R)} \tag{1.10}$$

where $v(R)$ is the relative velocity of separation of A and X^- and $\overline{\tau}_a$ is the mean autoionization lifetime of AX^{-*}.

The effect of temperature on the dissociative electron attachment cross section is usually an increase in σ_{da} (Compton *et al.*, 1966; Chantry 1969; Henderson *et al.*, 1969; Warman and Sauer, 1971; Warman *et al.*, 1972; Spence and Schultz, 1973; Brooks *et al.*, 1979; Shimamori and Fessenden, 1979; Christophorou, 1980; Alge *et al.*, 1984; Smith *et al.*, 1984; Christophorou *et al.*, 1984; Spyrou and Christophorou, 1985a, 1985c). This increase is mainly due to the decrease with T of the separation time τ_s (see Eqn. 1.3). As T increases the threshold energy decreases, the energy position of the resonance maximum cross section decreases, while the magnitude of the cross section and the resonance width increase.

Similarly the nondissociative electron attachment cross section $\sigma_{nda}(\epsilon)$ for a molecule AX as a function of the electron energy ϵ may be represented by

$$\sigma_{nda}(\epsilon) = \sigma_c(\epsilon)p(\epsilon) \tag{1.11}$$

In Eqn. 1.11 $\sigma_c(\epsilon)$, $p(\epsilon)$ are respectively the cross section for formation of the transient negative ion AX^{-*} and the probability that it will be stabilized into AX^-.

The incident electron $e(\epsilon)$ may be captured into any of the vibrational levels of AX^{-*} which lie above the initial state of AX. Using v to denote the v^{th} vibrational level and ℓ for the orbital angular momentum and spin of the electrons, the contibution of the level $v\ell$ at energy $E_{v\ell}$ to the scattering cross section, from an initial channel $a\alpha$ to a final $b\beta$ is given by the Breit-Wigner formula (Blatt and Weisskopf, 1952; Herzenberg, 1969; Mott and Massey, 1971; Landau and Lifshitz, 1977)

$$\sigma_{v\ell}(\epsilon; a\alpha; b\beta) = \frac{4\pi}{k^2} \frac{\Gamma_{v\ell}^{a\alpha}\Gamma_{v\ell}^{b\beta}}{((\epsilon - E_{v\ell})^2 + (\Gamma_{v\ell}/2)^2)} \tag{1.12}$$

where k is the electron wave number, $\Gamma_{v\ell}^{a\alpha}$ is the partial width for the channel $a\alpha$, $\Gamma_{v\ell}^{b\beta}$ is the partial width for channel $b\beta$, $\Gamma_{v\ell}$ is the total width of the resonance, and α, β are respectively the initial and the final spin of the electron. Then the cross section for formation of all the intermediate states with vibrational number

v, arising from the initial channel a is obtained by summing over the final channels $b\beta$, averaging over all the initial spins α, multiplying by the number g of the degenerate resonances corresponding to the level v and dividing by the number S of spin states of the incident electron, viz.,

$$\sigma_v(\epsilon, a) = \frac{4\pi}{k^2}\frac{g}{S}\frac{\Gamma_v^a \Gamma_v}{((\epsilon - E_v)^2 + (\Gamma_v/2)^2)} \tag{1.13}$$

The cross section for the formation of the transient anion is then given by

$$\sigma_c(\epsilon) = \int_0^\infty dR \sigma_v(\epsilon, a) \left|\chi_v(R)\right|^2 \tag{1.14}$$

hence

$$\sigma_{nda}^v(\epsilon) = \frac{4\pi}{k^2}\frac{g}{S}\left(\int_0^\infty dR \frac{\left|\chi_v(R)\right|^2 \Gamma_v^a \Gamma_v}{((\epsilon - E_v)^2 + (\Gamma_v/2))}\right) p(\epsilon) \tag{1.15}$$

gives the nondissociative electron attachment cross section.

The effect of temperature on the nondissociative electron attachment cross section is usually a decrease in σ_{nda} with increasing T (Hunter *et al.*, 1983; Hernandez-Gil *et al.*, 1984; Christophorou, 1985; Adams *et al.*, 1985; Christophorou *et al.*, 1987; Spyrou and Christophorou, 1985b; Datskos and Christophorou, 1987) which is a result of a decrease in $p(\epsilon)$ and/or $\sigma_c(\epsilon)$. The decrease in $p(\epsilon)$ results mainly from a decrease of the mean autodetachment lifetime τ_a with increasing T (see Chapter 3).

The direct effect of the temperature on a molecule AX is to produce a Maxwellian distribution of vibrational (v) and rotational (j) states (O'Malley, 1967). The effective electron attachment cross section $\sigma_a(\epsilon, T)$ then is the Boltzmann average of the cross section $\sigma_a^{v,j}(\epsilon)$ from each of the individual states, (Christophorou *et al.*, 1984) viz.,

$$\sigma_a(\epsilon, T) = \sum_v^\infty \sum_j^\infty Z \mathrm{e}^{-(E_v + E_j)/kT} \sigma_a^{v,j}(\epsilon) \tag{1.16}$$

where

$$Z = \left(\sum_v^\infty \sum_j^\infty \mathrm{e}^{-(E_v + E_j)/kT}\right)^{-1} \tag{1.17}$$

1.3 Multiphoton Ionization Processes

1.3.1 Multiphoton Ionization Mechanisms

The first work on multiphoton processes can be traced back in the beginning of quantum theory, when a theoretical analysis of a two-photon absorption was published by Goeppert-Mayer[a] in 1931. When multiphoton ionization processes take place in an atom or molecule which has an ionization threshold I, that species can be ionized by absorbing a number of photons,each photon having an energy $h\nu$ much less than its ionization potential, provided that the photon flux is high enough. Such conditions can usually be achieved with laser radiation. Mechanisms of MPI have been described earlier in the gaseous phase (Chin and Lambropoulos, 1984) and in the liquid-phase (Faidas and Christophorou, 1988b).

In Fig. 1.2 some of the mechanisms that describe MPI processes are shown schematically. In case (a), a direct three-photon nonresonant ionization is represented, using as an example the ionization of a molecule (or atom) through the absorption of three photons each of energy $h\nu$. Case (b) describes a resonant photoionization process (with a two-photon excitation followed by ionization with the absorption of a third photon) which occurs when a molecular (or atomic) state is located close to a laser-induced virtual state. It is interesting to note that in this case the MPI processes take place at lower laser intensities. In case (c) a situation similar to the previous one is shown where the molecule is excited by absorption of two photons to a short lived singlet state S. But unlike case (b) the ensuing ionization of the species is proceeding through ionization from a lower lying "longer lived" with respect to the laser pulse duration, singlet state, S'.

Multiphoton ionization has been proven to be a very sensitive technique (Faidas, 1985) in both the gas (Boesl *et al.*, 1981) and in the liquid-phase (Christophorou and Siomos, 1984), which among other information provides direct estimates on the ionization onsets of atoms and molecules. It is very important (but many

[a]This analysis was later employed by Breit and Teller (1940) to claculate the mean lifetime of the $2s$ state of hydrogen which was estimated to be $\approx 1/7\ s$

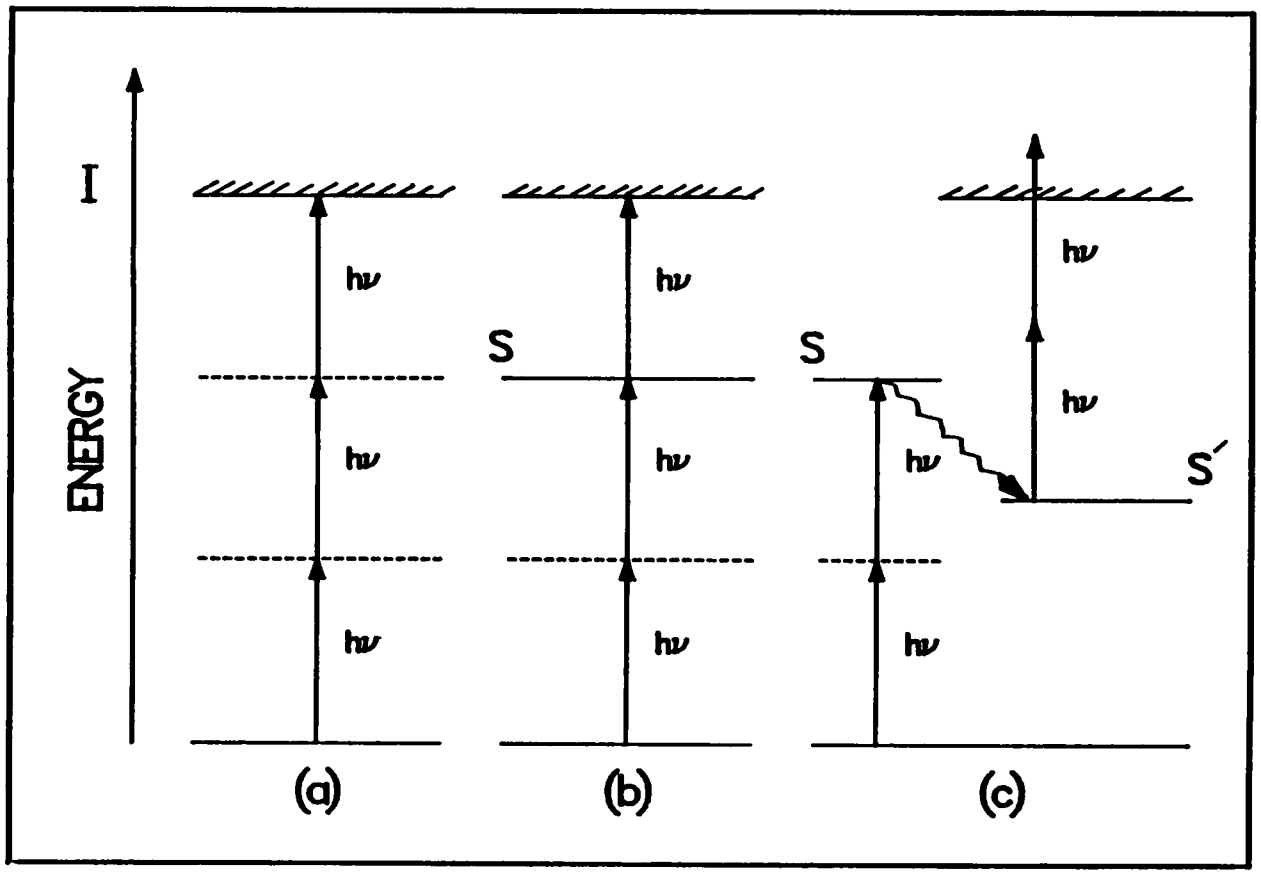

Figure 1.2: Schematic illustration of different ionization pathways. (a) Direct three-photon nonresonant ionization, (b) three-photon resonant, one-photon ionization, (c) stepwise four-photon ionization cosisting of two-photon resonant, two-photon ionization via a lower-lying state S′.

times not an easy task when dealing with MPI processes), to identify the mechanism through which the ionization proceeds and to determine the order of the MPI process (*i.e.*, the number of photons absorbed during the process). The intensity I_{in} of the light incident on a molecule (or atom) inside a medium is a function of the position $\mathbf{r}$ where the species is located, as well as of the time t, and it can be described as (Crance, 1984)

$$I_{in}(\mathbf{r},t) = I_\ell f(\mathbf{r}) g(t) \tag{1.18}$$

where I_ℓ is defined as the maximum value of the intensity with respect to space and time so that the functions $f(\mathbf{r})$ and $g(t)$ are dimensionless and can take values between 0 and 1. The probability for the molecule or atom to be ionized absorbing n photons is given by (Crance, 1984)

$$\begin{aligned} P_{ionization} &= 1 - \exp\left[-\int_{-\infty}^{\infty} \sigma_n \left(I_\ell f(\mathbf{r}) g(t)\right)^n dt\right] \\ &= 1 - \exp\left[-\sigma_n f^n(\mathbf{r}) \tau_n I_\ell^n\right] \simeq \sigma_n f^n(\mathbf{r}) \tau_n I_\ell^n \end{aligned} \tag{1.19}$$

where

$$\tau_n = \int_{-\infty}^{\infty} g^n(t) dt \tag{1.20}$$

In Eqn 1.19, σ_n is the $n-$photon transition probability, (which in the *c.g.s.* system is expressed in units of $cm^{2n} \cdot s^{n-1}$). The number of charges created directly (electrons, positive ions) by a light pulse is

$$\begin{aligned} N &= N_0 \int \left(1 - \mathrm{e}^{-\sigma_n I_\ell^n f^n(\mathbf{r}) \tau_n} d^3\mathbf{r}\right) \\ &\approx N_0 \sigma_n \tau_n \left(\int f^n(\mathbf{r}) d^3\mathbf{r}\right) I_\ell^n \end{aligned} \tag{1.21}$$

Hence

$$N = N_0 \sigma_n \tau_n V_n I_\ell^n \tag{1.22}$$

where

$$V_n = \int f^n(\mathbf{r}) d^3\mathbf{r} \tag{1.23}$$

Then the mean ionization signal which is proportional to the number of charge carriers created per light pulse of wavelength λ is

$$I_s(\lambda) = (AN_0\sigma_n\tau_n V_n)\, I_\ell^n \tag{1.24}$$

or

$$I_s(\lambda) = C(\lambda) \cdot I_\ell^n \tag{1.25}$$

where $C(\lambda)$ is a quantity which includes the yield for ion-electron pair production following the ionization. From the knowledge of the ionization signal versus the laser intensity at a fixed wavelength the order n of the MPI process can be determined through the relation 1.25 (see Chapter 2)

1.3.2 Dependence of the Ionization Threshold on the Density and the Temperature

The threshold energy, I_f, which is required to ionize an atom or molecule embedded in a dielectric medium with a number density N and at temperature T may be represented as (Holroyd, 1972; Christophorou and Siomos, 1984)

$$I_f = I_g + V_0 + P^+ \tag{1.26}$$

where I_g is the ionization threshold of the molecule in the gas phase, V_0 is the ground state energy (bottom of the conduction band) of the excess electron in the medium and P^+ is the medium polarization energy (which is always negative) due to the creation of the positive ion. The expression 1.26 was first used by Lyons (1957) in his effort to understand the photoconductance in organic crystals. Since then many authors have verified the correctness of Eqn 1.26 (see for example Faidas and Christophorou, 1988a). The understanding of the effect that the medium has on the ionization onset, I_f, can be realized on the basis of the dependence of the V_0 and P^+ on changes in the environment (such as changes in the density, temperature, pressure).

The ground state energy of an excess electron in a fluid can be calculated by adopting the Wigner-Seitz model (Wigner and Seitz, 1933; Springett *et al.*, 1968).

In a fluid of density N, a spherical Wigner-Seitz (W-S) cell is constructed around the molecule of the fluid, which is situated at $\mathbf{r} = 0$. This cell would have a radius r_s given by

$$r_s = \left(\frac{3}{4\pi N}\right)^{1/3} \tag{1.27}$$

The ground state energy V_0 can then be calculated by solving for the lowest eigenvalue of the Schrödinger equation in the W-S cell viz.,

$$\left(-\frac{\hbar^2}{2m_e}\right)\nabla^2\psi_k(\mathbf{r}) + U(\mathbf{r})\psi_k(\mathbf{r}) = E_k\psi_k(\mathbf{r}) \tag{1.28}$$

where $U(\mathbf{r})$ is the potential with which the excess electron interacts in the cell and the wavefunction $\psi_k(\mathbf{r})$ is subject to the boundary condition

$$\left.\frac{\partial\psi_k(\mathbf{r})}{\partial r}\right|_{r=r_s} = 0 \tag{1.29}$$

which is required for the continuity of the wavefunction on the surface of the W-S sphere (Shimoji, 1977; Kittel, 1977).

The one-electron potential $U(\mathbf{r})$ is considered to be the superposition of the Hartree-Fock potential (due to the charge distribution in the molecule), the electron-molecule polarization potential and the mean (screened) potential produced by the interaction of the electron with molecules outside the cell, which are distributed with a density $Ng(r')$ at position $\mathbf{r}'$. The quantity $g(r')$ is the pair distribution function of the fluid and is a measure of the probability of finding in the fluid two molecules at a distance r from each other. Then the potential can be written as (Springett *et al.*, 1967)

$$U(\mathbf{r}) = U_{HF}(\mathbf{r}) + U_{pol}(\mathbf{r}) + N\int d^3\mathbf{r}' g(r') U_{pol}^{scr}(\mathbf{r}-\mathbf{r}') \tag{1.30}$$

The Hartree-Fock potential (when the exchange term is neglected) is given by

$$U_{HF}(\mathbf{r}) = e^2\sum_{\mathbf{k}'}\int d^3\mathbf{r}'\frac{|\psi_{k'}(\mathbf{r}')|^2}{|\mathbf{r}-\mathbf{r}'|} \tag{1.31}$$

where e is the electron charge, and the summation is extended over all the electrons except the k^{th}. The electron-molecule polarization potential (Springett *et al.*,

1968), may be represented "taking also into account the penetration effect within the molecular core" as Kivel (1959) did, by the semiempirical fomula

$$U_{pol}(\mathbf{r}) = -\frac{\alpha e^2}{2}\frac{1}{\left(|\mathbf{r}|^2 + d^2\right)^2} \tag{1.32}$$

where α is the molecular polarizability and d is a cutoff parameter (of the order of the dimensions of the molecule).

The interaction of the electron with molecules in the bulk is screened because of the presense of other neighboring molecules. Assuming a local screening and neglecting the Coulomb and exchange interaction of the excess electron with the molecules around the W-S cell (in view of the short range of the Hartree-Fock interaction) one obtains the screened potential

$$U_{pol}^{scr}(\mathbf{r} - \mathbf{r}') = -\frac{\alpha e^2}{2}\frac{f(r)}{\left(|\mathbf{r} - \mathbf{r}'|^2 + d^2\right)^2} \tag{1.33}$$

and for $f(r)$ the Lorentz local field screening function was chosen (Lorentz, 1952, Lekner, 1967)

$$f(r) = \begin{cases} 1 & \text{if } r < r_s \\ \left(1 + \frac{8}{3}\pi N\alpha\right)^{-1} & \text{if } r > r_s \end{cases} \tag{1.34}$$

The total potential with which the electron interacts can then be written as

$$\begin{aligned} U(\mathbf{r}) \;=\; & U_{HF}(\mathbf{r}) - \frac{\alpha e^2}{2}\frac{1}{(r^2 + d^2)^2} \\ & -\frac{\alpha e^2}{2}\frac{N}{(1 + \frac{8}{3}\pi N\alpha)}\int_{r>r_s} d^3\mathbf{r}'\frac{1}{\left(|\mathbf{r} - \mathbf{r}'|^2 + d^2\right)^2} \end{aligned} \tag{1.35}$$

having approximated the pair distribution function $g(r)$ by a step function, viz.,

$$g(r) = \begin{cases} 0 & \text{if } r < r_s \\ 1 & \text{if } r > r_s \end{cases} \tag{1.36}$$

If the electron scattering cross section $\sigma(\epsilon)$ is independent of the electron energy in the range where the s-wave electron scattering is dominant, then the Hartree-Fock potential could be replaced by a "hard core" potential, which is defined by a "hard core" radius a so that

$$\sigma = \pi a^2 \tag{1.37}$$

After doing the integral over space in Eqn 1.35 and substituting a "hard" sphere potential for $U_{HF}(r)$ the potential inside the cell then becomes

$$U_{eff}(r) = -\frac{\alpha e^2}{2}\frac{1}{(r^2+d^2)^2} - \frac{\alpha e^2}{2}\frac{\pi N}{(1+\frac{8}{3}\pi N\alpha)}\left\{\frac{1}{2r}\ln\left[\frac{(r_s+r)^2+d^2}{(r-r_s)^2+d^2}\right]+ \frac{1}{d}\left[\pi - \tan^{-1}\left(\frac{r_s+r}{d}\right) - \tan^{-1}\left(\frac{r-r_s}{d}\right)\right]\right\} \quad a \le r \le r_s \quad (1.38)$$

The ground state energy V_0 of the excess electron in the fluid can therefore be determined using the effective potential given by 1.38 to solve the Schrödinger equation (Eqn 1.28) for the lowest eigenvalue. From the form of $U_{eff}(r)$ it can readily be seen that there is an explicit dependence of this potential (and therefore of V_0) on the number density N of the fluid. The dependence of $U_{eff}(r)$ on the temperature however is not an explicit one but may be introduced (in this model) through changes in the "hard core" of the fluid molecule with the temperature (see Chapter 5).

The medium polarization energy P^+ due to the positive ion has long been approximated by the Born formula (Born, 1920; Christophorou and Siomos, 1984), viz.,

$$P^+ = -\frac{e^2}{2r}\left(1-\frac{1}{\epsilon}\right) \quad (1.39)$$

where e is the electronic charge, ϵ is the dielectric constant of the medium and r is the radius of the cavity in which the positive ion finds itself. In the Born's picture of course one asssumes that the positive ion and the "hole", left by the ejection of the electron, reside at the center of a sphere of radius r surrounded by the molecules of the fluid. In a more realistic approach the motion of the positive ion and the "hole" within the W-S cell should be taken into account. If then the positive charge is located at a distance r from the center, and $g(r)$ is approximated by a step function, the polarization energy of the medium because of the presence of the charge is given by

$$P^+(r) = -\frac{\alpha e^2}{2}\frac{N}{(1+\frac{8}{3}\pi N\alpha)}\int_{r>r_s} d^3\mathbf{r}'\frac{1}{\left(|\mathbf{r}-\mathbf{r}'|^2+d^2\right)^2}$$

$$= -\frac{\alpha e^2}{2}\frac{\pi N}{(1+\frac{8}{3}\pi N\alpha)}\left\{\frac{1}{2r}\ln\left[\frac{(r_s+r)^2+d^2}{(r-r_s)^2+d^2}\right]+\right.$$
$$\left.\frac{1}{d}\left[\pi-\tan^{-1}\left(\frac{r_s+r}{d}\right)-\tan^{-1}\left(\frac{r-r_s}{d}\right)\right]\right\} \quad (1.40)$$

Averaging over all accessible positions within the cell the polarization energy of the medium is written as

$$P^+ = \frac{3\alpha e^2\pi N}{2\left(1+\frac{8}{3}\pi\alpha N\right)}\frac{1}{r_o^3}\int_0^{r_o} drr^2\left\{\frac{1}{2}\ln\left[\frac{(r_s+r)^2+d^2)}{(r_s-r)^2+d^2)}\right]+\right.$$
$$\left.\frac{1}{d}\left[\pi-\tan^{-1}\left(\frac{r_s+r)}{d}\right)-\tan^{-1}\left(\frac{(r_s-r)}{d}\right)\right]\right\} \quad (1.41)$$

where r_o is such that $4\pi r_o^3/3$ is the volume accessible to the "hole" (positive charge). Integation over space of Eqn 1.41 leads to

$$P^+ = \frac{3\alpha e^2\pi N}{2\left(1+\frac{8}{3}\pi\alpha N\right)}\frac{1}{r_s}\frac{1}{x^3}\left\{\frac{1}{4}\left(x^2+1+y^2/3\right)\ln\left[\frac{(x+1)^2+y^2}{(x-1)^2+y^2}\right]-\right.$$
$$\left.\frac{x^3+1}{3y}\tan^{-1}\left(\frac{x+1}{y}\right)+\frac{x^3-1}{3y}\tan^{-1}\left(\frac{x-1}{y}\right)-\frac{x}{3}+\frac{\pi x^3}{3y}\right\} \quad (1.42)$$

where

$$x=\frac{r_o}{r_s} \qquad \text{and} \qquad y=\frac{d}{r_s} \quad (1.43)$$

When the cutoff distance d is let to go to zero and the r_o is let to go to r_s this expression for the P^+ reduces to

$$\lim_{d\to 0, r_o\to r_s} P^+ = -\frac{3\alpha e^2}{2r_s^4}\frac{1}{\left(1+\frac{8}{3}\pi\alpha N\right)} \quad (1.44)$$

By using the Clausius-Mossotti relationship between the polarizability and the dielectric constant

$$\epsilon \simeq \frac{1+\frac{8}{3}\pi\alpha N}{1-\frac{4}{3}\pi\alpha N} \quad (1.45)$$

one obtains back the Born formula (Eqn 1.39).

Similarly P^+ exhibits (as V_o does) an explicit dependence on the density of the fluid and the only temperature dependent quantity appears to be the dielectric constant (or the molecular polarizability). Since for the temperature range studied the dielectric constant (or the molecular polarizability) does not vary drastically with T the P^+ is not strongly dependent on the temperature (see Chapter 5).

1.4 Outline of the Present Work

The present work consists of experimental studies and analyses of:
(a) the effect of temperature and number density on the low energy (0 - 10 eV) electron attachment processes to three "hot"(rotationally and/or vibrationally excited) molecules

1. The normal perfluorobutane, $n-C_4F_{10}$.
2. The normal perfluorohexane, $n-C_6F_{14}$.
3. The sulfuryl fluoride, SO_2F_2.

(b) multiphoton ionization of TMPD (N,N,N',N'-tetramethyl-p-phenylenediamene) in ethane and the effect of the number density and temperature on this process.

In Chapter 2 the experimental techniques and procedures employed in the present work are discussed. In Chapter 3 the results and analyses are presented for $n-C_4F_{10}$ and $n-C_6F_{14}$. In Chapter 4 the results of the study for SO_2F_2 are presented. The objective of the electron attachment studies was to examine the effect of the internal excitation and the number densities of the attaching and the carrier gas, on the electron attachment properties of organic polyatomic perfuororcarbons.

The study of the above molecules was motivated by practical as well as by intinsic reasons. Some of these molecules have high dielectric strengths and can be used as gaseous insulators, for diffuse discharge-switches, plasma etching, gas-filled radiation detectors, etc. There is also a need to overcome the shortcomings of the present theory and be able to get a deeper insight into the electron attachment processes of energy rich polyatomic molecules.

Chapter 5 contains the results and analyses of the photoionization of TMPD embedded in ethane and studied with the multiphoton ionization conductivity (MPIC) technique. The objective of these studies was to derive information on the effect of the temperature and the density of the medium in which the molecule is embedded on the production of electron-ion pairs by multiphoton ionization

(MPI) proceses. Finally in Chapter 6 a summary of the results and conclusions are given.

Chapter 2

Experimental Techniques and Procedures

2.1 Introduction

In this chapter the experimental methods and analytical procedures for the two techniques (High Temperature Electron Swarm and Multiphoton Ionization Conductivity) employed in the present studies are presented and discussed.

A great variety of experimental techniques can be employed to study the electron attachment to molecules. In the present work a High Temperture Electron Swarm Apparatus (HTESA) was used to study the effect of the temperature and the density on the two resonance electron attachment processes, namely the nondissociative and the dissociative electron attachment.

In an electron swarm experiment the total gas pressures employed can vary from a few kPa to a few MPa, so that the short-lived ($\tau_a \leq 10^{-6}s$) negative ion states (for which the EA is positive) can be stabilized and therefore probed and studied. Variation of the temperature and density provides a means for studying the (many times delicate) dependence of the electron attachment processes on these parameters. Under conditions of high gas number densities the electrons collide many times with the atoms or molecules of the gas and the determination of the electron energy distribution function, $f(\epsilon, E/N, T)$, can only be obtained by solving the appropriate Boltzmann transport equation (Christophorou, 1984;

Huxley and Crompton, 1974)

$$\frac{\partial(nf)}{\partial t} + \frac{\partial(nf\mathbf{v})}{\partial r} + \frac{e}{m_e}\frac{\partial(nf\mathbf{E})}{\partial v} = C(f) \tag{2.1}$$

where $n = n(\mathbf{r}, t)$ is the number density of the electrons at position $\mathbf{r}$ and time t, $f = f(\mathbf{v}, \mathbf{r}, t)$ is the electron velocity distribution function; $\mathbf{E}$ is the applied uniform electric field in which the electrons move, and $C(f)$ is the collision integral.

Swarm experiments can provide accurate data on the magnitude, the mean electron energy and temperature dependence of the total electron attachment rate constant $k_a(E/N, T)$, and on the total electron attachment cross section $\sigma_a(\epsilon, T)$, which can be obtained by unfolding the $k_a(E/N, T)$ over the electron energy distribution function (Christophorou *et al.*, 1971).

The second technique used in this work was the Multiphoton Ionization Conductivity (MPIC) technique. Multiphoton ionization becomes the predominant process in any molecule or atom and at any wavelength provided that the optical light power is sufficiently high (Bunkin and Prokhorov, 1964;

Siomos and Christophorou, 1980). Two or three-photon processes are at an energy respectively two or three times that of the individual photons absorbed, and therefore ionization thresholds of molecules as high as $\approx 10\ eV$ can be reached using commercially available tunable dye lasers. Also one-photon forbidden transitions can easily be probed, and the laser pulse characteristics (*i.e.*, duration, intensity and wavelength) can be varied over wide ranges allowing considerable freedom in investigating multiphoton ionization processes (*i.e.*, ionization, excitation, recombination) of molecules in different environments, and in probing and understanding the effects that the density, the temperature and the pressure have on the aforementioned processes.

The MPIC technique is extremely useful in efforts to identify and understand the mechanisms of the ionization processes, and the dependence of the ionization threshold I_f of a molecule on the nature, the density, the state and the temperature of its environment. Knowledge of how a quantity such as the ionization threshold of the isolated molecule changes as the molecule finds itself in gradually denser

and denser gaseous environments can be obtained from MPIC experiments. The study of the interface region (transition from a gaseous to a liquid environment) using the MPIC technique can help link the wealth of information that exists for similar processes in the gas phase, with that in the liquid.

2.2 The High Temperature Swarm Technique

2.2.1 The Electron Swarm Method

The electron swarm technique used in the present study was originally devised by Hurst and Bortner in 1958, to study electron attachment processes in O_2/Ar mixtures. A detailed description of the technique can be found in earlier works (Hurst and Bortner, 1959; Christophorou, 1971; Spyrou, 1983; Hunter and Christophorou, 1984a; Spyrou and Christophorou, 1985a).

In the present electron swarm experiment, the electrons were produced in a plane at the source electrode, perpendicular to the applied electric field, **E**, by passage of a high energy α particle through the carrier (buffer) gas. The trajectories of these α particles were well collimated so that the electron swarms produced by the ionization of the carrier gas lie in a well defined plane. Each α particle which is produced by the decay of Cf^{252} had an energy of $\approx 6.1\ MeV$ and produces a swarm of $\approx 2.3 \times 10^5$ *electrons* when Ar is used as a buffer gas, and $\approx 1.7 \times 10^5$ *electrons* when N_2 is used, within a time of $\approx 5 \times 10^{-9}\ s$ (at a buffer gas pressure of 133 kPa) to $2{\times}10^{-10}\ s$ (at 3.2 MPa) (Hunter and Christophorou, 1984b).

Under the influence of an externally applied uniform electric field the electrons drift towards the anode and are collected. The total (buffer gas) number densities, N_t, used are such that the electrons quickly attain an equilibrium energy distribution, $f(\epsilon, E/N, T)$. This electron energy distribution function extends over a wide range of electron energies, ϵ, and is determined by the nature of the gas, the density reduced electric field E/N, and the temperature T. Electron energy distribution functions, $f(\epsilon, E/N, T)$ are well known only for a small number of gases (including Ar and N_2) and not for all the attaching gases used in these experiments. In order

to overcome the problem of the lack of accurate knowledge of the electron energy distribution function, for every electron attaching gas that was studied, binary mixtures of these electron attachers with Ar or N_2 were employed. The electron attacher was mixed in minute amounts with an abundant nonelectron attaching gas (buffer gas) for which the $f(\epsilon, E/N, T)$ is well known over a wide range of E/N values. By changing the E/N, the mean electron energy, $\langle\epsilon\rangle$, range was varied from thermal to $\approx 5\ eV$.

As the electron swarm drifts under the influence of the uniform electric field, a number of electrons are captured by the attaching gas forming negative ions. The continuity equation describing the motion of the electrons is given by

$$\frac{\partial n_e(x,t)}{\partial t} + w\frac{\partial n_e(x,t)}{\partial x} = -\eta w n_e(x,t) \tag{2.2}$$

where n_e is the electron number density, η is the unnormalized electron attachment coefficient in units of cm^{-1} (in the *c.g.s.* system), and w is the electron drift velocity. The solution to this equation can be written as

$$n(x,t) = n_0 e^{-(\eta/N_a)N_a w t}\delta(t - x/w) \tag{2.3}$$

where $\delta(t - x/w)$ is the delta function, n_0 is the initial number of electrons in the swarm at $x = 0$ (Fig. 2.1), and η/N_a is the normalized electron attachment coefficient in units of cm^2.

The motion of the electrons and the ions in the drift region induces a charge on the anode, and hence across a capacitor C, which is the effective capacitance to ground of the anode, and thereby establishes an increasing potential $V(t)$ across R (Fig. 2.1). The time constant of the preamplifier, ($\tau = RC \approx 10^{-3}s$) in the present experiments was large compared to the transit time of the electron swarm ($t_e = d/w \approx 10^{-6}s$). The voltage induced on the anode by the motion of the electrons is given by

$$V_e(t) = -\frac{1}{C}\int_0^t I_e(t)\,dt \tag{2.4}$$

where $I_e(t)$ is the induced current flowing in the anode circuit, and it is given by

$$I_e(t) = n_e(t)ew/d \tag{2.5}$$

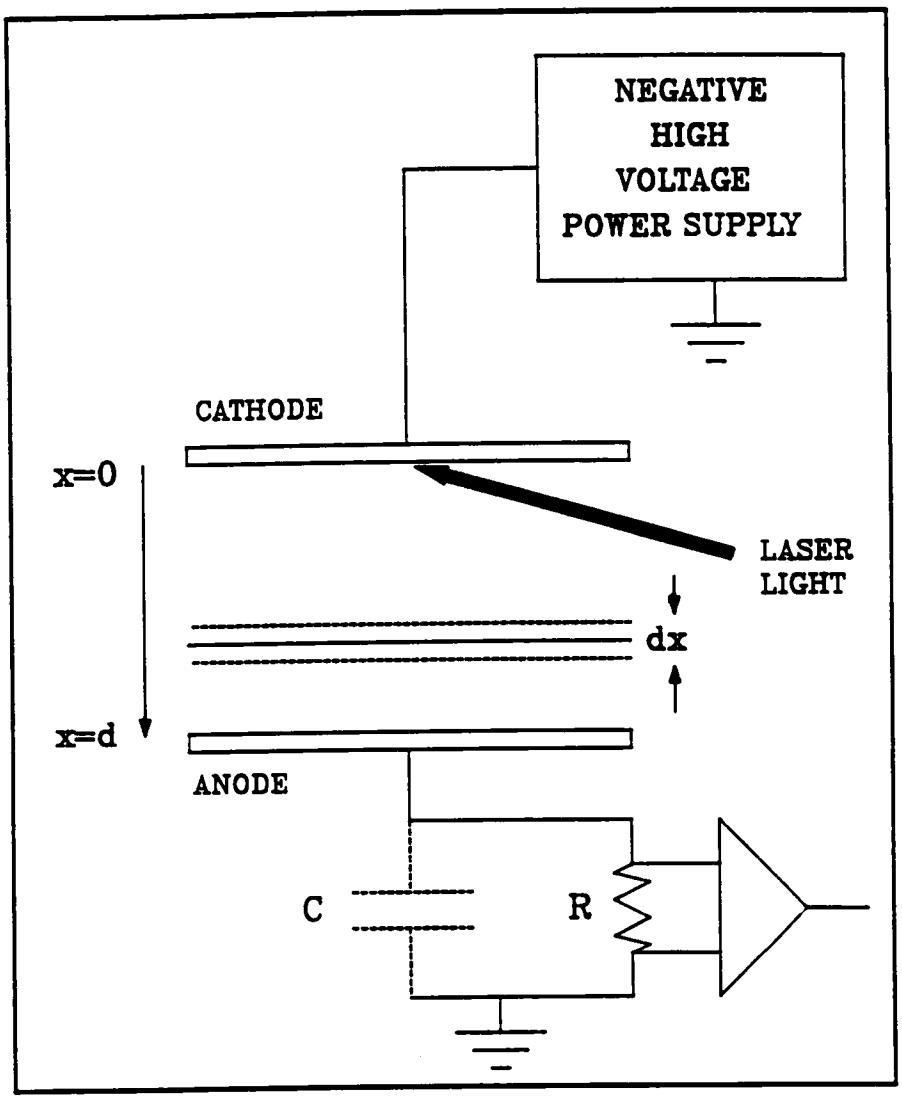

Figure 2.1: Schematic diagram showing the principles of the electron swarm technique. In the case shown the swarm of electrons is produced by the ultraviolet light of a laser beam that strikes the cathode.

where d is the drift distance, and hence

$$V_e(t) = -\frac{ew}{Cd}\int_0^t n_e(t)\,dt \tag{2.6}$$

and therefore the transient voltage on the anode is

$$V_e(t) = -\frac{n_0 e}{C(\eta/N_a)N_a d}\left(1 - \mathrm{e}^{-(\eta/N_a)N_a(d/t_e)t}\right) \qquad 0 \le t \le t_e \tag{2.7}$$

where t_e is the drift time of the electrons.

The voltage given by Eqn 2.7 is observed with a linear pulse amplifier, that has a response to a step function given by

$$V_r = \frac{t}{t_0}\mathrm{e}^{-t/t_0} \tag{2.8}$$

where t_0 is both the differentiating and the integrating time constant of the amplifier (in this work $t_0 = 15\mu s$). The output of the amplifier for times $t > t_e$ is given by

$$V(t) = \int_0^{t_0} V_r(t - t_e)\frac{dV_e(t')}{dt'}\,dt \tag{2.9}$$

hence

$$V(t) = \frac{n_0 e}{C}\int_0^{t_0} \frac{t - t'}{t_0}\mathrm{e}^{-[(\eta/N_a)N_a(d/t_e)t + (t-t')/t_0]}\,dt \qquad t \ge t_e \tag{2.10}$$

By doing the integral over time this becomes

$$V(t) = \frac{n_0 e}{C}\frac{\mathrm{e}^{-t/t_0}}{(t_e - t_0 f)}\left((\mathrm{e}^{Ut_e} - 1)t - \mathrm{e}^{Ut_e}(t_e - 1/U) - 1/U\right) \qquad t \ge t_e \tag{2.11}$$

where $f = (\eta/N_a)N_a d$ and $U = (t_e - t_0 f)/t_0 t_e$ The voltage $V(t)$ then has a maximum value at the time $t = t_m$ which can be determined from

$$\left.\frac{dV_e(t)}{dt}\right|_{t=t_m} = 0 \tag{2.12}$$

Thus

$$t_m = \frac{\left(\mathrm{e}^{Ut_0}(t_0 + t_e - 1/U) + (1/U - t_0)\right)}{(\mathrm{e}^{Ut_0} - 1)} \tag{2.13}$$

Eqn 2.13 is then substituted into Eqn 2.11 to find $V(t_m)$. Since the drift velocity of the negative ions is more than 1000 times less than that of the electrons at any

E/N it is assumed that the linear amplifier does not respond to any slowly time varying voltages that would be induced on the anode by the drift of the ions in the gap (see Fig. 2.1).

To obtain the attaching gas number density normalized electron attachment coefficient, η/N_a, from the maximum value of $V(t)$, the voltage $V(t)$ was fed into a multichannel analyzer (MCA). For a fixed E/N and temperature the most probable channel corresponding to the maximum value $V(t_m)$ was found, first for the pure carrier gas which corresponds to a voltage

$$V(t_m) = \frac{n_0 e}{C} \exp(-1) \tag{2.14}$$

and then for the binary mixture of the attaching-carrier gas. Consequently, from the ratio of these two channel numbers, the quantity f and hence the attachment coefficient η/N_a was obtained by an iterative procedure using Eqns 2.11 and 2.14. By varying the E/N, the η/N_a was measured as a function of E/N. From knowledge of the electron drift velocity as a function of E/N (see Tables 3.1 to 3.2 and 4.1 to 4.5) the product $(\eta/N_a) \cdot w$ was determined which gives the absolute electron attachment rate constant, $k_a(E/N,T)$ which is expressed in units of $cm^3 \cdot s^{-1}$ (in the $c.g.s.$ system). Knowledge of the electron energy distribution function $f(\epsilon, E/N, T)$ allows to translate $k_a(E/N,T)$ into a more meaningful quantity $k_a(\langle\epsilon\rangle, T)$ where $\langle\epsilon\rangle$ is the mean electron energy determined at each E/N from the known electron energy distribution function, $f(\epsilon, E/N, T)$ for the buffer gas. Typical examples of $f(\epsilon, E/N, T)$ for different values of E/N $(10^{-17} V cm^2)$ for Ar and N_2 (which are the carrier gases used) are shown in Figs. 2.2 and 2.3.

2.2.2 Apparatus and Experimental Procedure

The experimental apparatus is shown schematically in Fig. 2.4. The apparatus has been previously described (Spyrou, 1983) and consists of three parts: (i) the drift chamber, (ii) the gas manifold, and (iii) the carrier gas purification system.

The chamber was pumped by a turbo-molecular pump with a base pressure of a few parts in 10^{-8} $Torr$, and an outgassing rate of 10^{-4} $Torr$ per hour. The

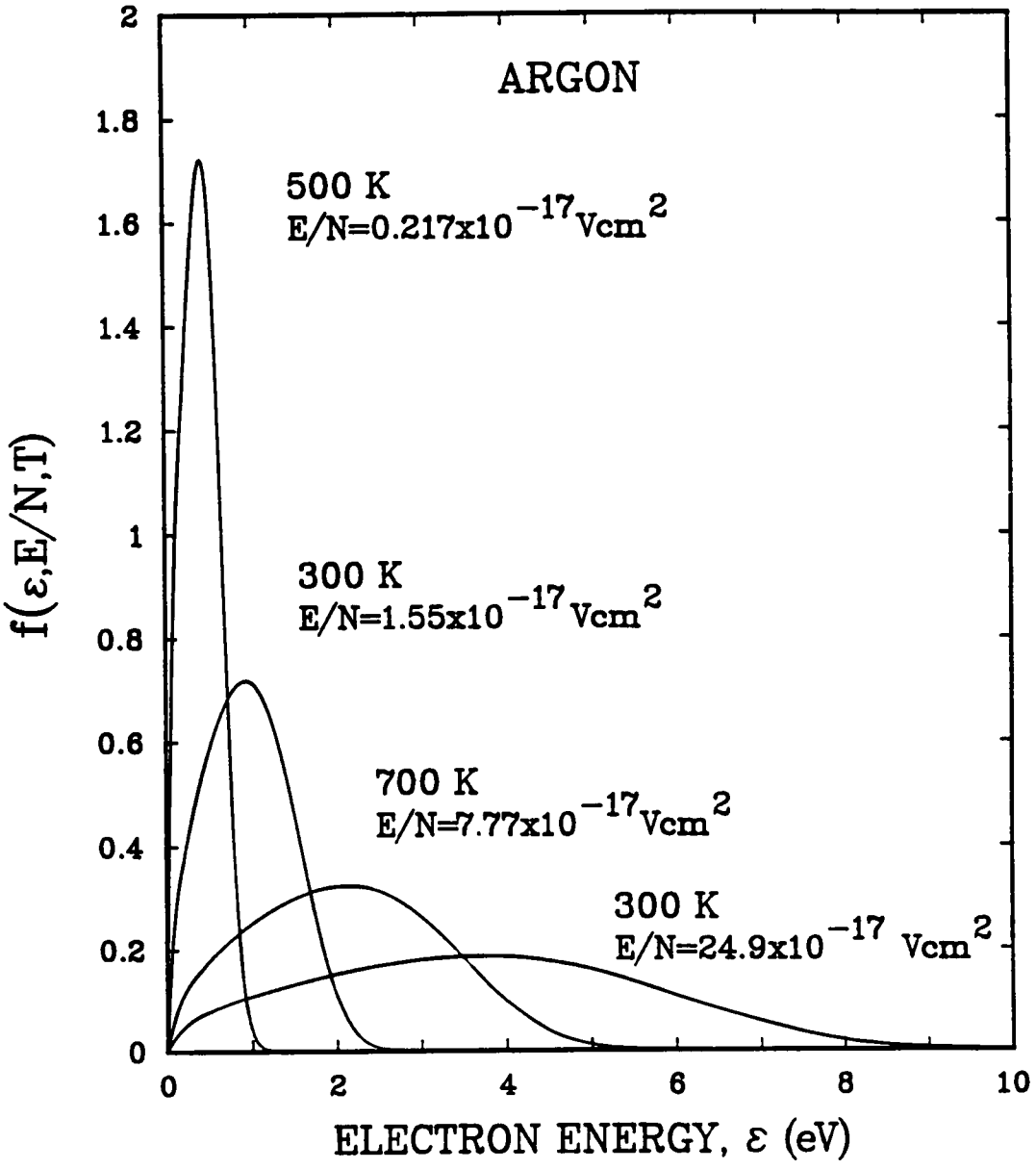

Figure 2.2: Electron energy distribution functions in Ar, for four different $E/N(10^{-17}\ Vcm^2)$ values at various temperatures, obtained using a two-term Boltzmann solution (Luft, 1975).

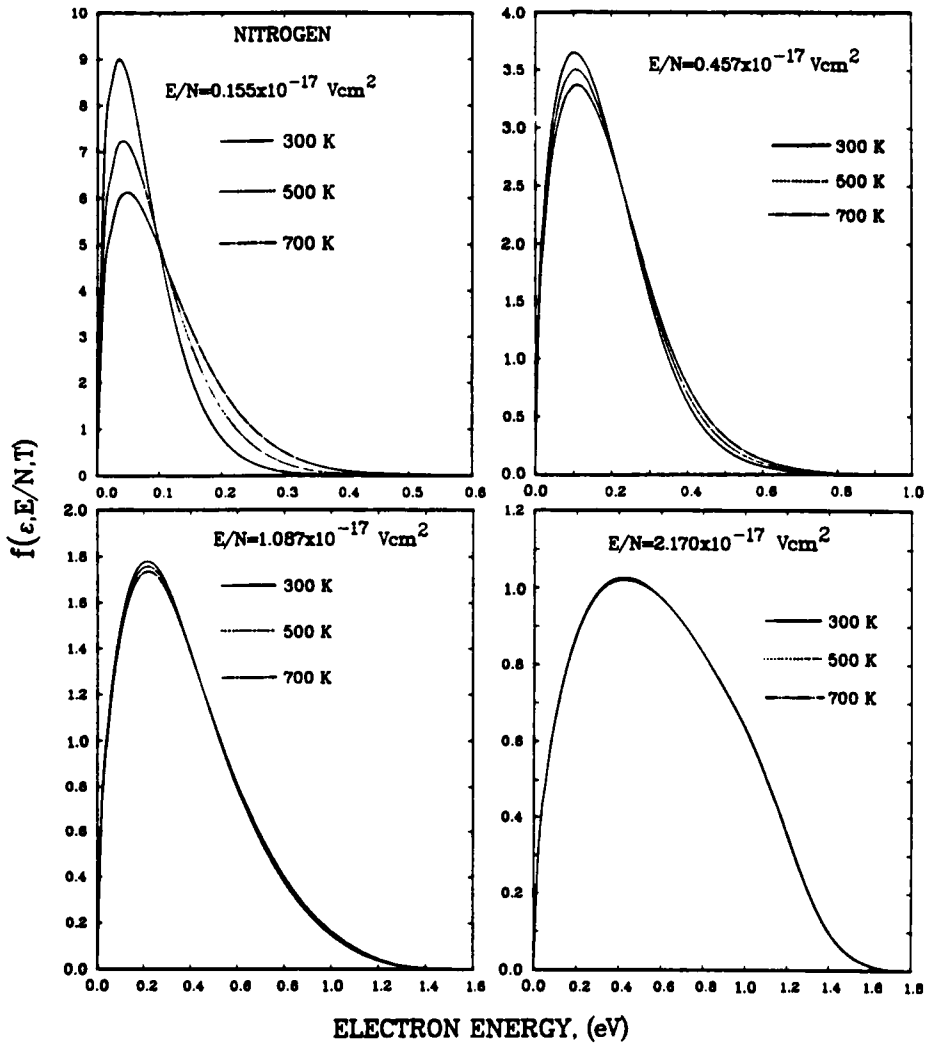

Figure 2.3: Electron energy distribution functions in N_2, for four different $E/N(10^{-17}\ Vcm^2)$ values at various temperatures, obtained using a two-term Boltzmann solution (Luft, 1975).

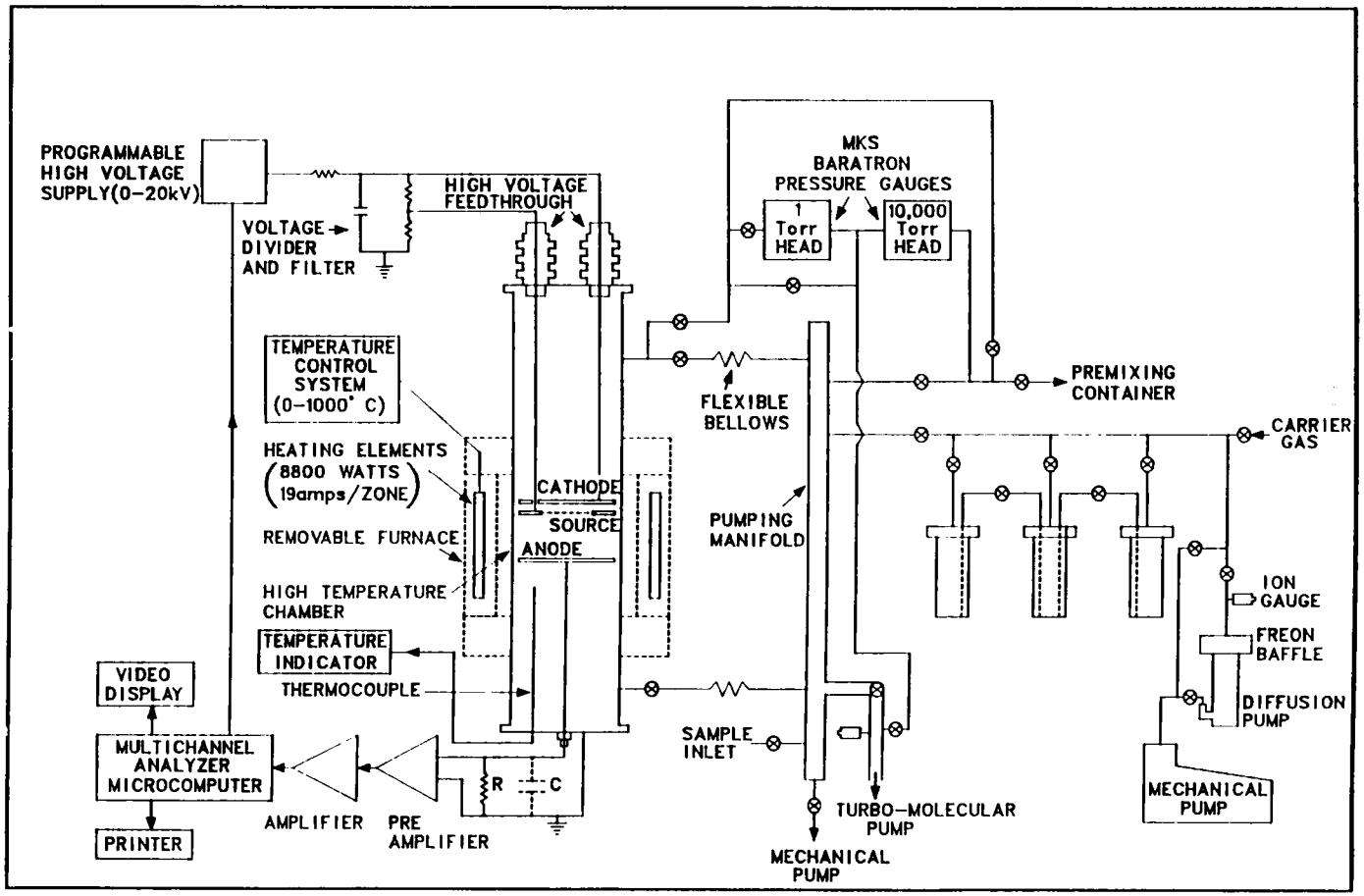

Figure 2.4: Layout of the high temperature electron swarm apparatus.

total (carrier gas) pressure, and that of the attaching gas was measured using a $10,000(\pm 0.1)$ *Torr* and a $1.00000(\pm 0.00001)$ *Torr* MKS Baratron pressure transduser. Using a Bertan (model 205A-10N) programmable power supply $(0-20kV)$ voltages were applied to the electrodes which were measured by a Keithley (model 182) digital voltmeter, using a high precision voltage divider. The induced anode voltages, produced by the motion of the electrons in the drift region, were detected and amplified by a preamplifier (Tennelec TC 161D) and a linear amplifier (Tennelec TC 222).

A specially designed furnace (series 3210, split type) and a temperature control system (series 230) built by the Applied Test System, Inc. were used to study the electron attachment over a temperature, T, range 300 to 750 K. The walls of the cylidrically shaped furnace, were made of low "K" factor vacuum cast ceramic insulation, providing minimum heat losses, as well as a rigid structure. Two heating zones (upper and lower) of 8800 *Watt* elements each, were placed inside of the insulation of the furnace. These heating zones were independently heated by the passage of a 19 *Amp/zone* current, which was provided by the temperature controllers. Two thermocouples, one being used to measure the temperature of the lower zone, and the other of the upper one, were connected to the temperature controllers. Six additional chromel-alumel type KX thermocouples were placed inside the chamber in order to measure the temperature as close to the interaction region (the space between the α particle source and the collector) as possible. These thermocouples were connected to a digital temperature indicator (OMEGA, Multipoint Selector 405A). By the use of the furnace and the accessory equipment, the desired temperature could easily be obtained within $\pm 2.2^{\circ}$ C or $\pm 0.75\%$ (whichever is greater) limited only by the limit error specified for the thermocouples used.

The experimental procedure applied in this work was as follows: The chamber was first brought to the desired temperature. At that fixed temperature the pure carrier gas was admitted into the chamber at a given pressure, and a distribution of voltage pulse heights were obtained at a given E/N, which were accumulated in

a multichannel analyzer (MCA) operating in the pulse height analysis mode. The most probable pulse height was recorded, the E/N was changed and a new series of most probable pulse heights were obtained as a function of E/N. If the dependence on the total pressure of the attachment processes was also to be studied, then the above set of measurements were performed over a range of buffer gas pressures as well. An admixture of the attaching gas (usually one part in $10^5 - 10^8$ of the total gas pressure) with the buffer gas was admitted into the chamber, and a new series of most probable pulse heights was obtained as a function of E/N and the total gas number density N_t. Thus by knowing the pulse heights with and without the attaching gas, at any given E/N, the η/N_a and the $k_a(\langle\epsilon\rangle, T)$ were obtained by using a simple numerical iterative procedure. The partial pressure of the attaching gas was very small, and thus it was safe to assume that any influence of the attaching gas on the electron energy distribution, $f(\epsilon, \langle\epsilon\rangle, T)$, was negligible. But in order to observe and remove any possible such influence, measurements of $k_a(\langle\epsilon\rangle, T)$ were performed as a function of the attaching gas number density, N_a, at fixed total gas number densities N_t. From plots of $k_a(\langle\epsilon\rangle, T)$ versus N_a/N_t the values of $k_a(\langle\epsilon\rangle, T)$ for $N_a \to 0$ were determined by extrapolation. Similar sets of measurements were performed for all the temperatures studied (see Chapters 3 and 4).

Before every measurement the carrier gases (quoted purity: 99.9995% for both carrier gases used) were subjected to liquid nitrogen temperatures (for $\sim$ 15 hours), in order to freeze any condensible impurities (*e.g.*, water vapor) which could affect the voltage pulse heights. The vapor from these gases was then extracted at temperatures just above the boiling point for each buffer gas. This procedure gave stable pulse height measurements which were reproducible to within ± 5 channels in the 2000 channels of the MCA (which is very accurate). The attaching gases used were subjected to several freeze distillation cycles prior to any measurements in order to remove air from the samples.

An analysis of the experimental errors in the determination of $k_a(\langle\epsilon\rangle, T)$ is given in Table 2.1 (Hunter and Christophorou, 1984b; Spyrou and Christophorou,

Table 2.1: Sources of error and their respective estimated uncertainties in the electron swarm experiment

Source	Error
Drift distance	$\pm 1.0\%$
Chamber Temperature	$\pm 0.5 - 2.0\%$
Total gas pressure	$\pm 0.5\%$
Electric field	$\pm 0.5\%$
Partial attaching gas pressure	$\pm 2.0\%$
Electron swarm transit time	$\pm 0.5\%$
Statistical uncertainty in determining the average electron swarm pulse height	$\pm 0.5 - 2.0\%$
Approximation in the numerical iteration procedure to obtain the electron attachment rate constant	Expected to be small when the electron transit time $\geq$ the time constant of the linear amplifier ($15\mu s$)
Non-ideal response characteristics of the linear amplifier	Same conditions as above

1985a). The total uncertainty in $k_a(\langle\epsilon\rangle, T)$ is estimated to be $\pm 6 - 8\%$. The largest contibution to the error arises from the measurement of the small partial (attaching gas) pressures.

2.2.3 Analytical Methods

The total electron attachment rate constant $k_a(E/N, T)$, measured directly in these swarm experiments, can be used to obtain the total electron attachment cross section, $\sigma_a(\epsilon, T)$ for each of the attaching gas molecules. The cross section $\sigma_a(\epsilon, T)$ is related to the $k_a(\langle\epsilon\rangle, T)$ through

$$k_a(\langle\epsilon\rangle, T) = (2/m)^{1/2} \int_0^\infty \epsilon^{1/2} \sigma_a(\epsilon, T) f(\epsilon, \langle\epsilon\rangle, T)\, d\epsilon \tag{2.15}$$

where ϵ is the electron energy, m is the electron mass, and $f(\epsilon, \langle\epsilon\rangle, T)$ is the electron energy distribution at each value of the mean electron energy, $\langle\epsilon\rangle$. For these experiments, the $f(\epsilon, \langle\epsilon\rangle, T)$ used were assumed to be those of the pure buffer gas, since only small number densities, N_a, of the attaching gas were used. Also plots of $k_a(\langle\epsilon\rangle, T)$ versus N_a/N_t were made (see Chapters 3 and 4) and the values of $k_a(\langle\epsilon\rangle, T)$ obtained when $N_a \rightarrow 0$ were used in all the analyses, removing in this way any influence that the attaching gas molecules might have on the electron energy distribution function.

The distribution functions for N_2 and Ar were calculated from the numerical solution of the Boltzmann transport equation (see Eqn 2.1) using a code developed by Luft (1975). At each temperature, the $\sigma_a(\epsilon, T)$ were determined using the electron swarm unfolding technique (Christophorou *et al.*, 1971). To perform the unfolding procedure, the monoenergetic electron attachment rate constant $k_m(\epsilon, T)$ is first defined as

$$k_m(\epsilon, T) = \sigma_a(\epsilon, T)(2/m)^{1/2} \epsilon^{1/2} \tag{2.16}$$

Thus the observed electron attachment rate constant at the mean electron energy $\langle\epsilon\rangle_i$ and the temperature T is expressed as

$$k_a(\langle\epsilon\rangle_i, T) = \int_0^\infty k_m(\epsilon, T) f(\epsilon, \langle\epsilon\rangle_i, T)\, d\epsilon \tag{2.17}$$

Starting a numerical iterative procedure, $k_m(\epsilon,T)$ is first approximated by the $k_a(\langle\epsilon\rangle,T)$, by imposing the condition $k_m(\epsilon,T)=0$ above the maximum energy accessible by $f(\epsilon,\langle\epsilon\rangle,T)$ at the highest E/N value. These values of $k_m(\epsilon,T)$ are then substituted into Eqn 2.17 and a new series of values for $k_a(\epsilon,\langle\epsilon\rangle_i,T)$ are calculated for every mean electron energy, $\langle\epsilon\rangle_i$, used. By defining weighting factors $W(\langle\epsilon\rangle_i)$ as the ratio of the observed electron attachment rate constant $k_{obs}(\langle\epsilon\rangle_i,T)$ to the calculated $k_{cal}(\langle\epsilon\rangle_i,T)$, a new estimate for the monoenergetic electron attachment rate constant $k_m(\epsilon,T)$ can be obtained through

$$(k_m)_{new}(\epsilon,T)=(k_m)_{old}(\epsilon,T)\cdot\frac{\sum_i W(\langle\epsilon\rangle_i,T)^n f(\epsilon,\langle\epsilon\rangle,T)}{\sum_i f(\epsilon,\langle\epsilon\rangle,T)} \tag{2.18}$$

where n is an accelerator factor >1 which can be used to speed up the convergence rate. The new value $(k_m)_{new}(\epsilon,T)$ is then substituted back into Eqn 2.17 and the whole procedure is repeated several times until the residuals are minimized, *e.g.*,

$$\sum_i [k_{obs}(\langle\epsilon\rangle_i,T)-k_{cal}(\langle\epsilon\rangle_i,T)]^2 \longrightarrow minimum \tag{2.19}$$

The weighting factors then approach the value one and the monoenergetic electron attachment rate constants $k_m(\epsilon,T)$ do not change appreciably with any successive iterations and thus the the electron attachment cross sections can be obtained through

$$\sigma_a(\epsilon,T)=(2\epsilon/m)^{-1/2}k_m(\epsilon,T) \tag{2.20}$$

2.3 The Multiphoton Ionization Conductivity Method

2.3.1 Multiphoton Ionization Conductivity Technique

The technique used in the multiphoton ionization conductivity (MPIC) studies, is similar to the one described earlier (*e.g.*, Siomos and Christophorou, 1980; Faidas and Christophorou, 1987, 1988a, 1988b; Faidas and Siomos, 1987). These previous studies, however, were dealing exclusively with molecules in liquid environments, whereas in this work the molecules are studied in gradually denser and denser

gaseous and finally liquid environments. In this section only a brief description of the basic principles for the MPIC technique will be given.

The MPIC technique is based on the careful monitoring of the laser induced photocurrent, I_s (due to the creation of charged species by the interaction of the laser beam with the molecule), as a function of the laser intensity I_ℓ, and the determination of the order (*i.e.*, the number of photons absorbed during the process) and the nature of the multiphoton processes (Faidas and Christophorou, 1988a). Knowledge of the dependence of I_s on I_ℓ yields immediately the order of the multiphoton ionization process (see subsection 2.3.3). In order to determine this dependence, the light of a tunable dye laser is allowed to enter the ionization cell (see next subsection) and is focused between two parallel electrode plates. The charged species which are created by the interaction of the laser beam with the molecule either directly (positive ions, electrons) or indirectly through electron attachment (negative ions) move towards the electrodes under the influence of an externally applied uniform electric field. The induced voltages on the electrodes produced by the motion of the electric charges were detected and amplified using first a preamplifier and then an amplifier and finally were fed into a boxcar integrator (see next subsection). This voltage which was measured across a 10^{11} Ω resistor, represented the ionization signal, I_s. The laser intensity I_ℓ was measured by monitoring the beam behind the cell (see next subsection).

In an $n-$photon nonresonant ionization process, the ionization signal, I_s is related to the laser intensity, I_ℓ through (see Chapter 1)

$$I_s(\lambda) = C I_\ell^n \tag{2.21}$$

where λ is the wavelength of the photon. By taking the logarithm of both sides this becomes

$$\log(I_s(\lambda)) = \log(C) + n \log(I_\ell) \tag{2.22}$$

Thus the relationship between $\lg(I_S(\lambda))$ and $\lg(I_\ell)$ is described by a straight line whose slope is given by

$$S = \frac{d \log(I_s(\lambda))}{d \log(I_\ell)} = n \tag{2.23}$$

so that S (and therefore the order n of the multiphoton process) can be determined from plots of $\log(I_s)$ versus $\log(I_\ell)$.

In the wavelength regions, however, where the multiphoton ionization process is an admixture of $n-$ and $m-$photon processes, $I_s(\lambda)$ may be represented as (Faidas and Christophorou, 1988b)

$$I_s(\lambda) = A(\lambda)I_\ell^n + B(\lambda)I_\ell^m \tag{2.24}$$

where $A(\lambda)$ and $B(\lambda)$ express the relative strengths of each process as a function of the wavelength, λ. The slope S in this case is given by

$$S = \frac{d\log(I_s(\lambda))}{d\log(I_\ell)} = \frac{1}{A(\lambda)I_\ell^n + B(\lambda)I_\ell^m} \cdot \left(A(\lambda)\frac{dI_\ell^n}{d\log(I_\ell)} + B(\lambda)\frac{dI_\ell^m}{d\log(I_\ell)} \right) \tag{2.25}$$

or

$$\begin{aligned} S &= \frac{nA(\lambda)I_\ell^n + mB(\lambda)I_\ell^m}{A(\lambda)I_\ell^n + B(\lambda)I_\ell^m} \\ &= n + \frac{(m-n)B(\lambda)I_\ell^{m-n}}{A(\lambda) + B(\lambda)I_\ell^{m-n}} \end{aligned} \tag{2.26}$$

2.3.2 Apparatus and Experimental Procedure

The experimental apparatus is shown in Fig. 2.5. The ionization cell had a cubic-geometry and it was made out of stainless steel. Two ports with sapphire windows (able to withstand a pressure of 150 atm at $T = 423\ K$) were opposite to each other allowing the laser beam to enter and exit the cell. The drift space of the charged particles (ions and electrons) extended between two stainless steel electrode plates, each having a 3.0 cm diameter and being 0.5 cm apart. The applied voltages were varied between 200 - 4000 V depending on the total pressure and temperature so that space charge was avoided.

Two different types of frequency tunable dye lasers were used as light sources, which covered the entire wavelength region (from 380 nm to 510 nm) that was studied. A Nitrogen-pumped dye laser (Molectron UV100/DL 300) and an excimer XeCl-pumped dye laser (Lambda Physik EMG101MSC/FL2002) were used. The

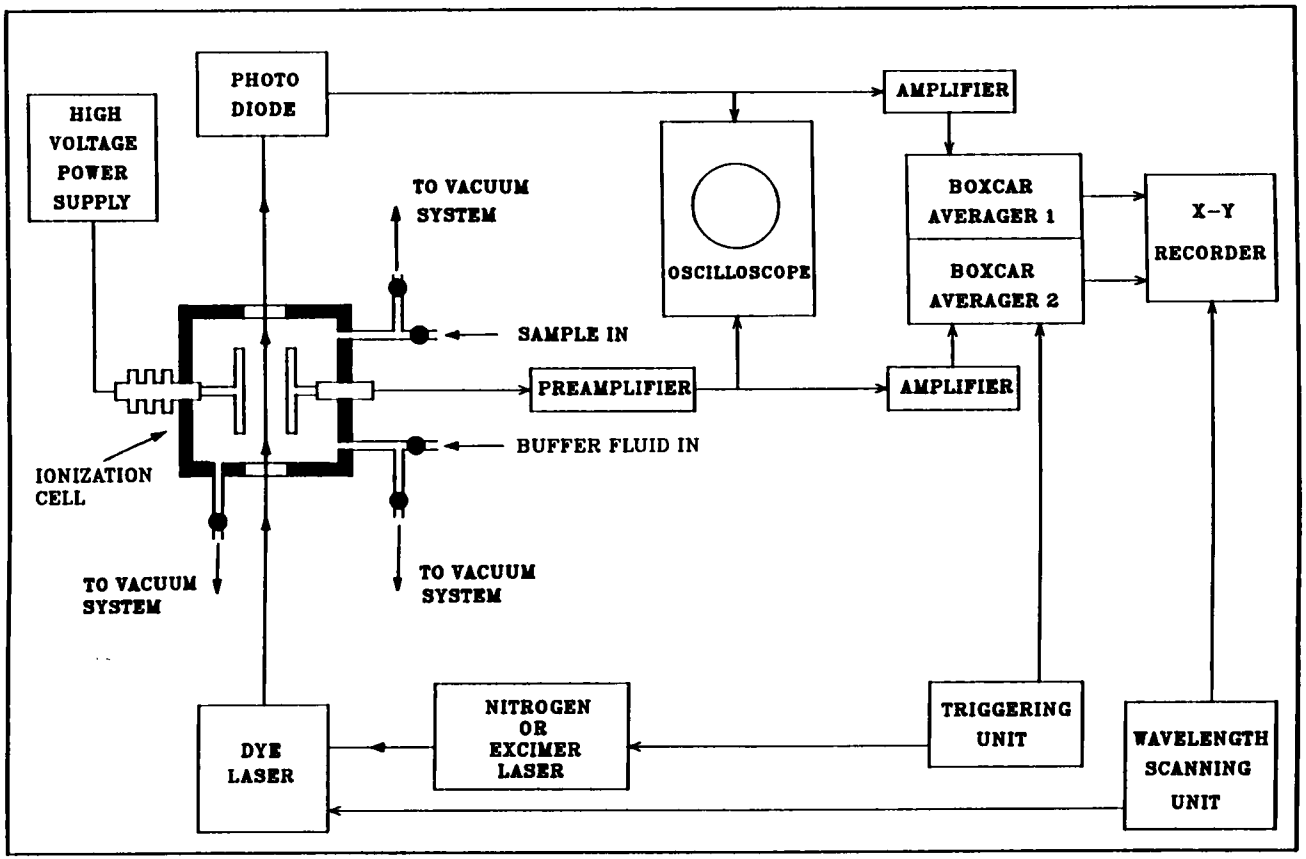

Figure 2.5: Schematic diagram of the multiphoton ionization conductivity apparatus

spectral bandwidth of the laser light produced by all the dye lasers was of the order of $\sim 0.02\ nm$ and the wavelength accuracy better than $0.1\ mm$. The pulse duration of the Nitrogen-pumped dye laser was $\sim 5\ ns$ (FWHM) and the energy per pulse ranged from 50 to 200 μJ depending on the laser dye used. The excimer XeCl-pumped dye laser had a pulse duration of $\sim 10\ ns$ and the energy per pulse ranged from 50 to 600 μJ. In order to cover the entire wavelength region, a number of different laser dyes and dye-mixtures had to be used. Table 2.2 contains a list of laser dyes that were used in this work, accompanied by their respective wavelength ranges. The light produced by the laser entered the ionization cell between the parallel electrode plates, either unfocused or focused by a lens with a focal length of $1\ m$, depending on the strength of the observed ionization signal, I_s. The electrodes were connected to a high impedance ($10^{11}\ \Omega$) charge sensitive preamplifier. The laser intensity was monitored behind the cell (see Fig. 2.5) with a photodiode of known spectral response (Molectron J3-022DW). Both the photodiode signal, I_ℓ, and the preamplifier signal, I_s, were further amplified and sampled by boxcar averagers (EG & G 162 and Princeton Applied Research 160) before they were digitized and fed into the computer for further analysis.

The cell was pumped using a diffusion pump with a base pressure of $\approx 1.0^{-7}$ *Torr*. The pressure of the sample molecules (which could be ionized by the dye laser) in the cell was measured using a 100.000 ($\pm$0.001) *Torr* MKS Baratron pressure transducer, and the pressure of the buffer medium was measured with a Stathan absolute pressure transducer (model PA822-2M). The voltage was applied to the electrodes using a Fluke (model 410B) power supply. A heating jacket was employed to heat the cell (to the desired temperature) and was controlled by a Barber-Colman (model 410) temperature controller. Two thermocouples were placed into the cell in order to measure the temperature as close to the interaction region as possible. One of these two thermocouples was connected to a digital temperature indicator, and the other's signal was fed into the temperature controller.

Briefly the experimental procedure was as follows: The cell was first heated to

Table 2.2: Dyes and Dye-mixtures

		Wavelength Range (nm)	
		Pumping Laser	
Dye-name	Supplier*	Nitrogen	Excimer
QUI	L	372-412	368-402
QUI/DPS(3/4)		381-415	
DPS	E	396-416	
DPS/Bis-MSB (2/3)		396-430	
Bis-MSB	E	411-430	
Bis-MSB/Coumarin 440 (2/1)		415-440	
Coumarin 440	E	420-457	
Coumarin 460	E	440-478	
Coumarin 481	E	460-517	
Coumarin 102	L		460-510
Coumarin 500	E	473-547	

*L=Lambda Physik; E=Exciton

the selected temperature after it was baked for more than 48 hours at about 450 K, so that the outgassing rate would be low. At the fixed temperature the sample molecules (which could be ionized by the dye laser) were admitted into the cell, at a pressure of ≈ 1 $Torr$. Then the laser light was allowed to enter the cell, and a series of "power measurements" was taken, (that is the ionization signal I_s was observed as a function of the laser intensity I_ℓ at a particular wavelength). Then the wavelength was varied and a new series of power measurements was taken. In order to study the dependence of I_f on the density of the medium, buffer fluid was admitted into the cell and a new series of power measurements were obtained for different values of the total gas number density, which was varied from that of a dilute gas to that of a dense gas to that of supercritical gas and finally to that of a liquid.

Before every measurement was made, care was taken to purify the sample and the buffer medium. The sample was purified by fractional distillations and the carrier fluid was deoxygenated with several successive freeze-pump-thaw cycles (see Chapter 5).

2.3.3 Data Analysis

In order to determine the ionization threshold, I_f, of a molecule in a medium from measurements of the laser induced photocurrent, I_s versus the laser intensity I_ℓ, the wavelength range over which the laser wavelength λ was varied, was divided into three regions: (i) The region where the species can be ionized directly by absorption of n photons (ii) The region where n-photon excitation just above the ionization continuum occurs, leading to (a) direct n-photon ionization with relatively low efficiency (decreasing with increasing laser wavelength) or (b) relaxation to a lower lying (longer-lived) excited state and subsequent ionization with the absorption of an extra photon (iii) The region where $(n+1)-$photon ionization occurs, involving $n-$photon excitation below the ionization continuum, relaxation to a lower lying (longer lived) excited state and subsequent ionization from that state by absorption of another photon.

In the laser wavelength regions (i) and (iii) the ionization signal I_s is related to the laser intensity I_ℓ through Eqn 2.21 and plots of $\log I_s$ versus $\log I_\ell$ are straight lines whose slope, S, can be determined and therefore the order n or $n+1$ of the multiphoton ionization process (see Eqn 2.22). When, however, λ lies in the laser wavelength region (ii) the photoionization signal, I_s, is related to the laser intensity, I_ℓ, through Eqn 2.24 (with $m = n+1$). In this region, the slope S depends on the relative contribution of the two different order processes, namely n and $(n+1)-$photon ionization, and can be obtained by employing Eqn 2.26 and takes values between n and $n+1$.

The relation 2.21 which holds in regions (i) and (iii) over wide ranges of the laser intensity can still be employed in the laser wavelength region (ii) as long as I_ℓ is varied over narrow intensity ranges (see Chapter 5) and the dependence of I_s on I_ℓ can be represented as

$$I_s(\lambda) = K I_\ell^\alpha \tag{2.27}$$

where α is the "apparent" order of the multiphoton ionization process and is a real number between n and $n+1$ expressing the coexistence of n and $(n+1)-$photon ionization processes. The above relationship enables the determination of the slope in the region (ii) as a function of the laser wavelength without the prior knowledge of the relative strengths $A(\lambda)$ and $B(\lambda)$ of the n and $(n+1)-$photon ionization processes (see Eqn 2.26). From plots of S versus λ [in regions (i), (ii), and (iii)] the $n-$photon ionization onset can then be determined by identifying it with the longest laser wavelength for which a still measurable n-photon ionization component ($\approx 10\%$ of the total ionization signal) is present in the observed photoionization signal. This laser wavelength λ in the present study corresponded to a slope $S \approx 2.9$ and could be determined with an accuracy of $\approx 5\ nm$ ($\approx 0.05\ eV$ for the ionization onset).

Chapter 3

Variation with Temperature of the Electron Attachment to $n-C_4F_{10}$ and $n-C_6F_{14}$

3.1 Introduction

In this chapter the results of a high pressure electron swarm study on the variation of electron attachment to $n-C_4F_{10}$ and $n-C_6F_{14}$ with temperature are presented and discussed. Prior to doing this, however, a brief survey of the nondissociative and dissociative electron attachment processes to "hot" molecules is given.

The study of electron attachment to hot (vibrationally/rotationally excited) molecules is of practical as well as of basic significance (Christophorou and Hunter, 1984a). Vibrational and (to a lesser extent) rotational excitation affects the magnitude and the energy dependence of the cross section for electron attachment (see, for example, O'Malley, 1967; Massey, 1976; Bardsley and Waderha, 1979; Smirnov, 1982; Christophorou *et al.*, 1984; Spyrou and Christophorou 1985a,b,c; Christophorou *et al.*, 1987). As a rule (Christophorou *et al.*, 1984) for molecules AX for which only dissociative electron attachment processes occur, the effect of T on the cross section $\sigma_{da} = \sigma_c' p'$ for the process

$$e + AX \underset{\tau_a'^{-1}}{\overset{\sigma_c'}{\rightleftharpoons}} AX^{-*} \xrightarrow{p'} A + X^- \tag{3.1}$$

is an increase in σ_{da}; in the reaction (3.1) σ_c', $\tau_a'^{-1}$, and p' are respectively, the

capture cross section to produce AX^{-*}, the rate of autodetachment of AX^{-*}, and the probability of AX^{-*} to decay into $A + X^-$. The increase in σ_{da} results mainly from an increase in p' with T which itself results from a decrease with increasing T of the separation time of A and X^-.

For molecules AX with purely nondissociative electron attachment, the effect of T is a decrease in $\sigma_{nd} = \sigma_c p$ with increasing T for the process

$$e + AX \underset{\tau_a^{-1}}{\overset{\sigma_c}{\rightleftharpoons}} AX^{-*} \xrightarrow{p} AX^- + \text{energy} \tag{3.2}$$

which results from a decrease in p and/or σ_c as T increases.

In those cases where dissociative and nondissociative electron attachment processes take place concurrently over a given energy range ϵ, the mode of attachment (dissociative or nondissociative) itself varies with both ϵ and T (Spyrou and Christophorou, 1985b; Datskos and Christophorou, 1987; Christophorou *et al.*, 1987).

The normal perfluorocarbon alkanes with three or more carbon atoms have been found earlier (Harland and Thynne, 1973; Spyrou *et al.*, 1983; Hunter and Christophorou, 1984b; Spyrou and Christophorou, 1985a, 1985b) to attach electrons both dissociatively and nondissociatively, with both processes extending over a wide range of electron energies, and with the latter process decreasing as T increases. Electron beam studies (Harland and Thynne, 1973; Spyrou *et al.*, 1983) have shown that the parent anions $n\text{-}C_4F_{10}^{-*}$ and $n\text{-}C_6F_{14}^{-*}$ are formed at low energies (with an onset at $\simeq 0.0\ eV$ and a peak at $\simeq 0.6\ eV$ for the former and at $\simeq 0.55\ eV$ for the latter) and are long lived [the "apparent" mean autodetachment lifetime at the peak of the resonance was found by Spyrou *et al.*, (1983) to be $\simeq 21 \mu s$ for $n\text{-}C_4F_{10}$ and $\simeq 53.2\ \mu s$ for $n\text{-}C_4F_{14}$]. Fragment ions ($C_4F_9^-$, $C_3F_7^-$, $C_2F_5^-$, CF_3^-, and F^- for $n\text{-}C_4F_{10}$ and $C_6F_{12}^-$, $C_5F_{11}^-$, $C_5F_{10}^-$, $C_5F_9^-$, $C_4F_9^-$, $C_4F_7^-$, $C_3F_7^-$ and F^- for $n\text{-}C_6F_{14}$) were also detected. On the other hand, electron swarm studies (Hunter and Christophorou, 1984b) have shown that both dissociative and nondissociative electron attachment processes are present and that the latter — while predominant at low electron energies ($<1\ eV$) — extends to mean electron

energies, $\langle\epsilon\rangle$ >5.0 eV. The parent anion contribution was found to be much larger than indicated by electron beam studies. This is understood because in the swarm study transient anions with lifetimes in the range 10^{-6} to $10^{-11}s$, are stabilized and detected, while in the time-of-flight mass spectrometric study transient anions with lifetimes shorter than $10^{-6}s$ go undetected.

Based on the above studies, $n-C_4F_{10}$, and $n-C_6F_{14}$ have a bound low lying negative ion state whose potential energy curve has a minimum below that of the neutral, a vertical attachment energy of $\simeq$ 0.6 eV and $\simeq$ 0.55 eV respectively, and rise rather steeply in the Franck-Condon region. In addition, both possess one or more repulsive negative ion states at higher energies which can lead to the formation of fragment anions. Both dissociative and nondissociative electron attachment processes for both molecules occur over a common and wide mean electron energy range 0.0 to 5.0 eV.

The present study demonstrates that the mode — dissociative or nondissociative — of electron attachment to these molecules is a function of T and ϵ. It also shows — by comparing the results of these studies with those of earlier work on C_2F_6 and C_3F_8 — that this dependence is a strong function of the molecular size of these perfluoroalkanes.

3.2 Experimental Procedure

The experimental procedure and apparatus employed in the present study have been described earlier (see Chapter 2). The experiments were performed using ultrahigh purity (99.999%) Ar as a buffer gas obtained from Matheson Gas Products. Before use, the Ar gas was cooled to liquid nitrogen temperatures in order to freeze out any condensible impurities. The vapor from this cold gas was extracted at temperatures just above the Ar boiling point. The $n-C_4F_{10}$ sample was obtained from PCR/SCM Specialty Chemicals with a stated purity of 99%. The $n-C_6F_{14}$ was obtained from Pierce Chemicals with a quoted purity of 99%. The attaching gases was subjected to several vacuum distillation cycles prior to

any measurements to remove air from the sample. The total number density was in the range 2.25 to 12.88×10^{19} $molecules/cm^3$, and the attaching gas number density N_a was varied from 4.25 to 13.52×10^{13} $molecules/cm^3$ for $n-C_4F_{10}$ and from 0.05 to 1.62×10^{14} $molecules/cm^3$ for $n-C_6F_{14}$. At each temperature, T, measurements were made over a wide range of E/N (density-reduced electric field) corresponding to a mean electron energy $\langle\epsilon\rangle$, in the range 0.41 to 4.81 eV. The measured electron attachment rate constants $k_a(\langle\epsilon\rangle, T)$ and the buffer gas electron energy distribution functions $f(\epsilon, \langle\epsilon\rangle, T)$ were employed to calculate the total electron attachment cross sections $\sigma_a(\epsilon, T)$ (see Chapter 2). The $f(\epsilon, \langle\epsilon\rangle, T)$ and the electron drift velocities $w(E/N)$ for Ar at T above room temperature were assumed to be the same as those at room temperature since for the E/N employed the preponderance of the electrons have energies far in excess of thermal (see also Fig 2.2 in Chapter 2).

The possible sources of error in the measurement of $k_a(\langle\epsilon\rangle, T)$ have been discussed in Chapter 2. The total uncertainty in the measurement of $k_a(\langle\epsilon\rangle, T)$ at 300 K was estimated to be $\pm5\%$ to $\pm7\%$ (see chapter 2). At higher temperatures this is somewhat larger ($\simeq \pm6\%$ to $\pm8\%$).

3.3 Results

3.3.1 Electron Attachment Rate Constants $k_a(\langle\epsilon\rangle, T)$ as a Function of $\langle\epsilon\rangle$ and T

The total electron attachment rate constant $k_a(\langle\epsilon\rangle, T)$ for $n-C_4F_{10}$ and $n-C_6F_{14}$ have been measured at 300, 350, 400, 450, 500, 550, 600, 675, and 750 K. Although the number density N_a of the attaching gases is $\approx 10^6$ times smaller than that of the total gas number density, N_t, it was felt that even this small quantity of $n-C_4F_{10}$ or $n-C_6F_{14}$ in Ar could change the electron energy distribution function $f(\epsilon, \langle\epsilon\rangle, T)$ for the mixture, compared to that for the pure buffer gas. For this reason, at each value of T and $\langle\epsilon\rangle$, the $k_a(\langle\epsilon\rangle, T)$ was measured at a fixed total gas number density N_t as a function of N_a. From a plot of $k_a(\langle\epsilon\rangle, T)$ versus N_a/N_t the

values $k_a(\langle\epsilon\rangle, T)$ for $N_a \rightarrow 0$ were determined by extrapolation. These are considered to be the electron attachment rate constants, that would be measured had $f(\epsilon, \langle\epsilon\rangle, T)$ been characteristic of pure Ar and are the values used in subsequent discussions and analyses.

A typical set of $k_a(\langle\epsilon\rangle, T)$ vs N_a/N_t plots is shown in Fig. 3.1 for $T = 350$ K, $N_t = 9.66 \times 10^{19}$ $molecules/cm^3$, and $\langle\epsilon\rangle$ in the range 0.876 to 1.67 eV for the case of $n-C_4F_{10}$. In Fig. 3.2 a similar plot for $n-C_6F_{14}$ is shown. As a previous room temperature study has shown (Hunter and Christophorou, 1984b), the $k_a(\langle\epsilon\rangle, T)$ increases with increasing N_t for $n-C_4F_{10}$, but it is independent of N_t for $n-C_6F_{14}$, for all the temperatures studied. In the present study it was found that for $n-C_4F_{10}$ the $k_a(\langle\epsilon\rangle, T)$ increases with increasing N_t over the entire mean electron energy range studied for $T \leq 450$ K. At 500 K the $k_a(\langle\epsilon\rangle, T)$ was found to increase with N_t only for mean electron energies $\langle\epsilon\rangle \leq 1.5$ eV and to be independent of N_t at higher values of $\langle\epsilon\rangle$. These findings reflect the fact that as T increases the measured $k_a(\langle\epsilon\rangle, T)$ is increasingly dominated by the contribution of the dissociative electron attachment processes which are independent of N_t. However, in the T region where there is a large contribution from the nondissociative electron attachment process, the effect of N_t on $k_a(\langle\epsilon\rangle, T)$ is large; it is larger the higher the $\langle\epsilon\rangle$ and T because the lifetimes of the transient anions decrease with both $\langle\epsilon\rangle$ and T (Christophorou *et al.*, 1984; Spyrou and Christophorou, 1985b; Datskos and Christophorou, 1987). This is clearly seen from the data in Fig. 3.3. At low $\langle\epsilon\rangle$, the $k_a(\langle\epsilon\rangle, T)$ is almost independent of N_t, because the lower the $\langle\epsilon\rangle$ the longer lived the parent ions are; at 0.6 eV the parent negative ions, $n-C_4F_{10}^{-*}$, were found by Spyrou *et al.*, (1983) in a low pressure beam experiment to have an apparent mean autodetachment lifetime of $\simeq 21$ μs.

Thus, the absence of a density dependence of $k_a(\langle\epsilon\rangle, T)$ as in the case of $n-C_6F_{14}$ [which does not exhibit a dependence on the total number density (see Fig. 3.2 and 3.4)] is not suggestive of an absence of parent anions but rather that the anions produced are longer lived so that, for the N_t employed they are completely stabilized.

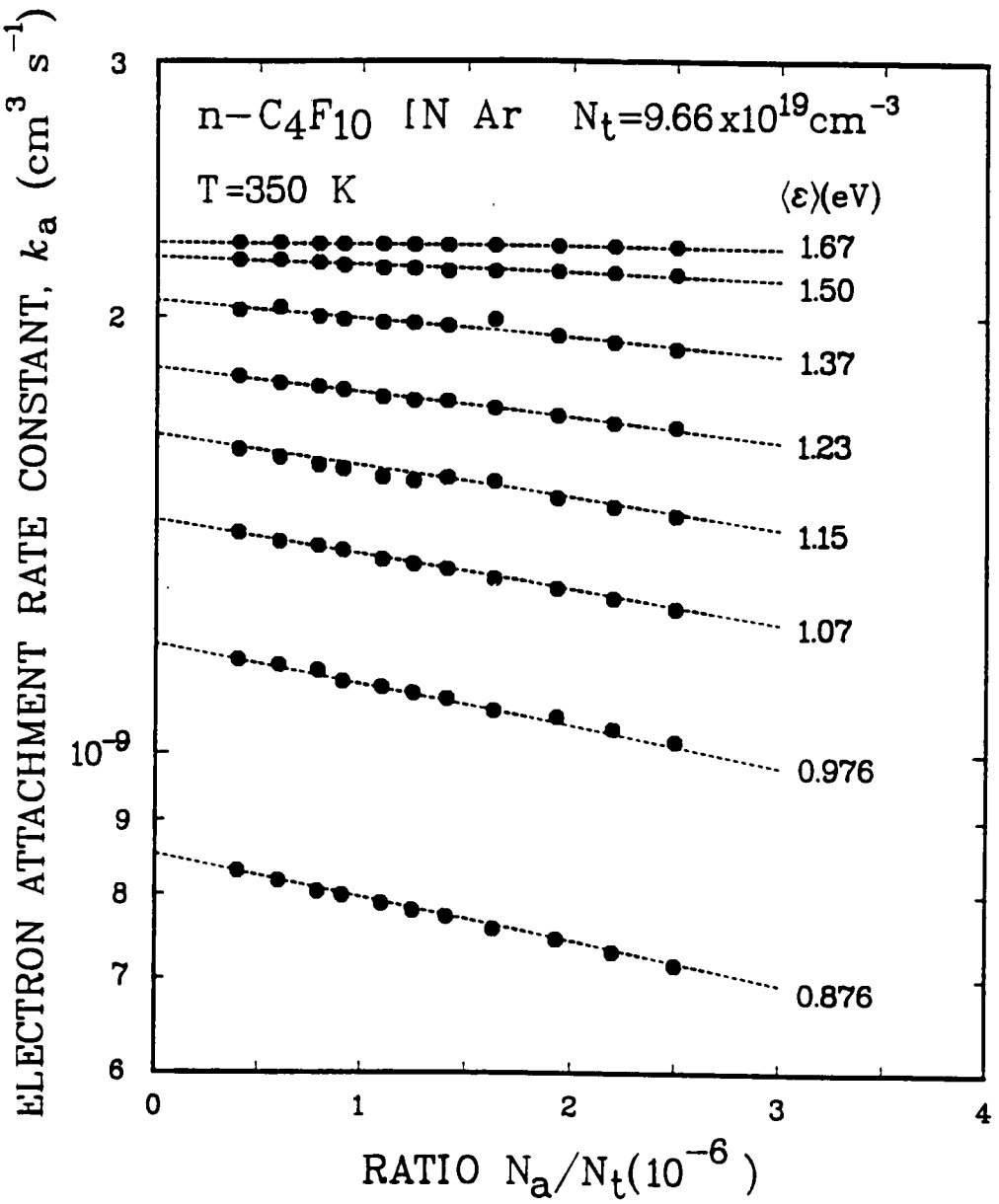

Figure 3.1: Total electron attachment rate constant $k_a(\langle\epsilon\rangle, T)$ for n-C_4F_{10} in Ar as a function of the ratio of the attaching gas number density N_a to the total gas number density N_t for several values of the mean electron energy $\langle\epsilon\rangle$ ($T = 350\ K$ and $N_t = 9.66 \times 10^{19}\ cm^{-3}$).

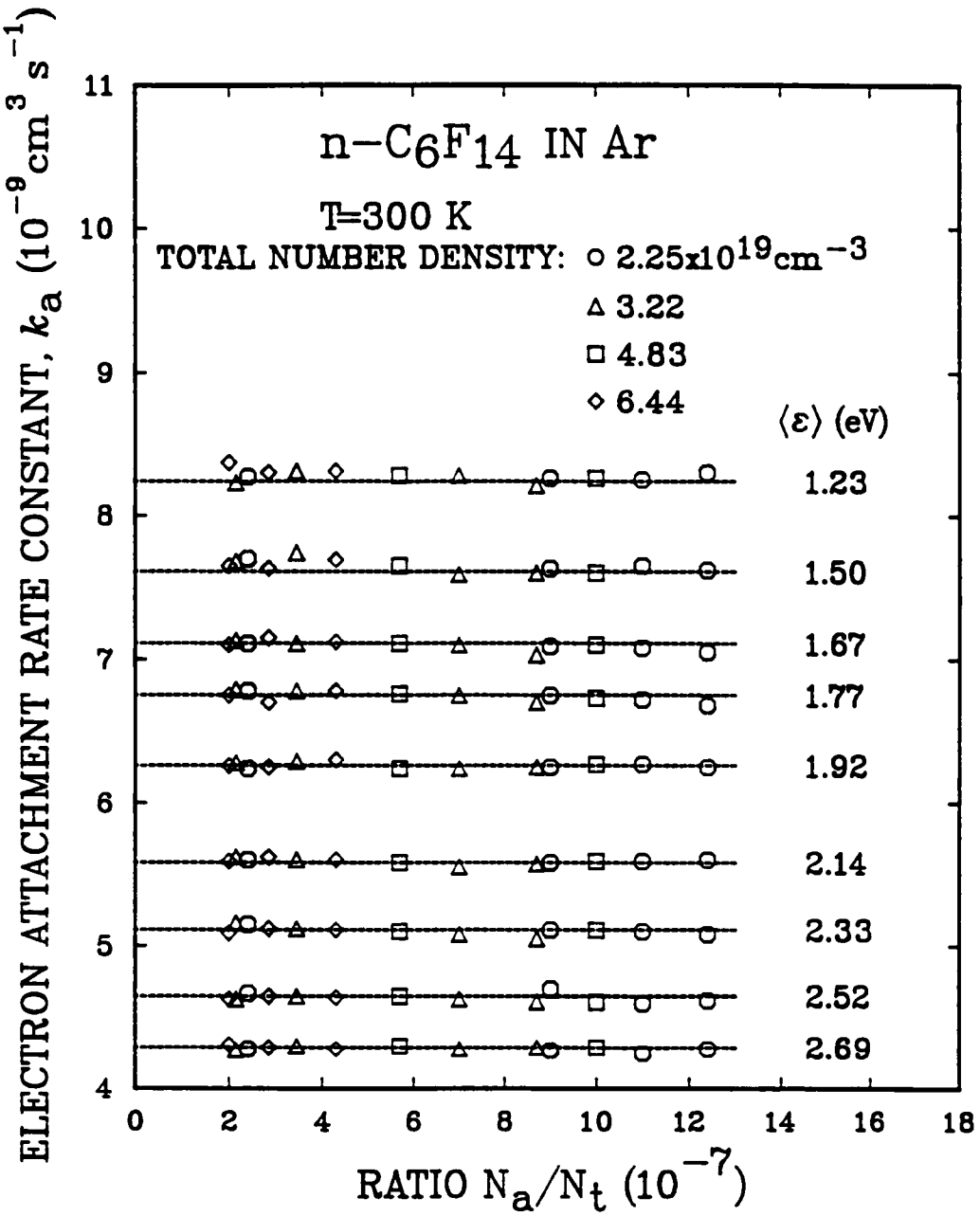

Figure 3.2: Total electron attachment rate constant $k_a(\langle\epsilon\rangle, T)$ for n-C_6F_{14} in Ar as a function of the ratio of the attaching gas number density N_a to the total gas number density N_t for several values of the mean electron energy $\langle\epsilon\rangle$. [$T = 300$ K and at total gas densities 2.25×10^{19} (o), 3.22×10^{19} (Δ), 4.83×10^{19} (□), and 6.44×10^{19} (◇) $molecules/cm^{-3}$].

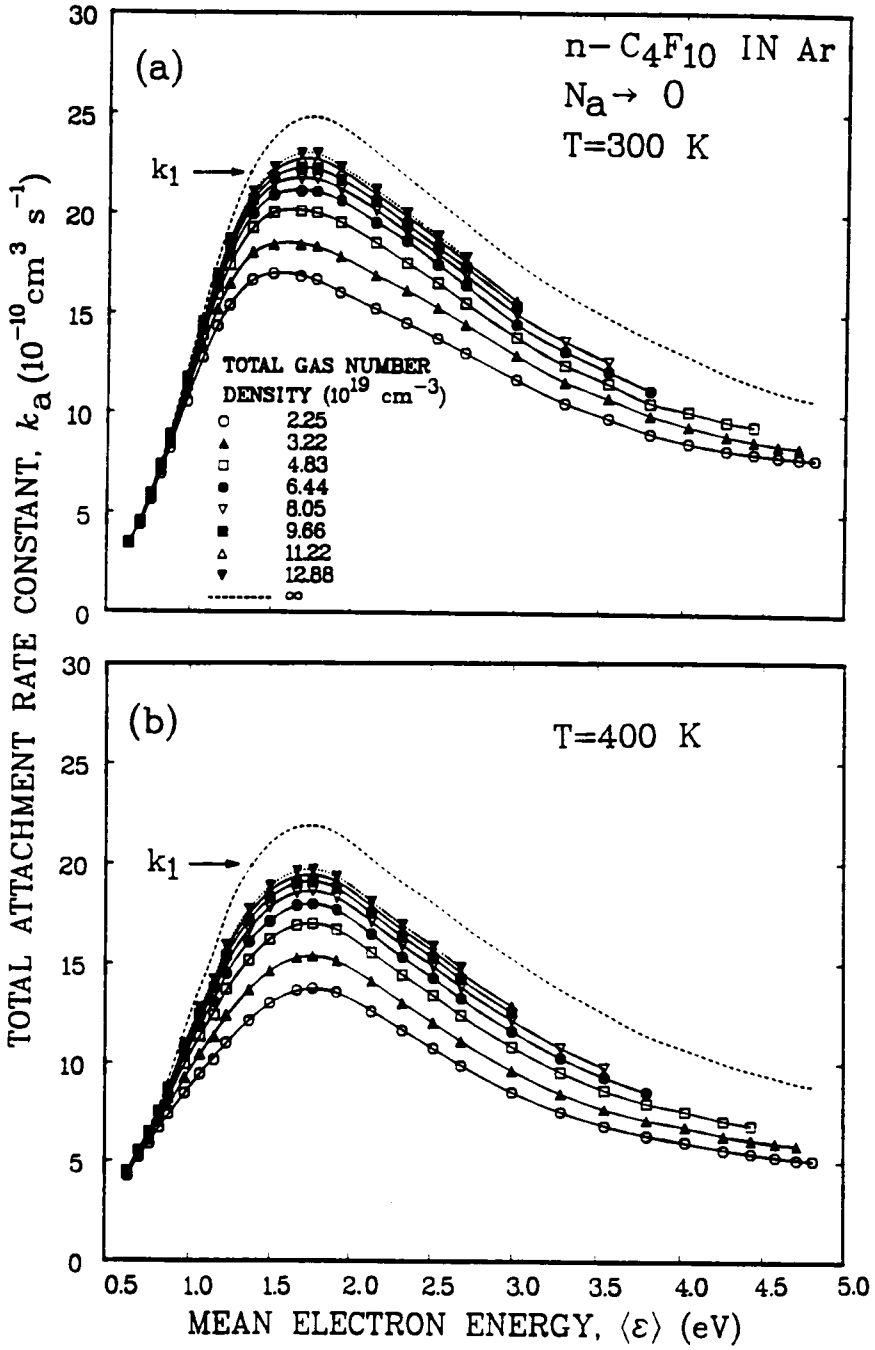

Figure 3.3: Total electron attachment rate constant $k_a(\langle\epsilon\rangle, T)$ (for $N_a \longrightarrow 0$) for n-C_4F_{10} as a function of the mean electron energy $\langle\epsilon\rangle$ and total gas number density N_t at (a) $T = 300\ K$ and (b) $T = 400\ K$. The broken curve shows the electron attachment rate constant k_1 for $N_t \longrightarrow \infty$.

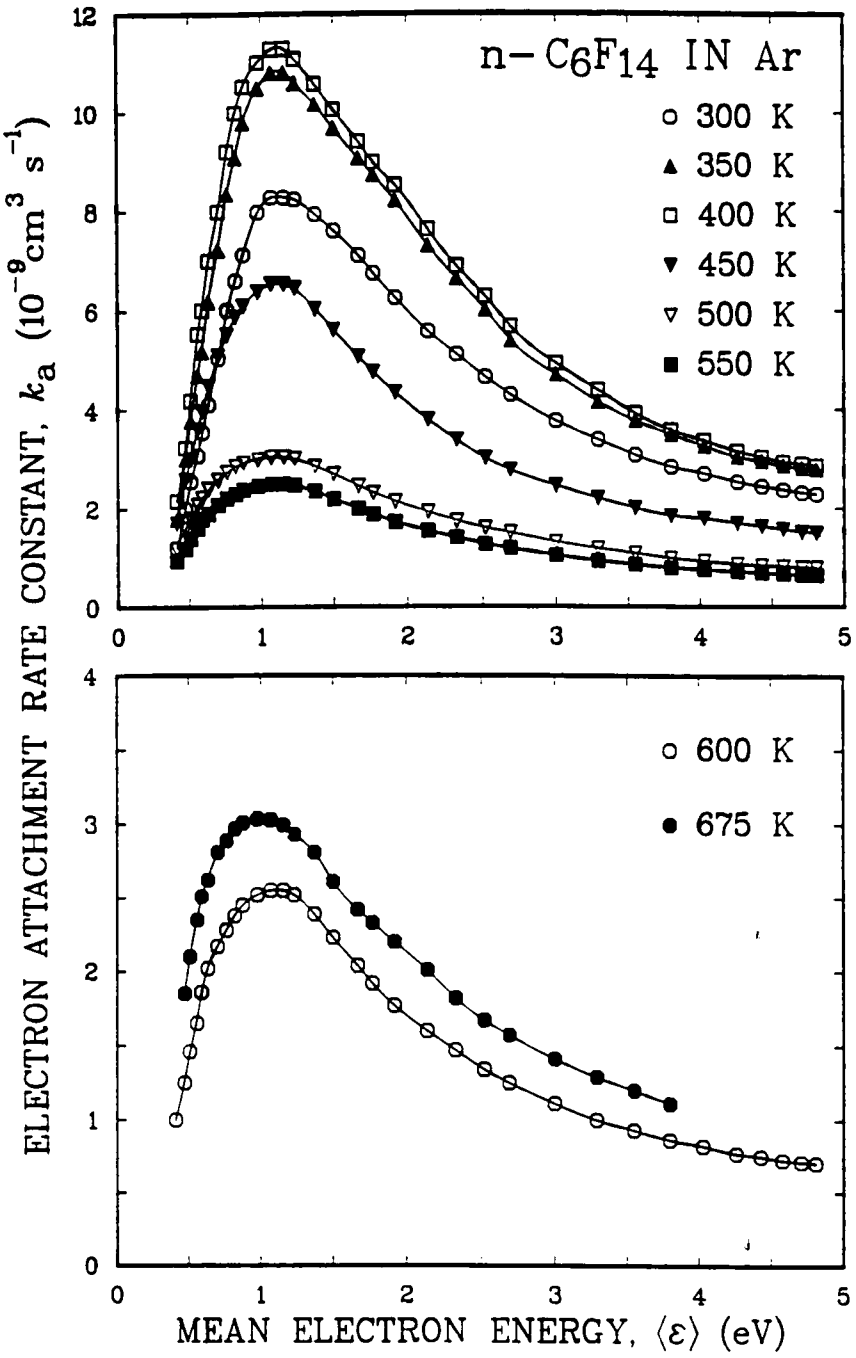

Figure 3.4: The total electron attachment rate constant $k_a(\langle\epsilon\rangle, T)$ (for $N_a \longrightarrow 0$) for n-C_6F_{14} as a function of the mean electron energy $\langle\epsilon\rangle$ at 300, 350, 400, 450, 500, 600, and 675 K.

From sets of data such as in Fig. 3.3 the value $k_1(\langle\epsilon\rangle, T)$ of $k_a(\langle\epsilon\rangle, T)$ (for n–C_4F_{10}) for $N_t \longrightarrow \infty$ was determined at each T. These values are shown in Fig. 3.3 by the broken curves and are listed in Table 3.1. They are also plotted in Fig. 3.5a for T = 300, 350, 400, 450, and 500 K. In Fig. 3.5b the $k_1(\langle\epsilon\rangle, T)$ for T = 600, 675, and 750 K are plotted but since at these temperatures the electron attachment is entirely dominated by the dissociative component, these rates are equal to the measured $k_a(\langle\epsilon\rangle, T)$ at all N_t. The broken curves in Fig. 3.5b for 300, 400, and 500 K are the dissociative electron attachment component of the rate constant (deduced as discussed in section 3.4) at these temperatures. In Fig. 3.4 the $k_a(\langle\epsilon\rangle, T)$ for n–C_6F_{14} are shown, which although are N_t independent, are dominated by the nondissociative electron attachment component at $T \leq 550$ K.

Clearly, the total electron attachment rate constant initially decreases with T above ambient temperatures and then increases. The initial increase in $k_a(\langle\epsilon\rangle, T)$ with temperature for n–C_6F_{14} between 300 and 400 K (see Table 3.2) is due to the dissociative electron attachment which results in the formation of the fragment negative ions (see Spyrou *et al.*, 1983). As was found earlier by Spyrou and Christophorou (1983b) for C_3F_8, the decrease in $k_a(\langle\epsilon\rangle, T)$ with T is due to the decrease with T of the nondissociative part of the electron attachment and the increase with T is due to the increase of the dissociative electron attachment component with increasing T; the contribution of the latter process increases with increasing T and dominates for $T \geq 500$ K in the case of n–C_4F_{10} and for $T \geq 550$ K in the case of n–C_6F_{14}.

Table 3.1: Total electron attachment rate constants, $k_1(\langle\epsilon\rangle, T)$, for $n-C_4F_{10}$ in Ar

	$T = 300\ K$		$k_1(10^{-10}cm^3/s)$							
E/N	$\langle\epsilon\rangle$	w	$T(K)$							
$(10^{-18}Vcm^2)$	(eV)	$(10^5cm/s)$	300	350	400	450	500	600	675	750
0.62	0.63	1.44	3.50	3.60	455		0.30			
0.78	0.70	1.53	4.60	4.70	5.61	1.40	0.46			
0.93	0.76	1.61	6.00	6.09	6.60	1.95	0.62			
1.09	0.82	1.68	7.50	7.58	7.80	2.35	0.74	0.90	1.57	2.75
1.24	0.88	1.75	9.05	9.14	9.11	2.90	0.88	1.10	2.00	3.60
1.55	0.98	1.87	12.10	12.30	11.70	3.92	1.22	1.75	3.05	5.20
1.86	1.07	1.95	15.00	15.10	13.80	4.97	1.54	2.40	3.90	6.50
2.17	1.15	2.03	17.65	17.60	15.50	5.85	1.89	2.95	4.85	7.80
2.49	1.23	2.10	19.60	19.60	17.60	6.71	2.29	3.50	5.60	8.60
3.11	1.37	2.22	22.30	22.30	19.70	8.01	2.82	4.30	6.75	10.00
3.73	1.50	2.33	23.72	23.50	21.00	9.01	3.41	5.10	7.59	11.00
4.66	1.67	2.46	24.75	24.40	21.81	9.82	3.97	5.90	8.30	11.70
5.28	1.77	2.54	24.80	24.45	21.88	10.01	4.20	6.25	8.60	11.95
6.21	1.92	2.64	24.30	23.99	21.51	9.98	4.40	6.65	8.85	12.05
7.77	2.14	2.79	23.00	22.55	20.25	9.25	4.54	6.80	8.90	11.85
9.32	2.33	2.92	21.75	21.25	19.03	8.57	4.56	6.75	8.75	11.50
11.0	2.52	3.04	20.55	20.19	18.00	7.96	4.53	6.55	8.40	11.00
12.4	2.69	3.14	19.46	19.08	16.95	7.48	4.44	6.31	8.07	10.55
15.5	3.00	3.33	17.50	17.21	15.25	6.61	4.20	5.90	7.45	9.80
18.6	3.29	3.49	15.95	15.55	13.70	5.98	3.94	5.50	6.95	9.08
21.7	3.55	3.63	14.80	14.31	12.53	5.45	3.91	5.20	6.50	8.50
24.9	3.80	3.76	13.69	13.30	11.41	5.01	3.49	4.90	6.10	8.00
27.9	4.03	3.88	12.88	12.48	10.71	4.75	3.33	4.65	5.80	
31.1	4.26	3.99	12.00	11.65	10.01	4.51	3.16	4.45	5.50	
34.2	4.43	4.18	11.52	11.16	9.60	4.35	3.07	4.30	5.30	
37.3	4.58	4.38	11.11	10.71	9.30	4.25	2.99	4.20	5.18	
40.4	4.71	4.62	10.83	10.52	9.00	4.15	2.94	4.12	5.10	
43.5	4.81	4.90	10.71	10.38	8.88	4.10	2.92	4.08		

Table 3.2: Total electron attachment rate constants, $k_a(\langle\epsilon\rangle, T)$, for $n-C_6F_{14}$ in Ar

	$T = 300\ K$		$k_a(10^{-9}cm^3/s)$							
E/N	$\langle\epsilon\rangle$	w	$T(K)$							
$(10^{-18}Vcm^2)$	(eV)	$(10^5cm/s)$	300	350	400	450	500	550	600	675
0.22	0.41	1.10	1.20	1.79	2.16	1.71	1.19	0.95	1.00	
0.31	0.47	1.20	2.00	3.01	3.24	2.59	1.60	1.19	1.25	1.85
0.37	0.51	1.26	2.55	3.78	4.19	3.01	1.81	1.40	1.46	2.10
0.47	0.56	1.34	3.08	4.70	5.54	3.61	2.09	1.61	1.65	2.35
0.53	0.59	1.38	3.55	5.18	6.02	3.98	2.23	1.79	1.86	2.51
0.62	0.63	1.44	4.11	6.19	7.01	4.49	2.41	1.90	2.02	2.62
0.78	0.70	1.53	5.04	7.23	8.00	5.11	2.59	2.08	2.17	2.81
0.93	0.76	1.61	6.02	8.35	9.21	5.53	2.75	2.21	2.28	2.89
1.09	0.82	1.68	6.61	9.08	10.00	5.89	2.87	2.30	2.38	2.38
1.24	0.88	1.75	7.13	9.79	10.53	6.11	2.94	2.38	2.45	3.01
1.55	0.98	1.87	7.98	10.49	11.02	6.39	3.00	2.46	2.52	3.04
1.86	1.07	1.95	8.28	10.81	11.29	6.55	3.05	2.51	2.55	3.03
2.17	1.15	2.03	8.28	10.81	11.30	6.55	3.05	2.51	2.55	2.99
2.49	1.23	2.10	8.24	10.59	11.09	6.46	3.01	2.47	2.52	2.93
3.11	1.37	2.22	7.94	10.17	10.58	6.05	2.85	2.35	2.39	2.81
3.73	1.50	2.33	7.61	9.68	10.06	5.62	2.70	2.19	2.23	2.61
4.66	1.67	2.46	7.11	9.07	9.41	5.08	2.46	2.00	2.04	2.42
5.28	1.77	2.54	6.75	8.73	8.99	4.76	2.31	1.88	1.92	2.33
6.21	1.92	2.64	6.26	8.21	8.52	4.34	2.14	1.72	1.77	2.20
7.77	2.14	2.79	5.58	7.30	7.63	3.79	1.93	1.54	1.60	2.01
9.32	2.33	2.92	5.11	6.64	6.89	3.38	1.74	1.41	1.47	2.82
11.0	2.52	3.04	4.65	6.01	6.28	3.01	1.60	1.27	1.34	1.67
12.4	2.69	3.14	4.29	5.39	5.68	2.77	1.51	1.19	1.25	1.57
15.5	3.00	3.33	3.76	4.70	4.93	2.46	1.32	1.05	1.11	1.41
18.6	3.29	3.49	3.39	4.15	4.39	2.21	1.19	0.94	1.00	1.29
21.7	3.55	3.63	3.08	3.77	3.92	2.01	1.09	0.87	0.93	1.20

Table 3.2: (Continued)

	$T = 300\ K$		$k_a(10^{-9}cm^3/s$							
E/N	$\langle\epsilon\rangle$	w	$T(K)$							
$(10^{-18}Vcm^2)$	(eV)	$(10^5cm/s)$	300	350	400	450	500	550	600	675
24.9	3.80	3.76	2.84	3.49	3.58	1.85	0.99	0.80	0.87	1.11
27.9	4.03	3.88	2.70	3.26	3.37	1.80	0.93	0.76	0.83	
31.1	4.26	3.99	2.53	3.04	3.16	1.70	0.87	0.72	0.78	
34.2	4.43	4.18	2.44	2.95	3.04	1.64	0.84	0.70	0.76	
37.3	4.58	4.38	2.37	2.86	2.94	1.58	0.82	0.67	0.73	
40.4	4.71	4.62	2.31	2.81	2.90	1.52	0.80	0.65	0.72	
43.5	4.81	4.90	2.28	2.78	2.86	1.50	0.79	0.64	0.71	

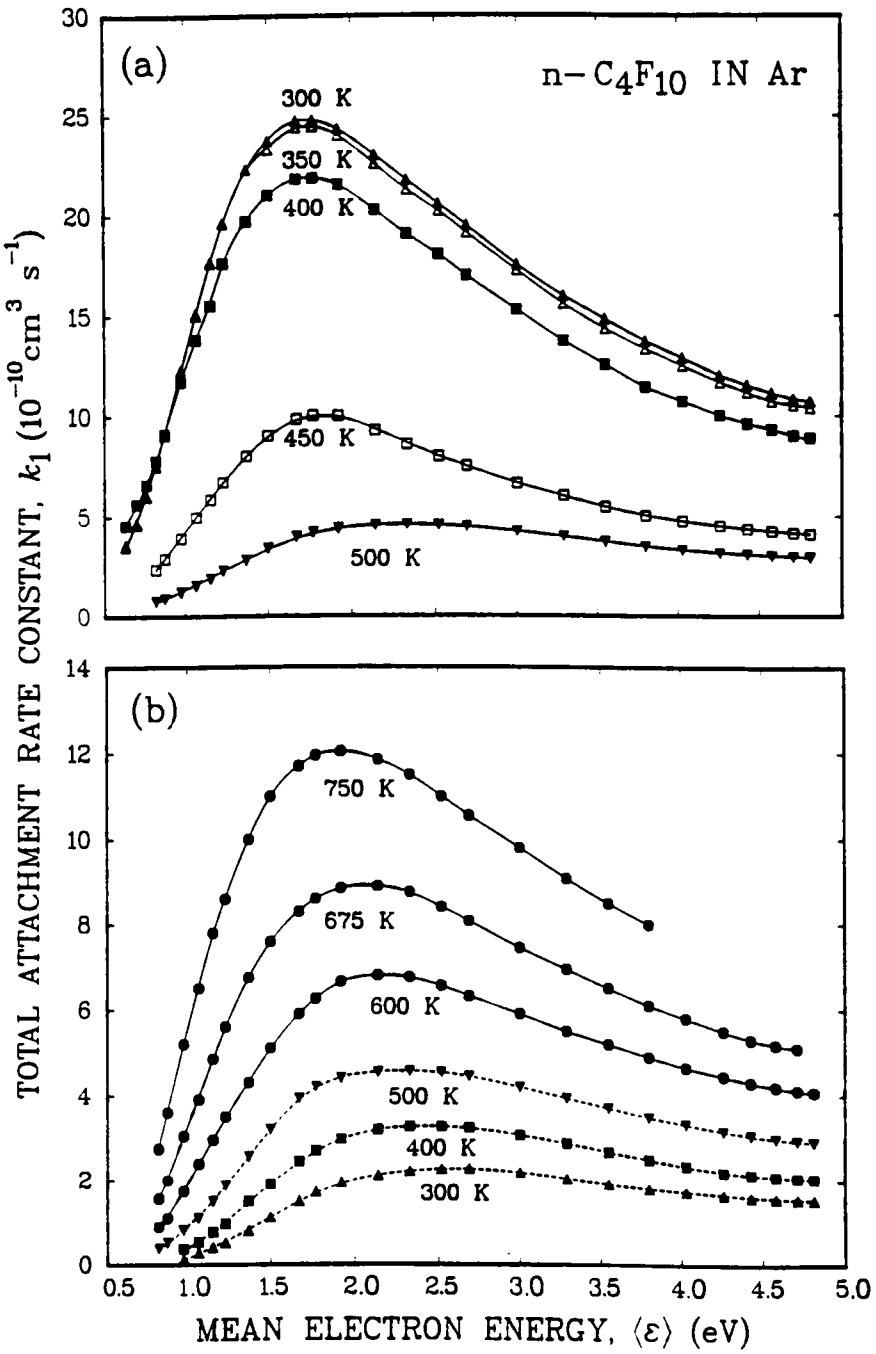

Figure 3.5: The total electron attachment rate constant $k_1(\langle\epsilon\rangle, T)$ (for $N_a \longrightarrow 0$, $N_t \longrightarrow \infty$) for n-C_4F_{10} as a function of the mean electron energy $\langle\epsilon\rangle$ at (a) 300, 350, 400, 450, and 500 K and (b) 600, 675, and 750 K. The 300, 400, and 500 K curves in (b) are the dissociative attachment components $(k_a)_d(\langle\epsilon\rangle, T)$ of the total rate constant $k_1(\langle\epsilon\rangle, T)$ at these temperatures.

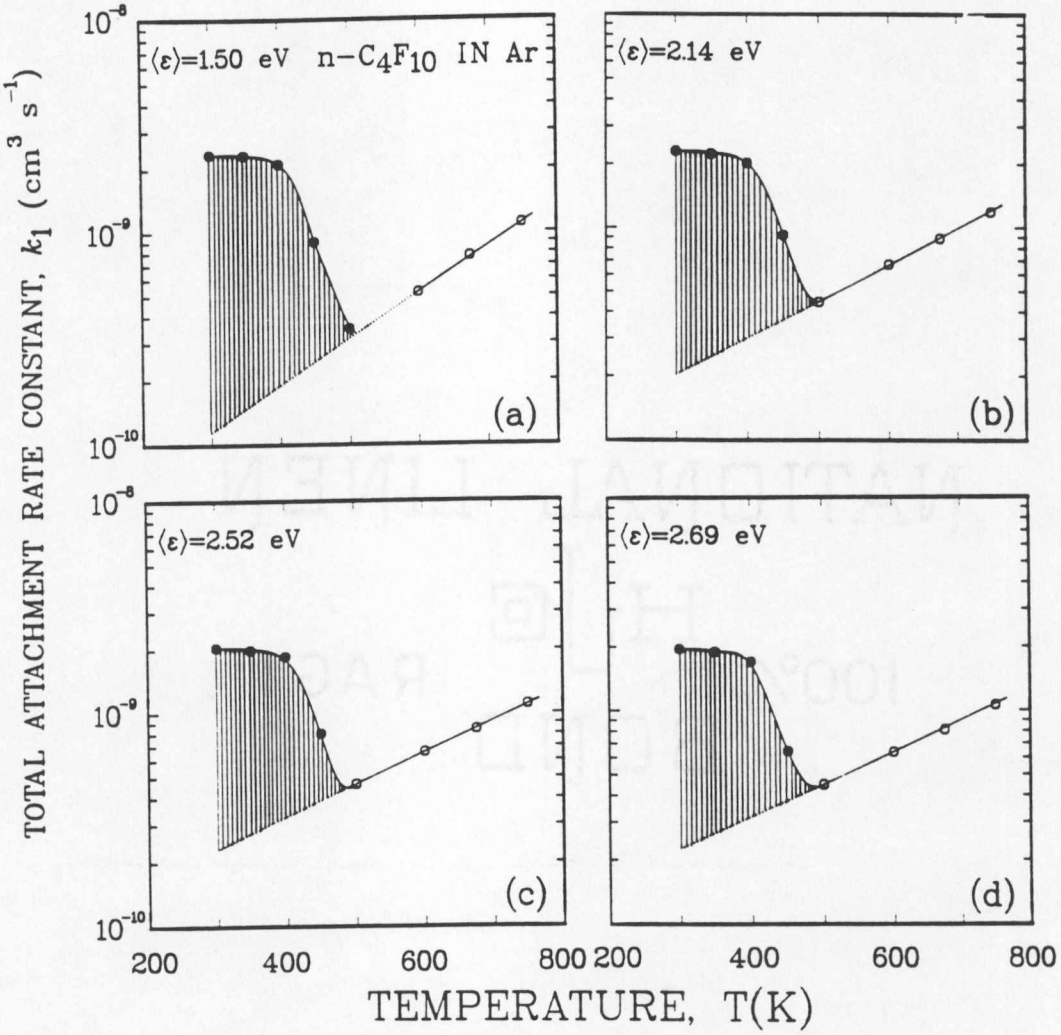

Figure 3.6: Total electron attachment rate constant $k_1(\langle\epsilon\rangle, T)$ (for $N_a \longrightarrow 0$, $N_t \longrightarrow \infty$) for n-C_4F_{10} as a function of temperature T and the mean electron energies $\langle\epsilon\rangle$: 1.50, 2.14, 2.52, and 2.69 eV.

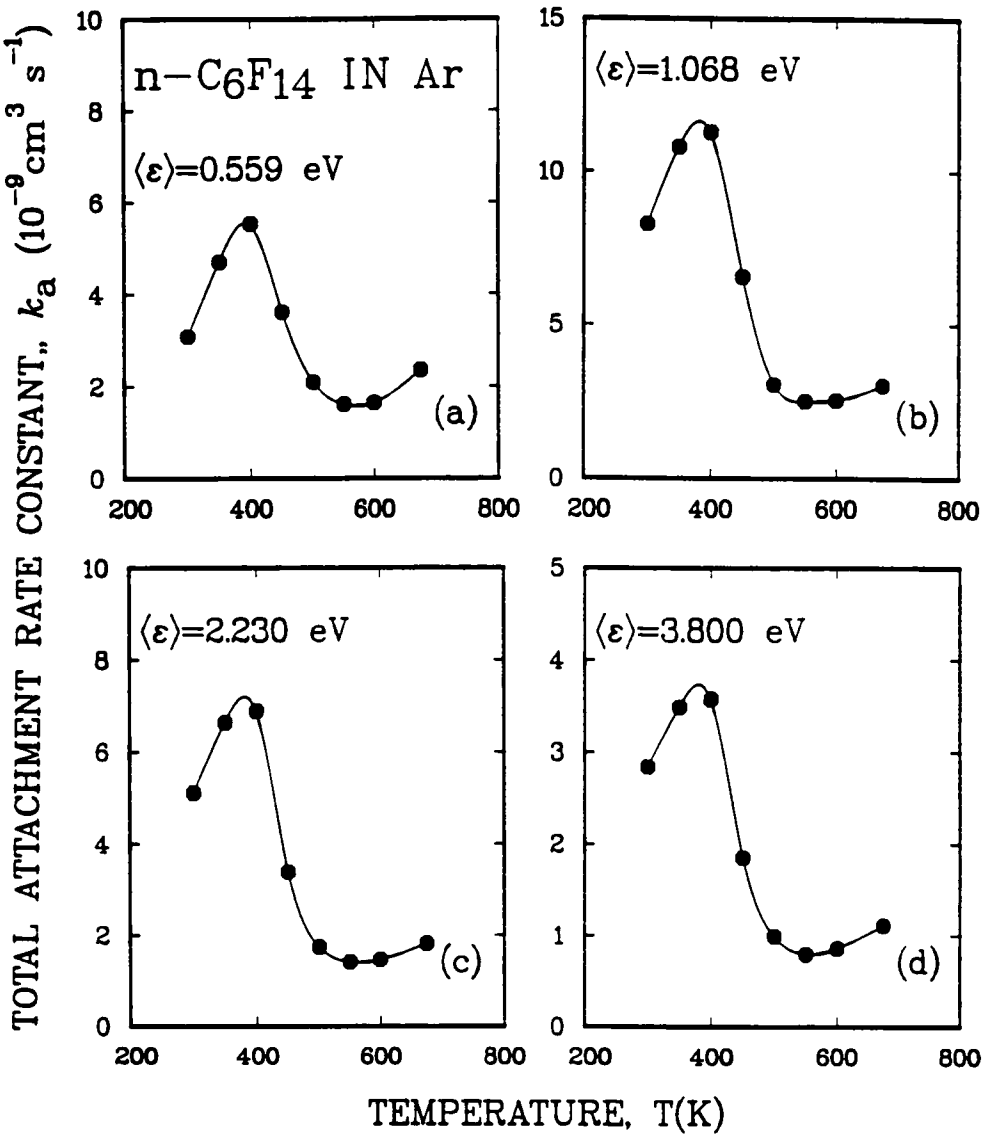

Figure 3.7: Total electron attachment rate constant $k_a(\langle\epsilon\rangle, T)$ (for $N_a \longrightarrow 0$) for n-C_6F_{14} as a function of temperature T and the mean electron energies $\langle\epsilon\rangle$: 0.559, 1.068, 2.23, and 3.80 eV.

As a result of the delicate temperature dependencies of the dissociative and nondissociative contributions to the total attachment, the position of the maximum of total electron attachment rate constant changes little with increases in T as long as the nondissociative contibution is large, and it shifts to lower electron energies with increasing T when the dissociative electron attachment contribution predominates (see Figs. 3.4 and 3.5). These delicate effects of T on $k_1(\langle\epsilon\rangle, T)$ and the relative contribution to $k_1(\langle\epsilon\rangle, T)$ of the dissociative and nondissociative processes are further illustrated by the data in Figs. 3.6 and 3.7 where $k_1(\langle\epsilon\rangle, T)$ is plotted as a function of T for different values of $\langle\epsilon\rangle$. For $n-C_4F_{10}$, at high $T \geq 500\ K$ the logarithm of $k_1(\langle\epsilon\rangle, T)$ increases almost linearly with T and is N_t independent. These findings coupled with earlier knowledge on the effect of temperature on dissociative electron attachment (O'Malley, 1967; Smirnov, 1982; Christophorou *et al.*, 1984, 1987; Spyrou and Christophorou, 1985b), show that the linearly rising portion of $\log(k_1)$ for $T \geq 500\ K$ is due to dissociative electron attachment processes. The data on $\log(k_1(\langle\epsilon\rangle, T))$ for $T \geq 500\ K$ in plots such as in Fig. 3.6 were fitted to a straight line and extrapolated to 300 K. In this way the dissociative $(k_a)_d$ and the nondissociative $(k_a)_{nd}$ (shaded areas in Fig. 3.6), component of $k_1(\langle\epsilon\rangle, T)$ at each $\langle\epsilon\rangle$ were determined, (see section 3.4 for another way to determine the two components, which gave results consistent with the extrapolation method). Examples of the variation of $(k_a)_d$ and $(k_a)_{nd}$ with T determined in this way for $n-C_4F_{10}$ are shown in Fig. 3.8 for four values of $\langle\epsilon\rangle$. In Fig. 3.9, the $(k_a)_{nd}$ is shown for 300, 350, 400, and 450 K. The dramatic decrease of $(k_a)_{nd}(\langle\epsilon\rangle, T)$ with T is but apparent.

3.3.2 Swarm-Unfolded Electron Attachment Cross Sections

The total electron attachment rate constants for $n-C_4F_{10}$ (in Fig. 3.5) and for $n-C_6F_{14}$ (in Fig 3.4) were unfolded and the total electron attachment cross section $\sigma_a(\epsilon, T)$ obtained are shown in Figs. 3.10 and 3.11. For $n-C_4F_{10}$, the $\sigma_a(\epsilon, T)$ decreases in magnitude with increasing T between 300 and 500 K (see Fig. 3.10a),

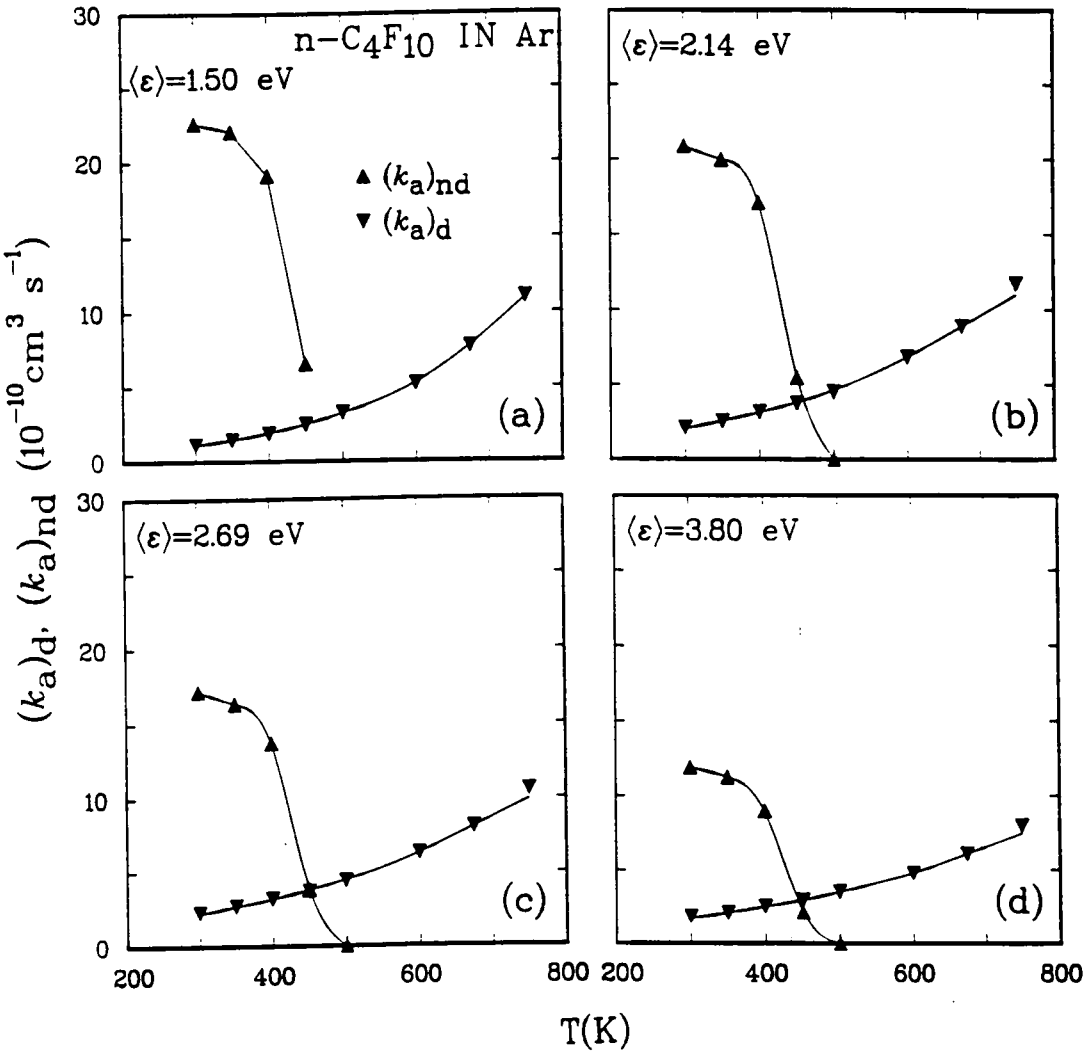

Figure 3.8: The electron attachment rate constant $(k_a)_d$ and $(k_a)_{nd}$ of n-C_4F_{10} due, respectively, to dissociative and nondissociative electron attachment as a function of the temperature T at the mean electron energies $\langle\epsilon\rangle$: 1.50, 2.14, 2.69, and 3.80 eV.

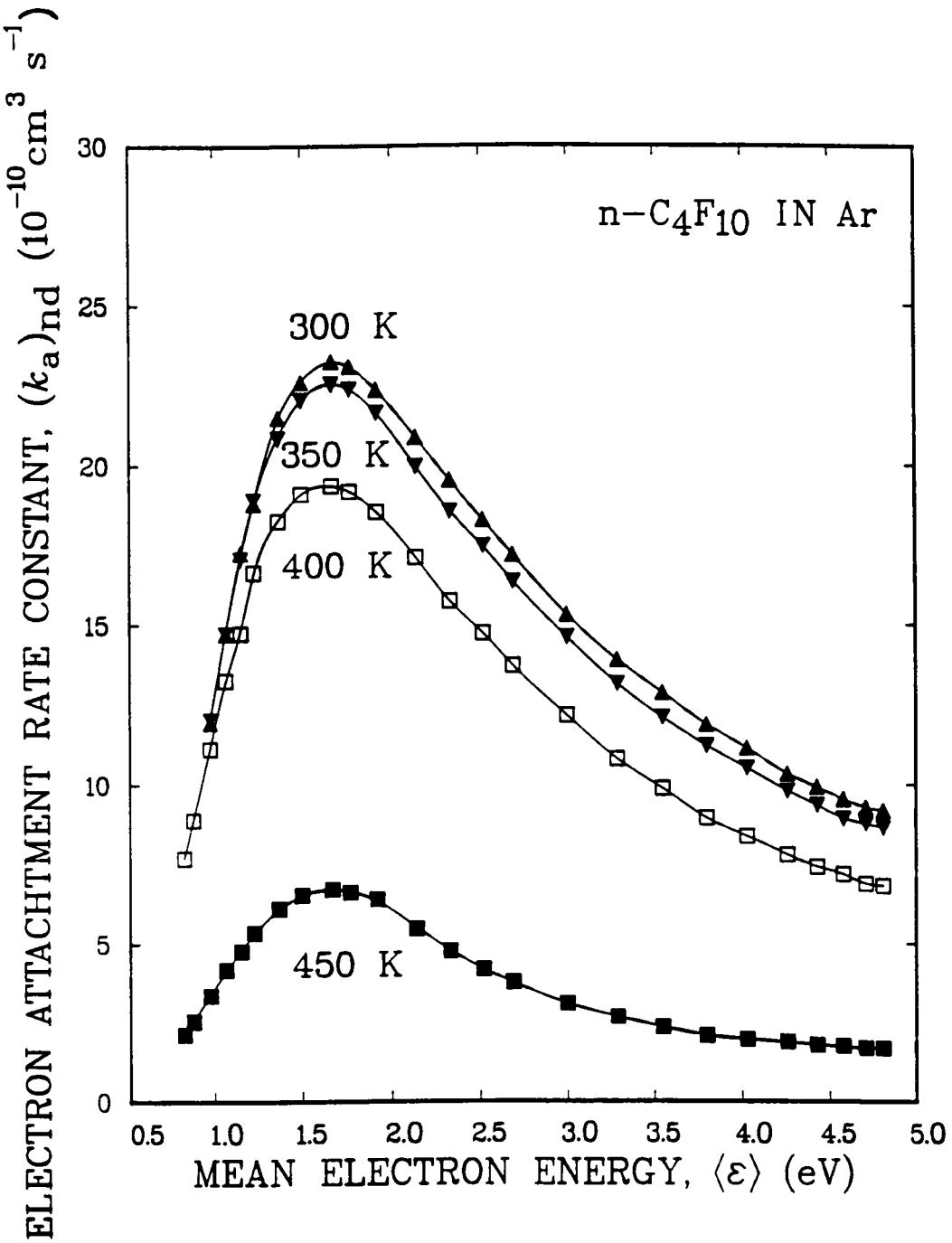

Figure 3.9: Electron attachment rate constant $(k_a)_{nd}$ for n-C_4F_{10} due to nondissociative attachment as a function of the mean electron energy at 300, 350, 400, and 450 K.

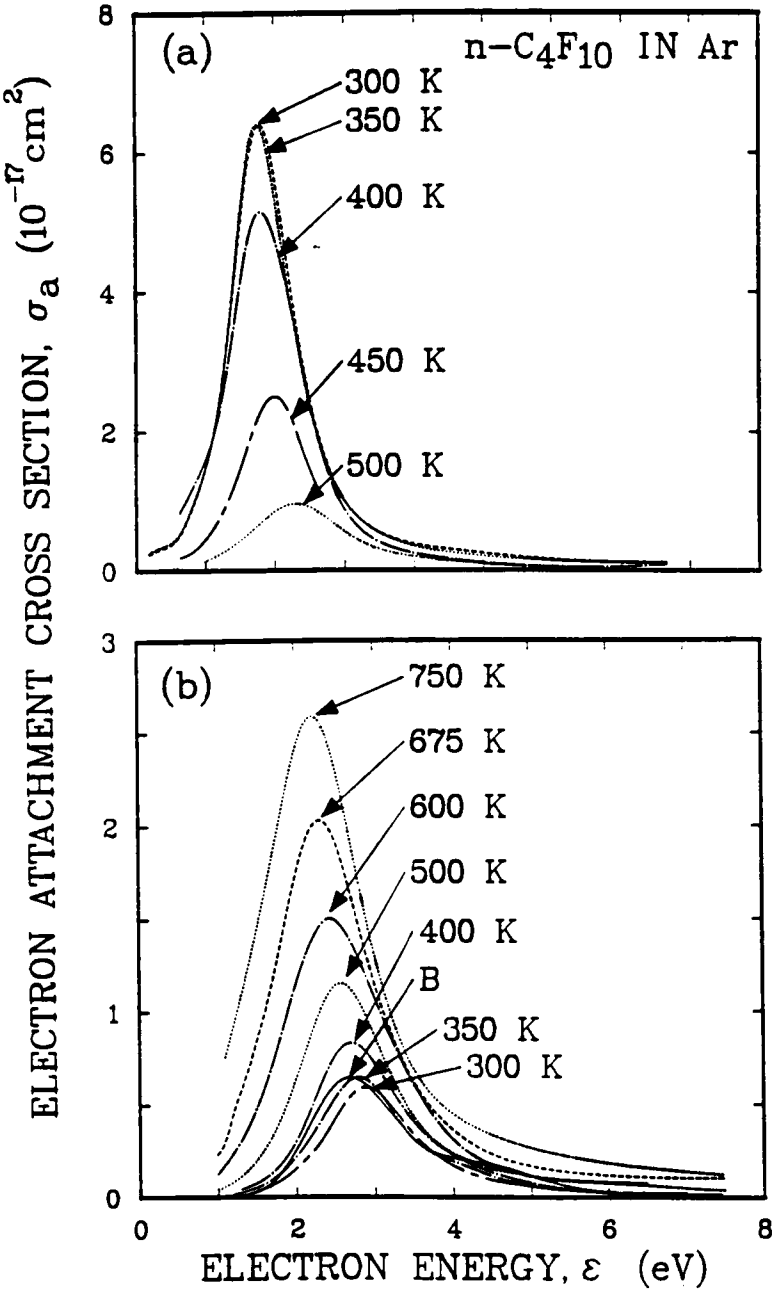

Figure 3.10: The swarm unfolded total electron attachment cross sections $\sigma_a(\epsilon, T)$ for n-C_4F_{10} obtained using the $k_1(\langle\epsilon\rangle)$ in Ar shown in Fig. 3.5 at (a) 300, 350, 400, 450, and 500 K and (b) 600, 675, and 750 K. The 300, 350, 400, and 500 K curves (b) are the dissociative attachment cross sections $(\sigma_a)_d(\epsilon, T)$ at these temperatures. In Fig. 3.10 (b) is plotted also the total relative cross section measured in an electron beam experiment (Spyrou *et al.*, 1983) (curve B) which has been normalized to the peak of the $(\sigma_a)_d(\epsilon, T)$ at 350 K (see the text).

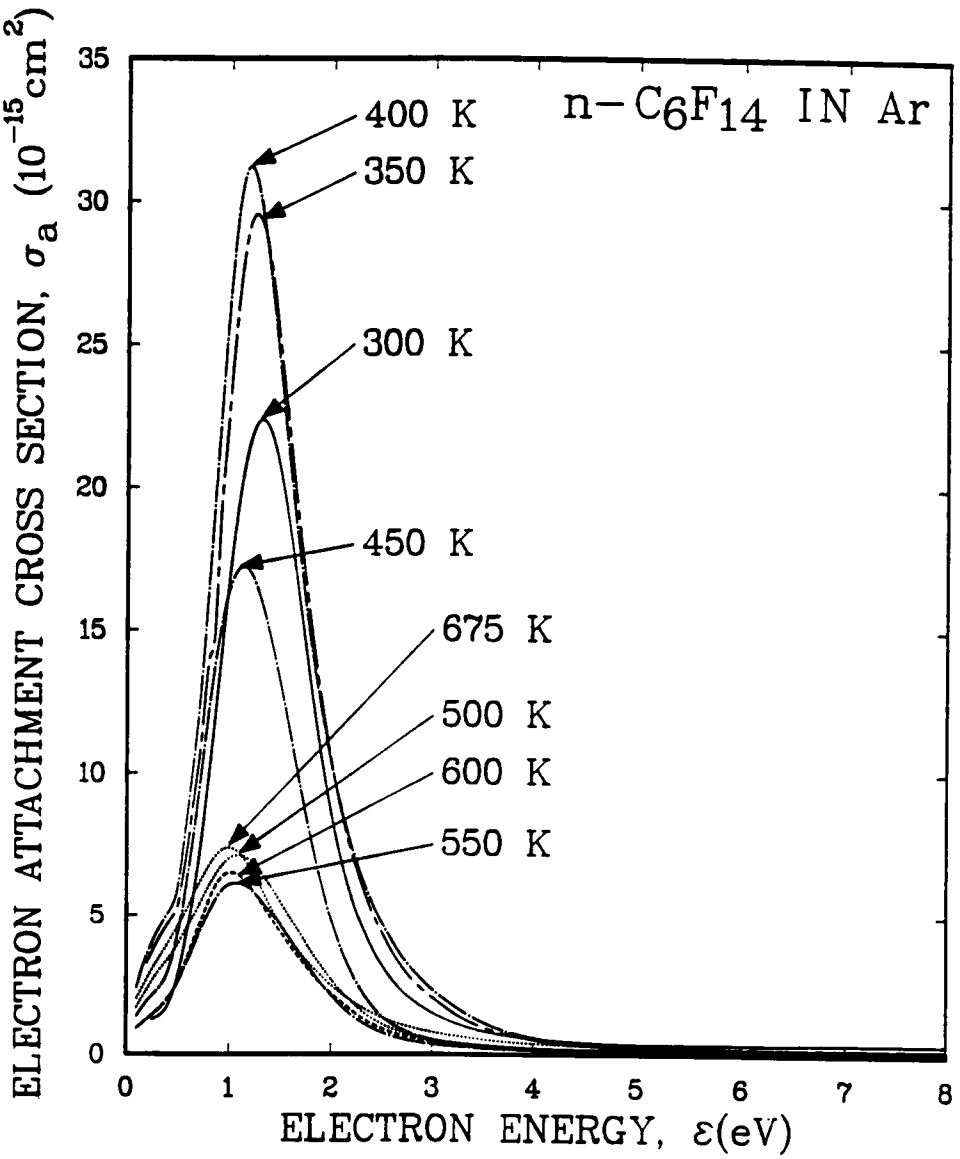

Figure 3.11: The swarm unfolded electron attachment cross sections $\sigma_a(\epsilon, T)$ for n-C_6F_{14} obtained using the $k_a(\langle\epsilon\rangle, T)$ in Ar shown in Fig. 3.4 at 300, 350, 400, 450, 500, 600, and 675 K (see the text).

because in this temperature range the electron attachment cross section contains a large contribution (which increases as T increases) from a nondissociative electron attachment process. Very interestingly, however, the $\sigma_a(\epsilon, T)$ for this molecule peaks at progressively higher ϵ in this temperature range reflecting the depletion of the parent and the preponderance of the fragment anions as T increases. In Fig. 3.10b the electron attachment cross sections $\sigma_a(\epsilon, T)$ for n–C_4F_{10} increases with increasing T and — as indicated by the data in Fig. 3.6 — it is entirely due to dissociative electron attachment. Also shown in Fig. 3.10b are the dissociative electron attachment cross section $(\sigma_a)_d(\epsilon, T)$ for 300, 350, 400, 450, and 500 K which were obtained by unfolding only the $(k_a)_d(\langle\epsilon\rangle, T)$ component of the total electron attachment rate constant. The curve B in Fig. 3.10b is the total (for all fragment anions) $(\sigma_a)_d(\epsilon, T)$ for n–C_4F_{10} as measured by Spyrou *et al.*, (1983) in an electron-beam study, normalized to the swarm unfolded $(\sigma_a)_d(\epsilon, T)$ at 350 K.

In Fig. 3.11 the total electron attachment cross section for n–C_6F_{14}, first increases with T between 300 and 400 K, due to a contribution from a dissociative electron attachment process, and in this temperature range the peak of $\sigma_a(\epsilon, T)$ shifts to progressively lower ϵ. Then it decreases precipitously between 400 and 500 K, reflecting a large contribution from a nondissociative process. Subsequently it starts increasing for $T \geq 550$ K, as higher-lying dissociative electron attachment processes predominate; in this temperature range, as expected, the peak of the energy position shifts to lower electron energies. The behavior of $(\sigma_a)_d(\epsilon, T)$ for n–C_4F_{10} and n–C_6F_{14} is consistent with that of the $(\sigma_a)_d(\epsilon, T)$ of other molecules with purely dissociative electron attachment processes (see, for example, Smirnov, 1982; Spyrou and Christophorou 1985b; Christophorou, 1987) its magnitude and width increase and its peak energy position ϵ_{max} and onset shift to lower energies with increasing T. In Fig. 3.12 (see also Table 3.3) are shown the observed dependencies of the Full Width at Half Maximum (FWHM), the peak energy position (ϵ_{max}) and the magnitude of $(\sigma_a)_d(\epsilon_{max}, T)$ on the temperature for n–C_4F_{10}. It is clear that the FWHM increases with increasing T, demonstrating the broadening of the Franck-Condon region due to the population of higher vibrational states

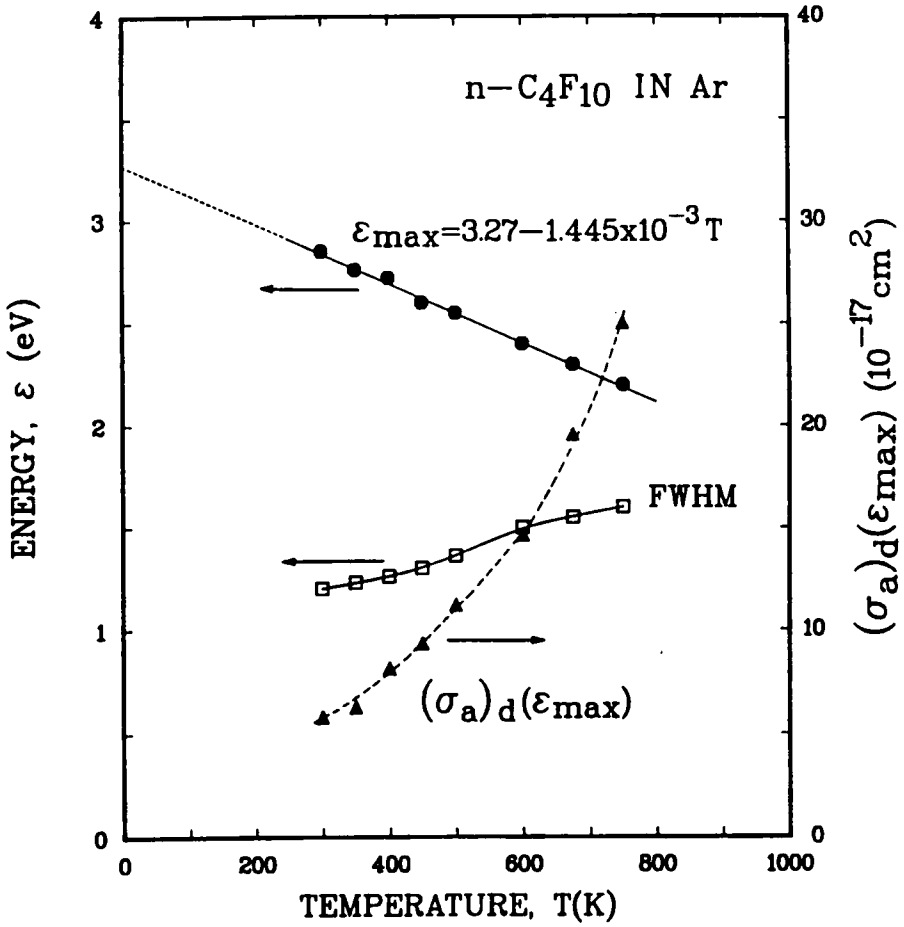

Figure 3.12: Variation of the peak energy ϵ_{max}, full width at half-maximum (FWHM), and peak value $(\sigma_a)_d(\epsilon_{max}, T)$ of the dissociative electron attachment cross section of n-C_4F_{10} with temperature.

Table 3.3: Values of FWHM, ϵ_{max} and $(\sigma_a)_d(\epsilon_{max}, T)$ for the $(\sigma_a)_d(\epsilon, T)$ of $n-C_4F_{10}$

T	FWHM	ϵ_{max}	$(\sigma_a)_d(\epsilon_{max})$
(K)	(eV)	(eV)	$(10^{-17}cm^2)$
300	1.20	2.85	6.00
350	1.23	2.76	6.50
400	1.26	2.72	8.44
450	1.30	2.60	9.70
500	1.36	2.55	11.65
600	1.50	2.40	15.20
675	1.55	2.30	20.32
750	1.60	2.20	26.00

with increasing T. Also the peak energy position shifts toward lower electron energies with increasing T since the negative ion state(s) can be reached with smaller energies from higher vibrational levels.

3.4 Discussion

3.4.1 Variation of the Nondissociative and Dissociative Electron Attachment Processes in $n-C_4F_{10}$ with Electron Energy and Temperature

As discussed in section 3.1, electron swarm and electron beam studies indicated that low-energy electron attachment to $n-C_4F_{10}$ can be described by electron attachment to an attractive negative ion state leading to parent anions and to

repulsive higher-lying negative ion state(s) leading to fragment anions, viz.,

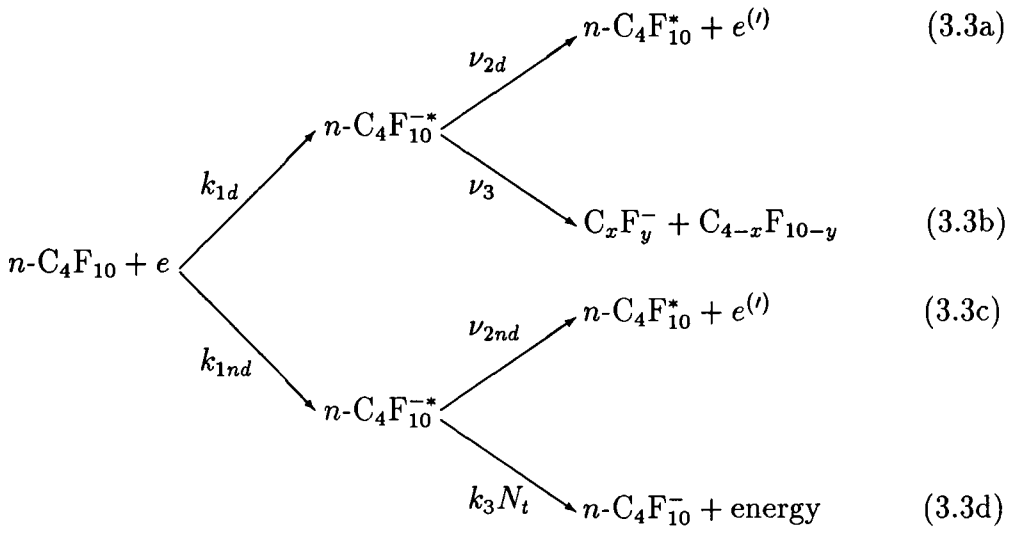

(3.3a)

(3.3b)

(3.3c)

(3.3d)

The $n{-}C_4F_{10}^{-*}$ produced by electron capture into dissociative negative ion state(s) (NISs) with a rate constant k_{1d} decays by autodetachment (process 3.3a) with a rate constant ν_{2d} or dissociates with a rate constant ν_3 to form negative ion and neutral fragments. The $n{-}C_4F_{10}^{-*}$ produced by electron capture into the nondissociative (bound) NIS with a rate constant, k_{1nd}, either decays by autodetachment with a rate constant, ν_{2nd} (average lifetime, τ_a) or is stabilized by collision with another species (in the present experiment by collision with an Ar atom) with a rate constant k_3N_t to form a stable parent anion, $n{-}C_4F_{10}^{-}$ (process 3.3d). If the bound and unbound NISs do not internally convert to each other, the measured total k_a ($\langle\epsilon\rangle$) can be expressed — on the basis of processes 3.3a to 3.3b — by

$$k_a = k_{1d}\frac{\nu_3}{\nu_{2d}+\nu_3} + k_{1nd}\frac{k_3N_t}{\nu_{2nd}+k_3N_t} \tag{3.4}$$

If the contribution to k_a from dissociative electron attachment is negligible, $1/k_a[= 1/(k_a)_{nd}]$ would vary linearly with $1/N_t$, viz.,

$$\frac{1}{(k_a)_{nd}} = \frac{1}{k_{1nd}} + \frac{\nu_{2nd}}{k_{1nd}k_3}\frac{1}{N_t} \tag{3.5}$$

This relationship is indeed obeyed (Fig. 3.13a) for $T = 300\ K$ and $(\epsilon) \leq 1.50$ eV (*i.e.*, under conditions for which nondissociative electron attachment predominates). However, as $\langle\epsilon\rangle$ increases, the contribution of dissociative attachment processes increases, and $1/k_a$ vs $1/N_t$ is no longer linear. As expected this latter type of behavior becomes more pronounced the higher the value of T (compare data in Figs. 3.13a and 3.13b), since the dissociative electron attachment contribution increases with T. If at a given value of T the rate constant $(k_a)_d$ due to the dissociative electron attachment is subtracted from the measured total electron attachment rate constant k_a and the inverse of the resultant nondissociative electron attachment rate constant $(k_a)_{nd}$ is plotted as a function of $1/N_t$, a linear relationship is indeed obtained. This is clearly seen from Fig. 3.14, where the $1/(k_a)_{nd}$ values for 450 K (determined from the respective $1/k_a$ data in Fig. 3.13a) are plotted as a function of $1/N_t$.

It should be pointed out that the $(k_a)_d$ and $(k_a)_{nd}$ components of k_a can be obtained — as in an earlier study by Spyrou and Christophorou (1985b) — by applying a nonlinear least squares fit to Eqn 3.4 (see Fig. 3.15 curve for 450 K). Furthermore, when $N_t \longrightarrow \infty$ (*i.e.*, when all parent and fragment anions are detected), Eqn 3.2 leads to

$$k_a \rightarrow k_{1d}\frac{\nu_3}{\nu_3 + \nu_{2d}} + k_{1nd} = k_1 \tag{3.6}$$

and when $N_t \longrightarrow 0$ (*i.e.*, when only the dissociative attachment fragment anions are detected), it leads to

$$k_a \rightarrow k_{1d}\frac{\nu_3}{\nu_3 + \nu_{2d}} = (k_a)_d \tag{3.7}$$

The ratio of Eqns 3.7 and 3.6 give the ratio $R_{d/t}$ of the dissociative to the total attachment rate constant. In Fig. 3.15 $R_{d/t}$ is plotted as a function of $\langle\epsilon\rangle$ for 300, 350, 400, 450, and 500 K: at low $\langle\epsilon\rangle$ and T the contribution of dissociative electron attachment to the total is small, but it rapidly increases as both $\langle\epsilon\rangle$ and T increase. This type of behavior is both a result of the $\langle\epsilon\rangle$ dependencies of $(k_a)_d$ and $(k_a)_{nd}$ and of the opposite effect of T on $(k_a)_d$ (increasing with T) and $(k_a)_{nd}$ (decreasing with T).

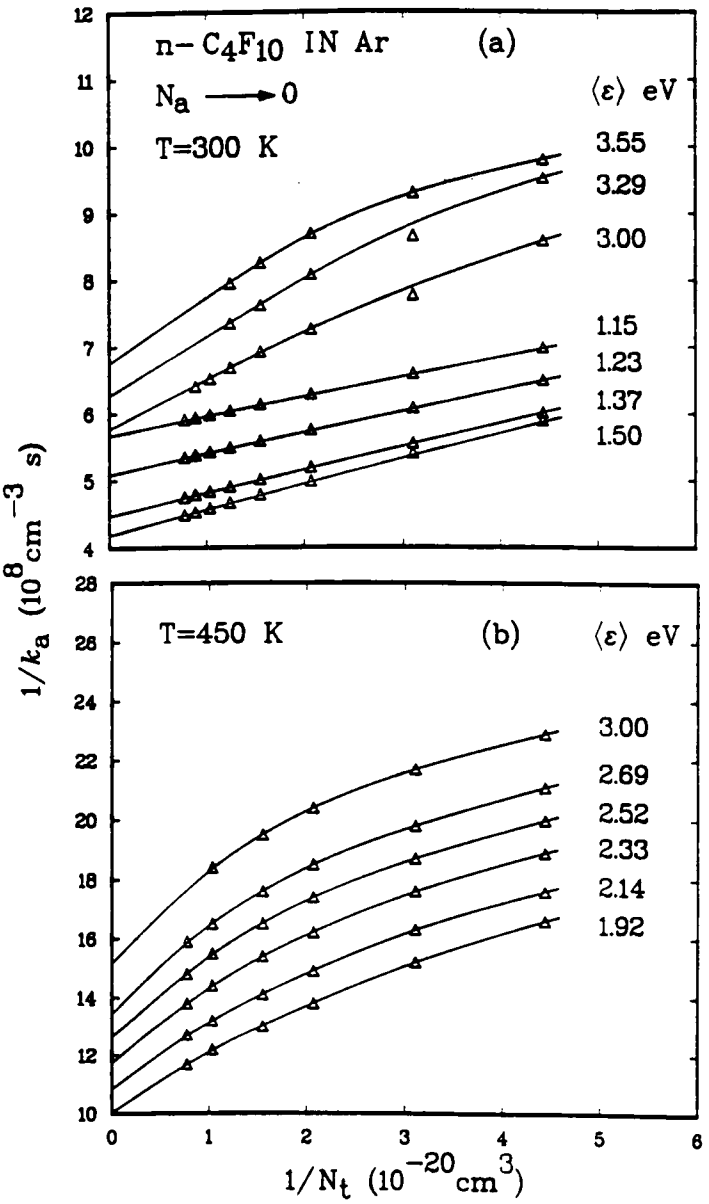

Figure 3.13: $1/k_a$ versus $1/N_t$ for n-C_4F_{10} in Ar at (a) 300 K and (b) 450 K (see the text).

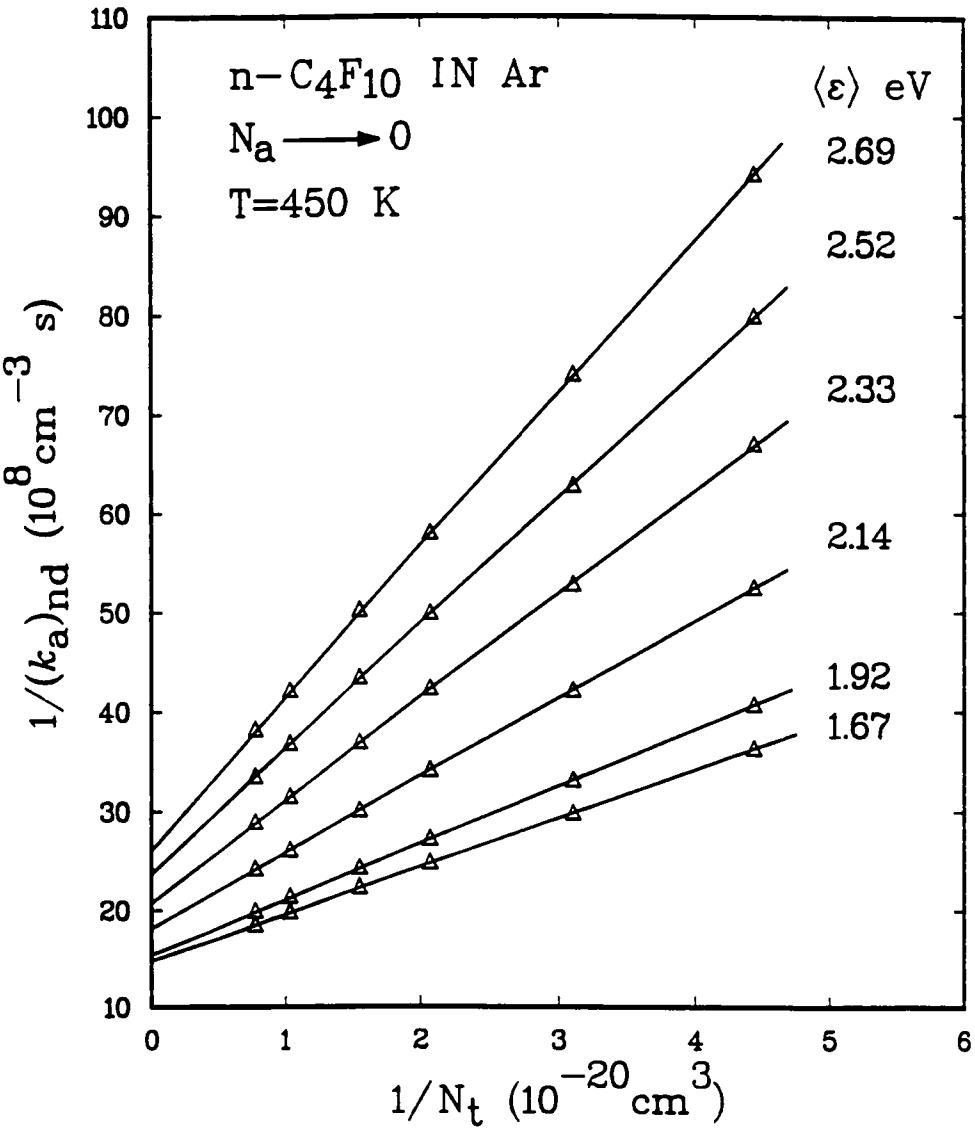

Figure 3.14: $1/(k_a)_{nd}$ versus $1/N_t$ for n-C_4F_{10} in Ar at 450 K (see the text).

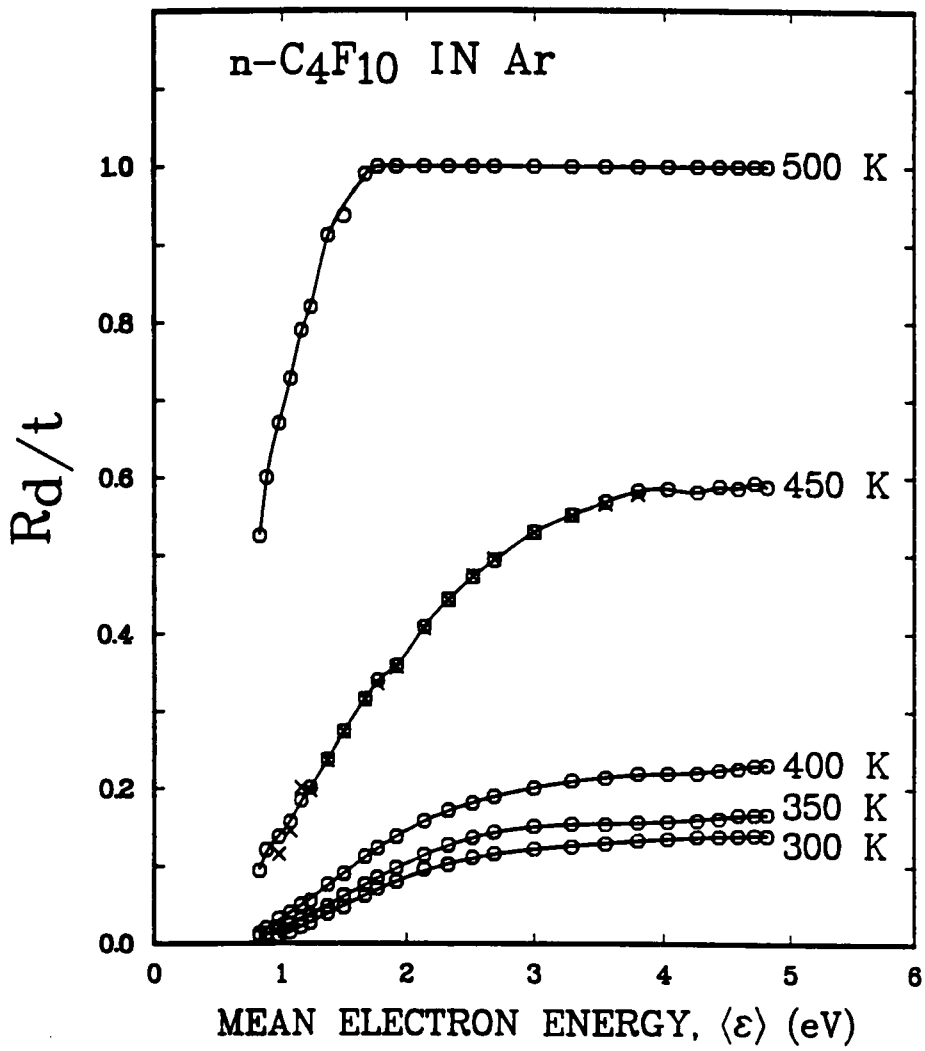

Figure 3.15: The ratio $R_{d/t}$ of the dissociative to the total electron attachment rate constant for n-C_4F_{10} as a function of the mean electron energy $\langle\epsilon\rangle$ at 300, 350, 400, 450, and 500 K. The data points ($\times$) for the 450 K are the values of $R_{d/t}(\langle\epsilon\rangle, T)$ calculated by a nonlinear least squares fit to Eqn 3.4.

3.4.2 Estimates of the Autodetachment Lifetime of $n-C_4F_{10}^{-*}$ in the Lowest (Bound) NIS

The observed linear dependence of $1/(k_a)_{nd}$ on $1/N_t$ allows an estimate of the autodetachment lifetime τ_a of $n-C_4F_{10}^{-*}$ produced via the lowest (bound) NIS as a function of $\langle\epsilon\rangle$ and T to be determined. From Eqn 3.5 and linear plots such as in Fig. 3.14 the $1/k_{1nd}$ and $\nu_{2nd}/k_{1nd}k_3$, were obtained at various values of $\langle\epsilon\rangle$ and T.

As discussed earlier by other authors (Goans and Christophorou, 1974; Hunter and Christophorou, 1984; Spyrou and Christophorou, 1985b) the ratio ν_{2nd}/k_3 gives the gas number density N_c at which the rate of autodetachment of $n-C_4F_{10}^{-*}$ is equal to the rate of stabilization of $n-C_4F_{10}^{-*}$ by collision with Ar atoms, *i.e.*,

$$\nu_{2nd}(=\tau_a^{-1}) = k_3 N_c \tag{3.8}$$

The average collision time τ_c between $n-C_4F_{10}$ and Ar atoms (since $N_{Ar} \gg N_a$) is given by

$$\tau_c = 1/\langle v\rangle \sigma_L N_c \tag{3.9}$$

where $\langle v\rangle$ is the average relative velocity between $n-C_4F_{10}$ and Ar, and σ_L is the classical Langevin collision cross section, which for orbiting collisions is given by (Langevin, 1905; Christophorou, 1971)

$$\sigma_L(v) = \frac{2\pi}{\langle v\rangle}\left(\frac{e^2\alpha}{M_r}\right)^{1/2} \tag{3.10}$$

where e is the electronic charge, α is the static polarizability of Ar ($= 1.64 \times 10^{-24} cm^3$) (Dalgarno, 1962), and M_r is the reduced mass of $n-C_4F_{10}$ and Ar. An estimate of k_3N_c can be obtained from

$$\tau_s\left(=(k_3N_c)^{-1}\right) = \frac{\tau_c}{p} = \frac{1}{2\pi p N_c}\left(\frac{M_r}{e^2\alpha}\right)^{1/2} = \frac{1.928\times10^9}{pN_c} \tag{3.11}$$

where τ_s is the average lifetime between stabilizing collisions, and $p \leq 1$ is the probability of stabilization of $n-C_4F_{10}^{-*}$ in each collision with an Ar atom. If p is assumed to be equal to one and independent of the captured electron's energy a lower limit to τ_s can be obtained.

Using Eqn 3.11 and the slopes and intercepts which were obtained from least squares fit to Eqn 3.5, the lowest limits for τ_a at 300, 400, and 450 K were estimated. These are plotted in Fig. 3.16 as a function of $\langle\epsilon\rangle$. While the meaning of these "lifetimes" is unclear [since at each value of $\langle\epsilon\rangle$ due to the broad $f(\epsilon, \langle\epsilon\rangle, T)$ one probes parent anions with a wide range of τ_a], they, nonetheless, demonstrate the increase in autodetachment probability with increasing $\langle\epsilon\rangle$ (and T). Since, however, the values of τ_a (see Fig. 3.16) at $\simeq 0.5eV$ are $< 10^{-8}s$ while electron beam experiments indicated τ_a values $> 10^{-5}s$ at this energy (Spyrou *et al.*, 1983), it seems that in the latter experiments most of the parent negative ions formed decay before they are detected and only a small fraction of them is detected, perhaps only those which are formed at lower (near zero) electron energies whose τ_a is longer. Consistent with this is the fact that in the swarm experiments at $\langle\epsilon\rangle \leq 1\ eV$ the parent ion intensity far exceeds that of the fragments, while the opposite is true in the electron beam studies.

3.4.3 Effect of Temperature on the Electron Attachment to the Perfluoroalkanes C_2F_6, C_3F_8, $n-C_4F_{10}$ and $n-C_6F_{14}$

The present measurements on $k_1(\langle\epsilon\rangle, T)$ for $n-C_4F_{10}$ and for $n-C_6F_{14}$ are compared in Fig. 3.17 with those for C_2F_6 (Spyrou and Christophorou, 1985a) and for C_3F_8 (Spyrou and Christophorou, 1985b) for four values of $\langle\epsilon\rangle$. The delicate dependencies of k_1 on both T and $\langle\epsilon\rangle$ depend on the size of the molecules, which apparently determines the relative contributions of the dissociative and nondissociative electron attachment processes. Thus, for C_2F_6 which attaches electrons by forming only fragment anions, the $\log(k_1)$ increases monotonically (actually linearly) with T (for this temperature range) at any $\langle\epsilon\rangle$. The next member of this family of molecules, the C_3F_8, which attaches electrons both dissociatively and nondissociatively, the $\log(k_1(\langle\epsilon\rangle, T))$ first decreases slowly with increasing T between 300 and 400 K and then decreases precipitously with increasing T down to

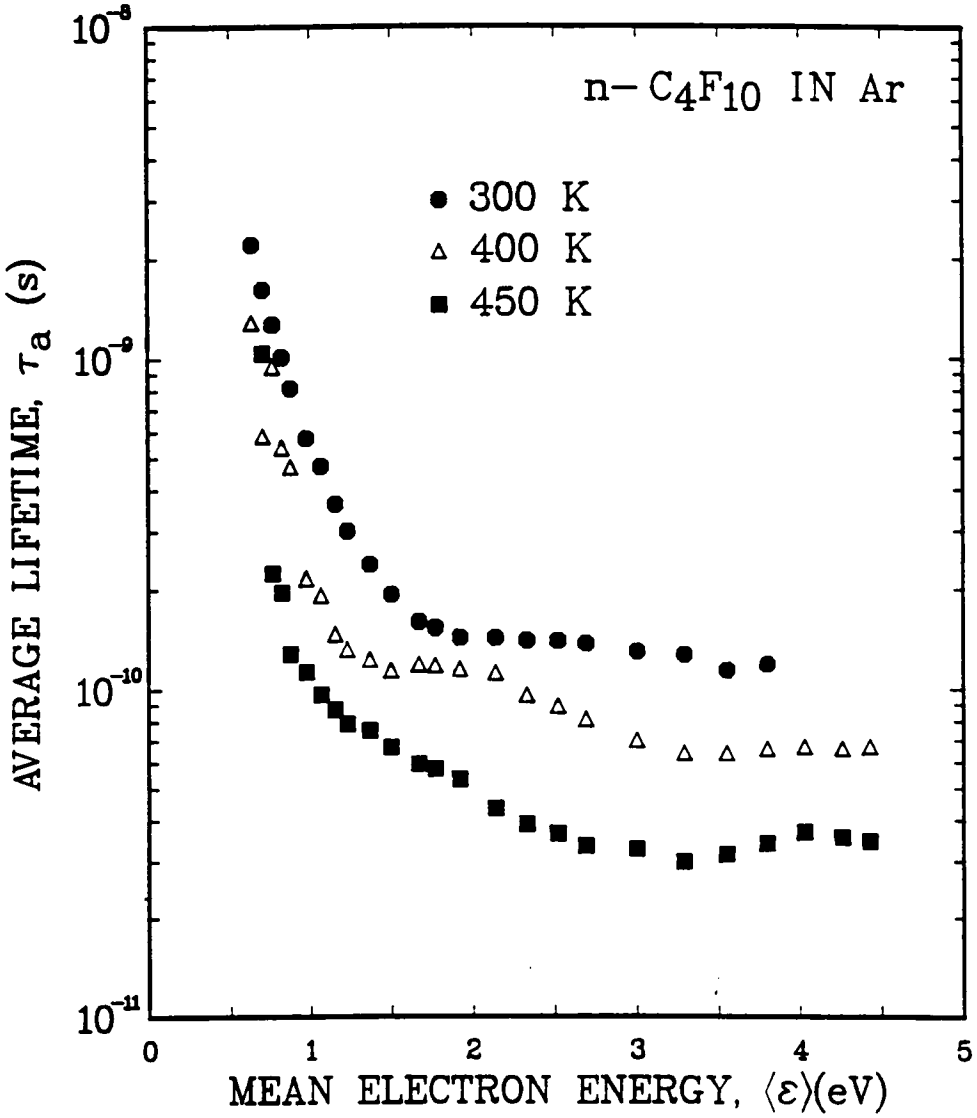

Figure 3.16: Lower limits to the average apparent autodetachment lifetime τ_a of n-$C_4F_{10}^{-*}$ in the lowest bound electronic negative ion state as a function of the mean electron energy $\langle\epsilon\rangle$ in Ar at 300, 400, and 450 K.

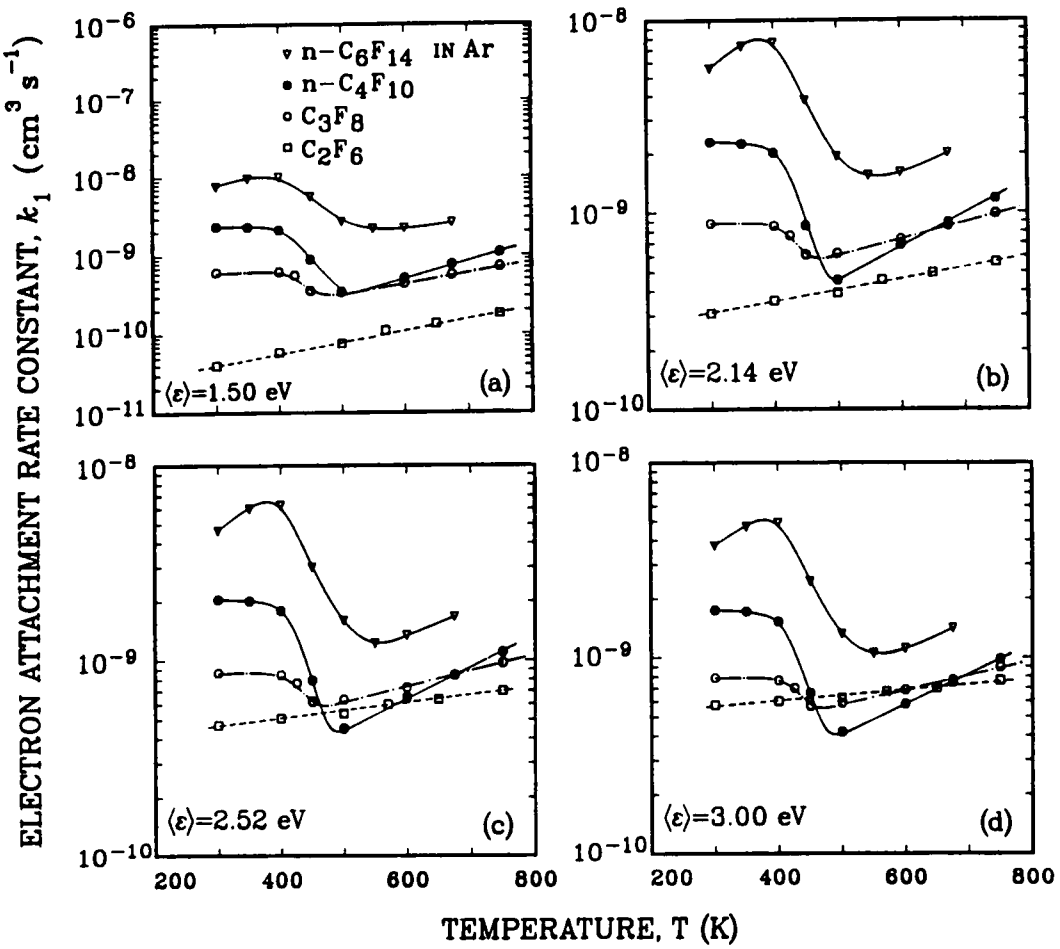

Figure 3.17: Comparison of the total electron attachment rate constants k_1 (for $N_a \longrightarrow 0$, $N_t \longrightarrow \infty$) for C_2F_6, C_3F_8, n-C_4F_{10}, and C_6F_{14} as a function of the temperature T at the mean electron energies $\langle\epsilon\rangle$: 1.50, 2.14, 2.52, and $300eV$.

a minimum value around $T \simeq 450\ K$ (due to the nondissociative electron attachment) and then increases linearly with T beyond $\simeq 500\ K$ (due to the dissociative character of the electron attachment process). This dependence varies with $\langle\epsilon\rangle$ and reflects the variation of $(k_a)_{nd}$ and $(k_a)_d$ with both $\langle\epsilon\rangle$ and T. For n-C_4F_{10} for which the nondissociative electron attachment is stronger a behavior similar to that just described for C_3F_8 is observed but is more pronounced (see Fig. 3.17). For n-C_6F_{14} the competition between the dissociative and the nondissociative processes lead first to an increase in k_a (due to the contribution of the dissociative electron attachment) between 300 and 400 K then to a decrease between 400 and 500 K (where the nondissociative process predominates) and subsequently to an increase for $T \geq 550\ K$ where the dissociative electron attachment predominates.

Chapter 4

Effect of Temperature on the Electron Attachment to SO_2F_2

4.1 Introduction

In this chapter the results of an electron swarm study on the temperature dependence of electron attachment to SO_2F_2 are presented and discussed. Also discussed, are the effects of T on the dissociative electron attachment to polyatomic molecules in terms of the increase with temperature T of their vibrational ($\simeq$ total internal) energy.

Low-energy electrons were found to attach to SO_2F_2 molecules both nondissociatively and dissociatively at room temperature (Reese *et al.*, 1958; Wang *et al.*, 1980; Sauers *et al.*, 1984). Electron beam studies (Reese *et al.*, 1958; Sauers *et al.*, 1984) have shown that a weak parent anion $SO_2F_2^{-*}$ is formed at very low electron energies with a maximum at $\simeq 0.0\ eV$ and an autodetachment lifetime τ_a at this energy of $\simeq 9\ \mu s$ (Sauers *et al.*, 1984). In addition three fragment negative ions — SO_2F^-, F^-, and F_2^- — have been observed (Sauers *et al.*, 1984): SO_2F^- with a main peak at $\simeq 2.95\ eV$ and a weak maximum at $\simeq 0.5\ eV$; F^- with a strong maximum at 3.3 eV and a weak peak at $\simeq 0.6\ eV$; and F_2^- with a peak at 3.3 eV. Based on these studies, therefore, the SO_2F_2 molecule has a bound low-lying [vertical attachment energy $\simeq 0.0\ eV$ (Christophorou, 1971)] negative ion state (NIS) leading to $SO_2F_2^-$ and repulsive NISs around 0.5 and 3.0 eV producing upon

decay, fragment (SO_2F^-, F^-, F_2^-) anions.

The study of effects of temperature on the electron attachment to SO_2F_2 at energies $\leq 1\ eV$ was motivated by reasons both practical and basic. SO_2F_2 can be found as a decomposition by-product when SF_6 gas, which is used as electrical insulation (*e.g.*, in high voltage or switching applications), decomposes because of sparks, corona, high electrical stress or high temperature. Also SO_2F_2 exhibits interesting electron attaching properties at room temperature (nondissociative electron attachment at $\simeq 0.0\ eV$, low-lying ($\simeq 0.5\ eV$) weak dissociative attachment). In this energy range the expected electron attachment processes are

$$e + SO_2F_2 \longrightarrow SO_2F_2^{-*} \longrightarrow SO_2F_2^- + \text{energy} \tag{4.1}$$

and

$$e + SO_2F_2 \longrightarrow SO_2F_2^{-*} \longrightarrow SO_2F^- + F \tag{4.2}$$

$$SO_2F + F^- \tag{4.3}$$

The present study shows that the electron attachment to SO_2F_2 is a function of both the temperature and electron energy and was independent of the total (buffer) gas number density. In particular, the electron attachment cross section $\sigma_a(\epsilon, T)$ was found to depend on the temperature as well on the electron energy ϵ.

4.2 Experimental Procedure

The experimental method and apparatus have been described earlier (see Chapter 2). N_2 was used as the carrier gas which was obtained from Matheson Gas Products with a quoted purity of 99.999%. The buffer gas was cooled to liquid nitrogen temperatures to freeze out condensible impurities. The SO_2F_2 sample used was obtained from the Linde Division of Union Carbide and had a stated minimum purity of 99.5 %. It was purified further by several vacuum distillation cycles. The total number density $N_t(\simeq N_{N_2})$ was varied from 2.25 to 6.44×10^{19} $molecules/cm^3$ and the attaching gas number density, N_a, was in the range 0.13

to 2.32×10^{14} $molecules/cm^3$. At each temperature studied the measurements were made over a range, E/N (density-reduced electric field) 0.062 to 7.75×10^{-17} Vcm^2. The values for the E/N employed and the corresponding mean electron energies $\langle\epsilon\rangle$ are given in Tables 4.1 to 4.5. At each value of E/N the mean electron energy $\langle\epsilon\rangle$ and the electron drift velocity $w(E/N)$ were obtained from the corresponding electron energy distribution function $f(\epsilon, E/N, T)$ in N_2, by solving the Boltzmann transport equation using the Luft code (Luft, 1975). At all temperatures below 700 K the measured $k_a(\langle\epsilon\rangle, T)$ did not depend on the time the measurement was made following the introduction of the gas mixture into the hot chamber. At 700 K, however, a small decrease in $k_a(\langle\epsilon\rangle, T)$ was noticed as the measurement was made at progressively longer and longer times t following the time t_0 at which the gas mixture was intoduced into the collision chamber. This may be attributed to the disapearence of SO_2F_2 through reactions with the walls of the hot chamber and/or through thermal decomposition of the molecule into nonelectron attaching species. Due to the small decrease of $k_a(\langle\epsilon\rangle, T)$ for SO_2F_2 at $T = 700$ K the following procedure was adopted: A premixture of SO_2F_2 with N_2 was prepared at room temperature and was introduced into the hot chamber ($T = 700$ K); a series of measurements on $k_a(\langle\epsilon\rangle, T)$ as a function of time was then conducted. From plots of $k_a(\langle\epsilon\rangle, T)$ versus time for each value of $\langle\epsilon\rangle$ (see Fig 4.1), the value of $k_a(\langle\epsilon\rangle, T)$ for that $\langle\epsilon\rangle$ was obtained for $t = t_0$ (*i.e.*, the time the admixture was introduced into the hot chamber). This procedure gave reliable reproducible data for $T = 700$ K. The $k_a(\langle\epsilon\rangle, T)$ rates given in Table 4.5 (for $T = 700$ K) are the values obtained from such measurments by extrapolation of the data to $t = t_o$.

Table 4.1: Total electron attachment rate constants, $k_a(\langle\epsilon\rangle, T)$, for SO_2F_2 in N_2 at $T = 300\ K$

E/N $(10^{-17} V cm^2)$	$\langle\epsilon\rangle$ (eV)	w $(10^5 cm/s)$	k_a $(10^{-10} cm^3/s)$
0.062	0.046	1.85	8.69
0.093	0.055	2.30	9.01
0.124	0.065	2.57	9.42
0.155	0.076	2.73	10.02
0.186	0.087	2.84	10.89
0.217	0.099	2.93	11.51
0.248	0.111	2.99	12.14
0.310	0.133	3.14	13.16
0.373	0.154	3.28	13.80
0.457	0.184	3.50	14.08
0.528	0.203	3.63	13.91
0.621	0.231	3.82	13.26
0.776	0.279	4.12	11.83
0.931	0.327	4.37	10.40
1.087	0.374	4.62	9.28
1.240	0.417	4.88	8.32
1.550	0.493	5.37	6.69
1.860	0.555	5.83	5.58
2.170	0.601	6.39	4.81
2.480	0.647	6.92	4.09
3.100	0.711	7.91	3.38
3.730	0.759	9.13	2.99
4.660	0.812	10.80	2.60
5.280	0.839	11.42	2.42
6.210	0.872	12.75	2.19
7.760	0.911	14.98	1.99

Table 4.2: Total electron attachment rate constants, $k_a(\langle\epsilon\rangle, T)$, for SO_2F_2 in N_2 at $T = 400\ K$

E/N $(10^{-17}Vcm^2)$	$\langle\epsilon\rangle$ (eV)	w $(10^5 cm/s)$	k_a $(10^{-10}cm^3/s)$
0.062	0.058	1.53	3.42
0.093	0.066	1.97	3.80
0.124	0.075	2.26	3.93
0.155	0.085	2.49	4.00
0.186	0.096	2.66	4.01
0.217	0.107	2.77	3.96
0.248	0.118	2.88	3.85
0.310	0.139	3.05	3.75
0.373	0.159	3.22	3.56
0.457	0.189	3.46	3.31
0.528	0.213	3.57	3.13
0.621	0.235	3.77	2.89
0.776	0.283	4.10	2.50
0.931	0.330	4.38	2.19
1.087	0.376	4.62	1.92
1.240	0.419	4.92	1.73
1.550	0.494	5.42	1.38
1.860	0.555	5.93	1.16
2.170	0.601	6.50	0.960
2.480	0.647	7.05	0.853
3.100	0.711	8.05	0.703
3.730	0.759	9.29	0.610
4.660	0.812	10.93	0.540
5.280	0.839	11.58	0.495
6.210	0.872	13.00	0.450
7.760	0.911	15.20	0.410

Table 4.3: Total electron attachment rate constants, $k_a(\langle\epsilon\rangle, T)$, for SO_2F_2 in N_2 at $T = 500\ K$

E/N $(10^{-17}Vcm^2)$	$\langle\epsilon\rangle$ (eV)	w $(10^5 cm/s)$	k_a $(10^{-10}cm^3/s)$
0.062	0.070	1.32	
0.093	0.076	1.77	
0.124	0.085	2.10	10.30
0.155	0.095	2.31	10.01
0.186	0.104	2.48	9.75
0.217	0.115	2.65	9.52
0.248	0.125	2.77	9.25
0.310	0.144	3.00	8.64
0.373	0.164	3.20	8.04
0.457	0.193	3.44	7.31
0.528	0.217	3.59	6.81
0.621	0.238	3.75	6.09
0.776	0.286	4.12	5.15
0.931	0.333	4.37	4.36
1.087	0.378	4.62	3.74
1.240	0.421	4.92	3.31
1.550	0.495	5.44	2.57
1.860	0.556	5.99	2.12
2.170	0.602	6.54	1.79
2.480	0.647	7.07	1.51
3.100	0.711	8.10	1.27
3.730	0.759	9.39	1.03
4.660	0.812	11.10	0.953
5.280	0.839	11.77	0.856
6.210	0.872	13.10	0.773
7.760	0.911	15.40	0.742

Table 4.4: Total electron attachment rate constants, $k_a(\langle\epsilon\rangle, T)$, for SO_2F_2 in N_2 at $T = 600\ K$

E/N $(10^{-17}Vcm)$	$\langle\epsilon\rangle$ (eV)	w $(10^5 cm/s)$	k_a $(10^{-10}cm^3/s)$
0.062	0.083	1.20	
0.093	0.086	1.60	
0.124	0.096	1.92	19.63
0.155	0.104	2.16	18.98
0.186	0.113	2.36	18.35
0.217	0.123	2.52	18.01
0.248	0.132	2.67	17.21
0.310	0.144	2.91	16.10
0.373	0.168	3.11	14.83
0.457	0.198	3.39	13.05
0.528	0.221	3.57	11.95
0.621	0.242	3.75	10.85
0.776	0.289	4.17	9.01
0.931	0.336	4.36	7.55
1.087	0.381	4.70	6.41
1.240	0.423	5.00	5.60
1.550	0.496	5.50	4.42
1.860	0.556	6.02	3.62
2.170	0.602	6.58	3.08
2.480	0.647	7.12	2.63
3.100	0.711	8.18	2.11
3.730	0.759	9.46	1.92
4.660	0.812	11.18	1.51
5.280	0.839	11.91	1.44
6.210	0.872	13.22	1.23
7.760	0.911	15.60	1.15

Table 4.5: Total electron attachment rate constants, $k_a(\langle\epsilon\rangle, T)$, for SO_2F_2 in N_2 at $T = 700\ K$

E/N $(10^{-17}Vcm)$	$\langle\epsilon\rangle$ (eV)	w $(10^5 cm/s)$	k_a $(10^{-10}cm^3/s)$
0.062	0.092	1.08	
0.093	0.097	1.49	
0.124	0.104	1.81	
0.155	0.112	2.06	27.00
0.186	0.121	2.27	25.98
0.217	0.130	2.41	25.21
0.248	0.139	2.61	24.32
0.310	0.157	2.88	22.73
0.373	0.176	3.12	21.18
0.457	0.202	3.41	19.22
0.528	0.221	3.58	17.79
0.621	0.249	3.81	15.56
0.776	0.296	4.20	13.41
0.931	0.343	4.44	11.16
1.087	0.388	4.70	9.68
1.240	0.429	5.00	8.19
1.550	0.503	5.57	6.38
1.860	0.556	6.12	5.22
2.170	0.602	6.70	4.41
2.480	0.647	7.28	3.66
3.100	0.711	8.40	2.83
3.730	0.759	9.66	2.52
4.660	0.812	11.31	2.25
5.280	0.839	12.05	2.02
6.210	0.872	13.40	1.86
7.760	0.911	15.70	

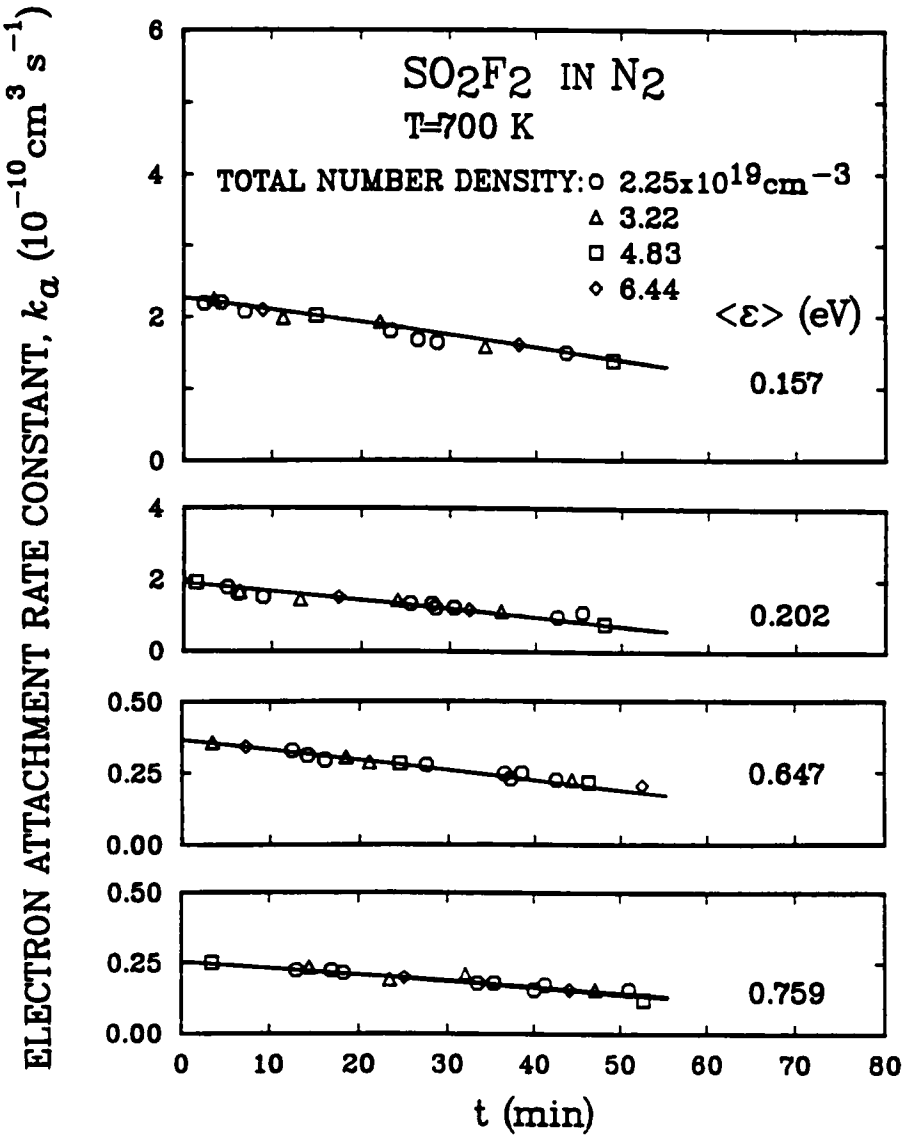

Figure 4.1: Plot of $k_a(\langle\epsilon\rangle, T)$ versus the time t following the time t_o at which the admixture (attaching-buffer gas) was introduced into the chamber, at $T = 700\ K$ for different values of $\langle\epsilon\rangle$ and for various total gas number densities.

4.3 Total Electron Attachment Rate Constant for SO_2F_2 Measured in N_2 as a Function of E/N, $\langle\epsilon\rangle$, and T

The total electron attachment rate constant, $k_a\,(E/N,T)$ for SO_2F_2 has been measured in the buffer gas N_2 as a function of E/N at the temperatures, T, of 300, 400, 500, 600, and 700 K. At each value of T and E/N (or $\langle\epsilon\rangle$) (see Tables 4.1 to 4.5), the $k_a\,(\langle\epsilon\rangle\,,T)$ was measured as a function of the ratio N_a/N_t of the attaching gas number density to the total gas number density. For all values of $\langle\epsilon\rangle$ and T the $k_a\,(\langle\epsilon\rangle\,,T)$ were found to be independent of the value of N_a/N_t when the latter was varied from 1.0 to 5.5 $\times$ 10^{-7} (Fig. 4.2). The measured values of $k_a(\langle\epsilon\rangle\,,T)$ as a function of E/N and $\langle\epsilon\rangle$ are listed in Tables 4.1 to 4.5 and the $k_a(\langle\epsilon\rangle\,,T)$ are plotted in Fig. 4.3. They are seen (Table 4.1, Fig. 4.3) to increase with T over the entire temperature range covered (300 to 700 K).

The increase in $k_a\,(\langle\epsilon\rangle\,,T)$ with increasing temperature is attributed to the increase with temperature of the contribution from the dissociative electron attachment processes. The maximum of $k_a\,(\langle\epsilon\rangle\,,T)$ (see Fig. 4.3) can be seen to shift to progressively lower values of mean electron energy as is to be expected for such dissociative electron attachment processes. (Fite *et al.*, 1963; O'Malley, 1967; Christophorou, 1980; Christophorou *et al.*, 1984; Spyrou and Christophorou, 1985a; Datskos and Christophorou, 1987).

In Table 4.6 are listed the measured thermal, $(k_a)_{thermal}$, and the maximum, $k_a\,(\langle\epsilon\rangle_{max})$, values of $k_a(\langle\epsilon\rangle\,,T)$ for various temperatures. The $(k_a)_{thermal}\,(T)$ values were determined at each temperature by extrapolating the measurements in Fig. 4.3 to $\langle\epsilon\rangle = (3/2)kT$. The $k_a\,(\langle\epsilon\rangle_{max})$ for 500, 600, and 700 K refer to the rate constant at the lowest $\langle\epsilon\rangle$ at which measurements were made.

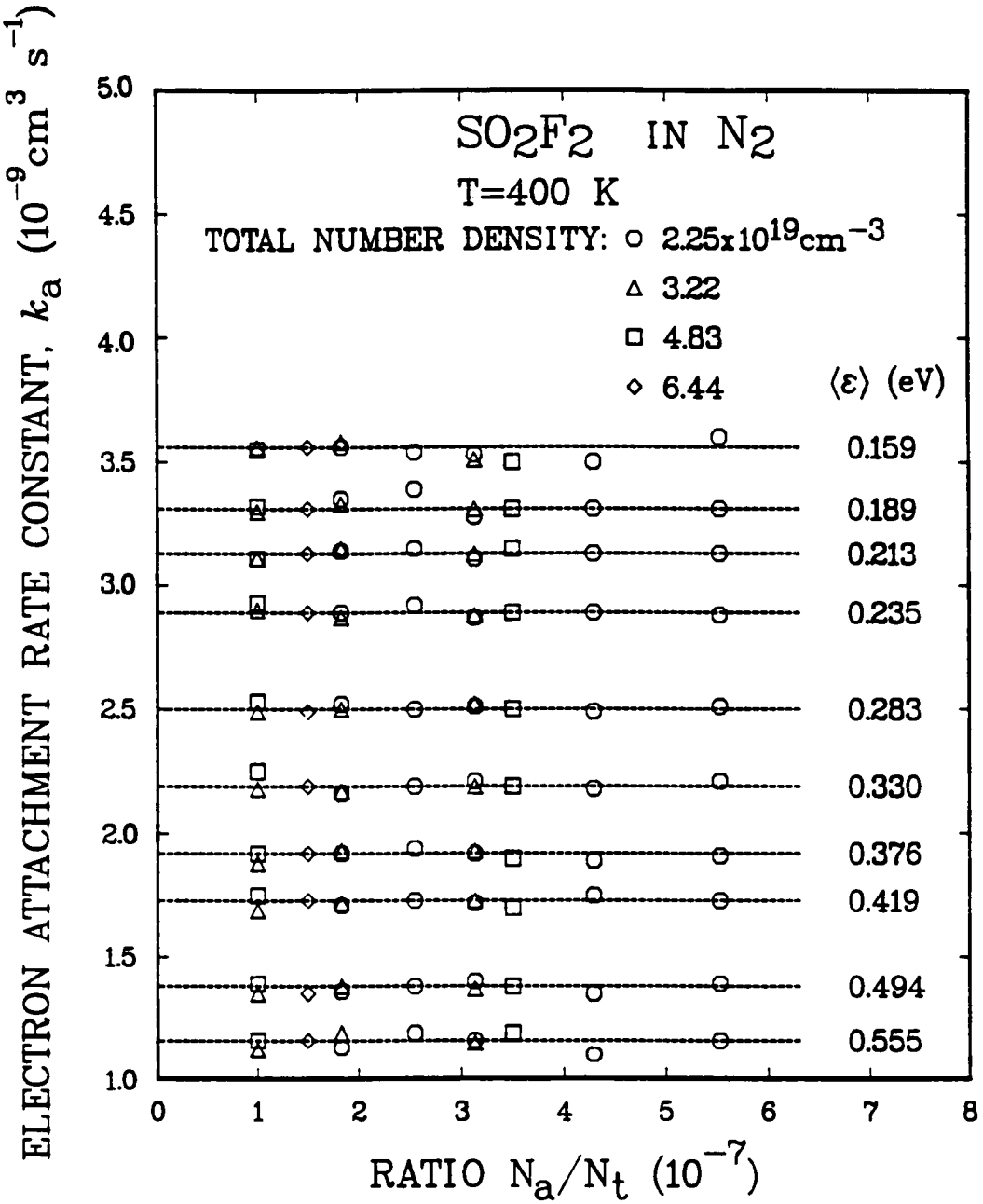

Figure 4.2: Total electron attachment rate constant $k_a(\langle\epsilon\rangle, T)$ for SO_2F_2 in N_2 as a function of the ratio N_a/N_t for $T = 400\ K$ and at the total gas number densities, N_t of 2.25×10^{19} (o), 3.22×10^{19} (Δ), 4.83×10^{19} (□), and 6.44×10^{19} (◇) $molecules/cm^{-3}$.

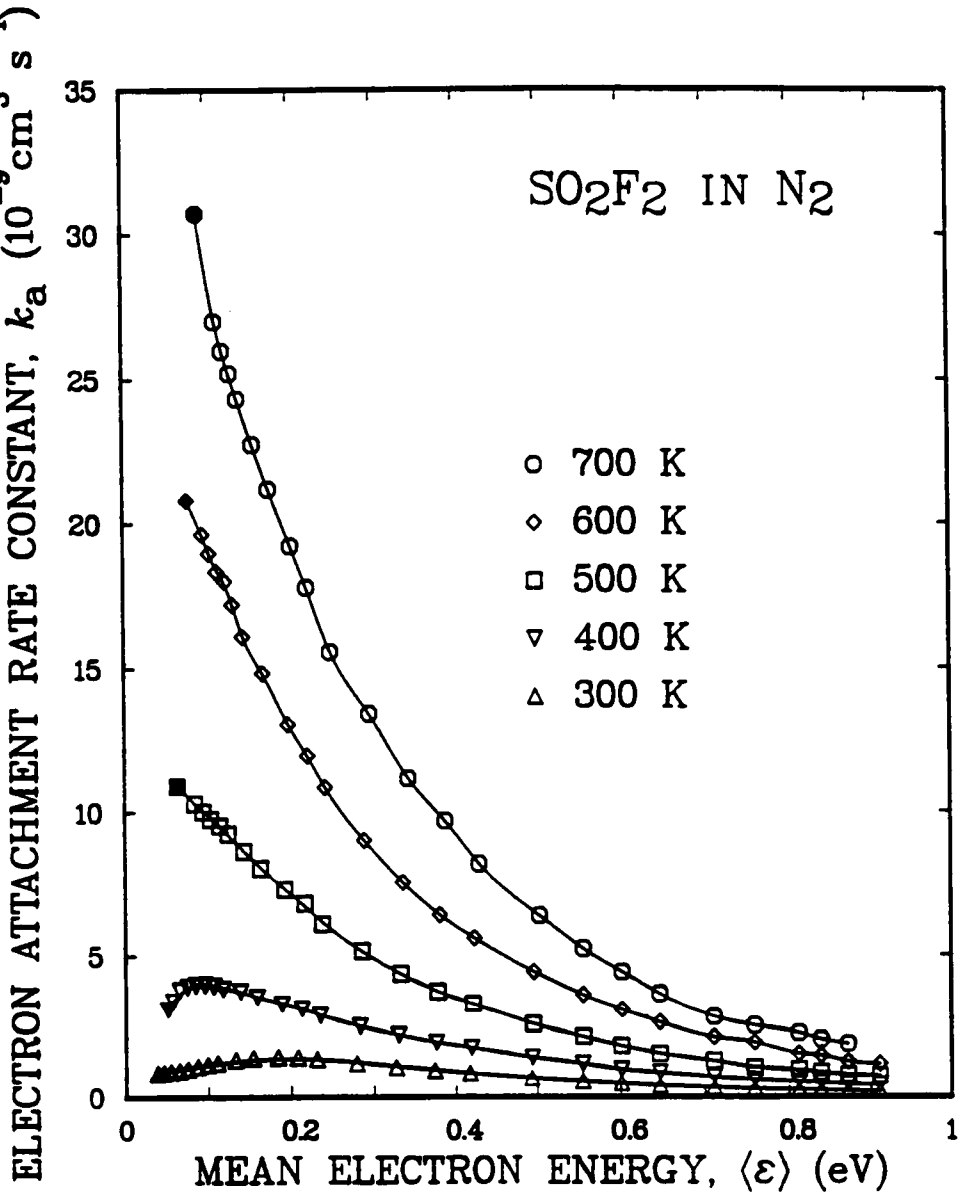

Figure 4.3: Total electron attachment rate constant $k_a(\langle\epsilon\rangle, T)$ as a function of the mean electron energy $\langle\epsilon\rangle$ for SO_2F_2 in N_2 at temperature T of 300 (△), 400(▽), 500(□), 600(◇), and 700(○) K. [The solid points are extrapolated data to $(3/2)kT$].

Table 4.6: Values of $k_a(T)_{thermal}$, $k_a(\langle\epsilon\rangle_{max}, T)$, ϵ_{max} and $\sigma_{da}(\epsilon_{max}, T)$ for SO_2F_2 in N_2 (see the text and the footnotes for explanation)

T	$(k_a)_{thermal}$	$k_a(\langle\epsilon\rangle_{max})$ [a]	ϵ_{max} [b]	$\sigma_{da}(\epsilon_{max})$
(K)	$(10^{-9}cm^3/s)$	$(10^{-9}cm^3/s)$	(eV)	$(10^{-16}cm^2)$
0			0.330	
300	0.84	1.41	0.220	1.06
400	3.11	4.01	0.130	2.27
500	10.90	10.30	0.090	8.71
600	20.80	19.63	0.070	17.10
700	30.70	27.00	0.025	33.70

[a] Value of the measured electron attachment rate constant at $\langle\epsilon\rangle_{max}(T)$

[b] Energy at which the swarm-unfolded electron attachment cross section at a given value of T is maximized

4.4 Swarm-Unfolded Total Electron Attachment Cross Sections

The $k_a(\langle\epsilon\rangle, T)$ data in Fig. 4.3 were unfolded employing the swarm unfolding technique (Christophorou *et al.*, 1971) and the Luft code (Luft, 1975) for solving the Boltzmann transport equation to obtain the electron energy distribution function $f(\epsilon, \langle\epsilon\rangle, T)$ used in the unfolding procedure. The deduced total electron attachment cross sections $\sigma_a(\epsilon, T)$ are shown in Fig. 4.4. At 300 K, the $\sigma_a(\epsilon, T)$ exhibits an increase below $\simeq 0.1$ eV and a maximum at $\simeq 0.22$ eV. The former is attributed to the contribution of the nondissociative electron attachment (process 4.1) and the latter to the contribution of the dissociative electron attachment (processes 4.2 and 4.3). The small contribution to $\sigma_a(\epsilon, T)$ from the parent negative ion which is evident in the $T = 300$ K data [and is shown by the low-pressure, room temperature electron beam measurements (Sauers, *et al.*, 1984)] vanishes at higher temperatures where dissociative electron attachment processes dominate; at $T \geq 400$ K, the increase in $\sigma_a(\epsilon, T)$ below $\simeq 0.1$ eV (as $\epsilon \rightarrow 0.0$ eV) disappears and $\sigma_a(\epsilon, T)$ shows only a main maximum. This maximum shifts towards lower electron energies ϵ with increasing T, reflecting the preponderance of the fragment negative ions and the depletion of the parent anions. The energy values ϵ_{max} at which the total dissociative electron attachment cross section $\sigma_{da}(\epsilon, T)$ peaks and the magnitude $\sigma_{da}(\epsilon_{max})$ of $\sigma_{da}(\epsilon, T)$ at ϵ_{max} are listed for a number of temperatures in Table 4.6 and are plotted in Fig. 4.5 as a function of the temperature. Assuming a linear relationship between ϵ_{max} and T, a straight line was then fitted through the data points enabling the prediction of the energy $\epsilon_{max}(= 0.33$ $eV)$, at which the dissociative electron attachment cross section $\sigma_a(\epsilon, T)$ peaks when $T \rightarrow 0$ K as well as the temperature ($T = 737$ K) at which $\epsilon_{max} = 0.0$ eV.

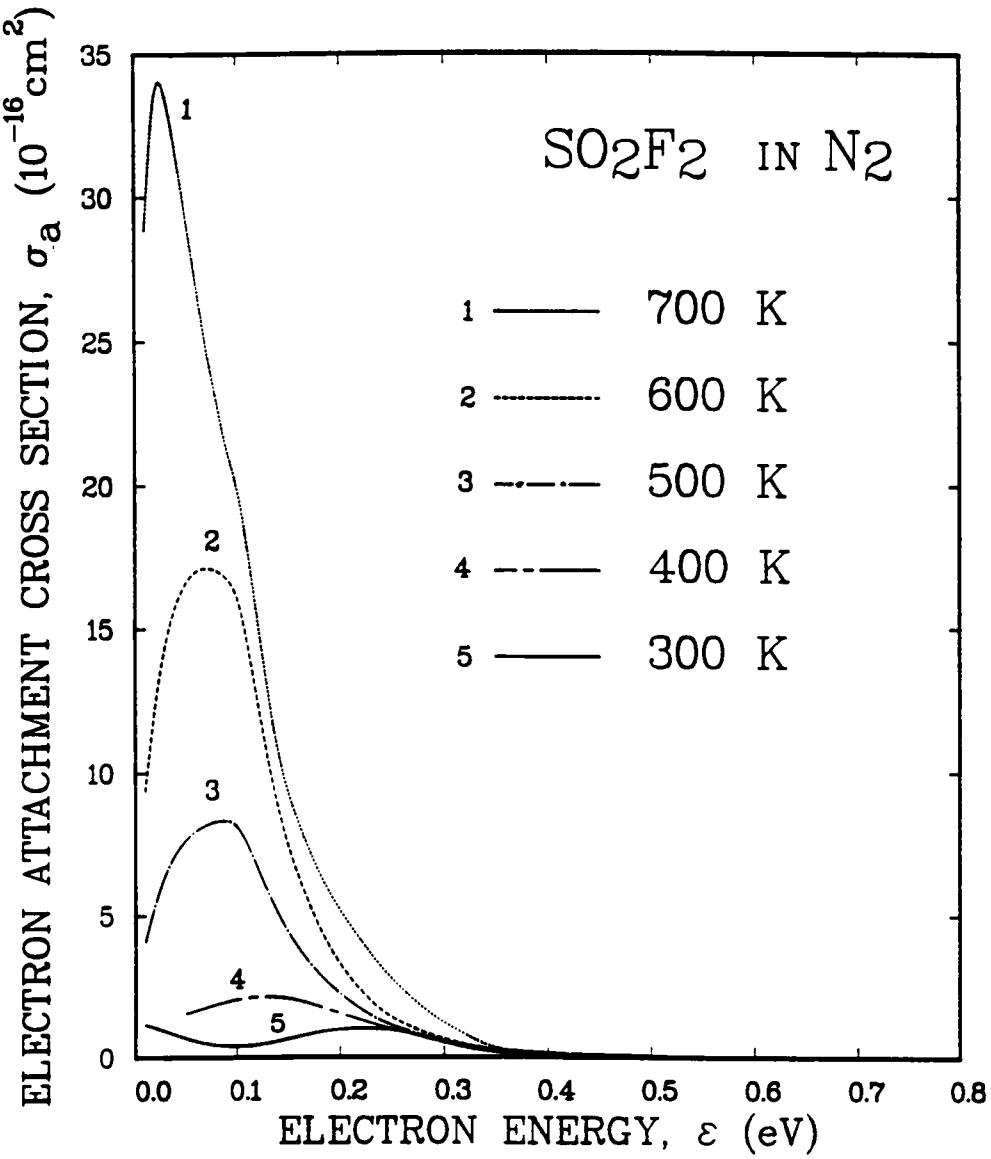

Figure 4.4: The swarm unfolded total electron attachment cross section $\sigma_a(\epsilon, T)$ for SO_2F_2 in N_2 as a function of the electron energy ϵ and at temperatures T of 300, 400, 500, 600, and 700 K.

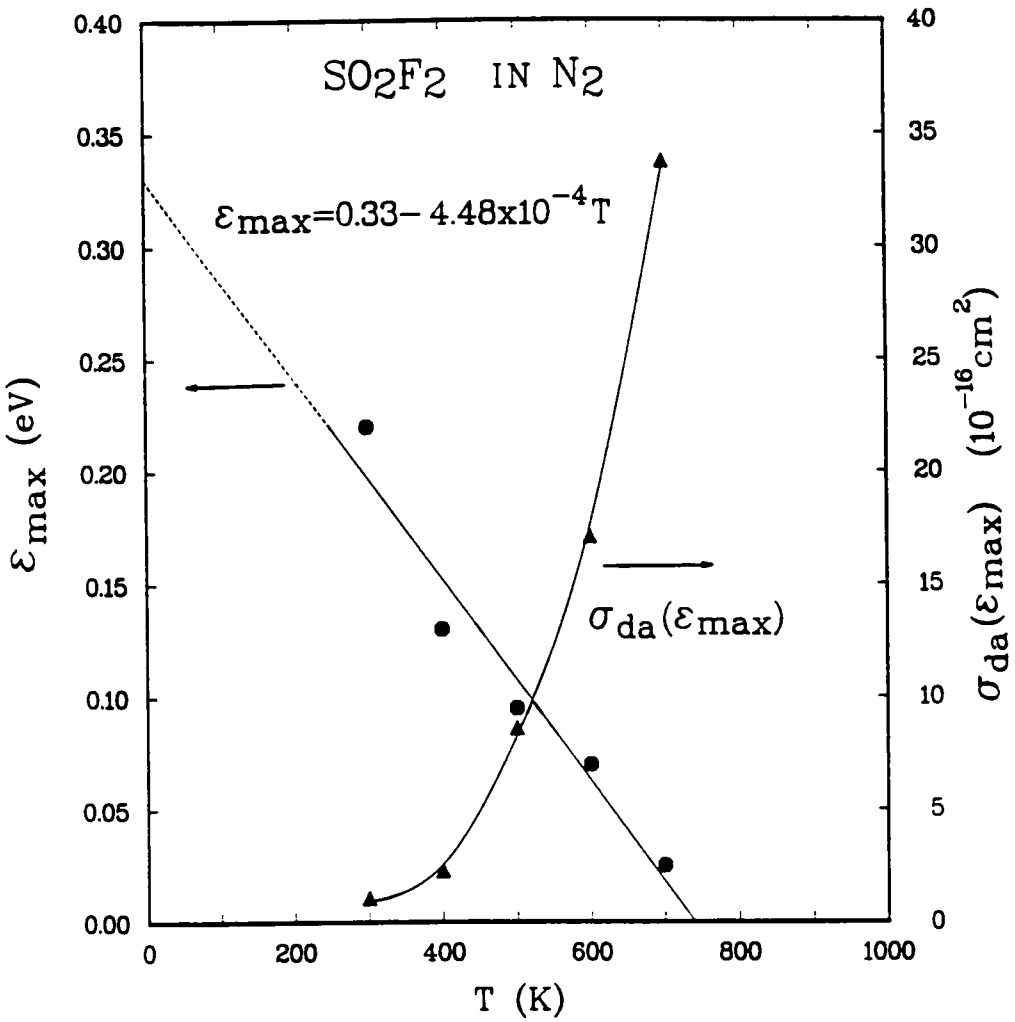

Figure 4.5: Variation with temperature of the peak energy ϵ_{max}, and the peak value $\sigma_{da}(\epsilon_{max})$, of the total electron attachment cross section for SO_2F_2.

4.5 Discussion

4.5.1 Effect of Temperature on the Low-Energy Electron Attachment Processes in SO_2F_2

From the results presented in sections 4.3 and 4.4, it is seen that as the temperature T is increased, $k_a(\langle\epsilon\rangle, T)$ increases and this increase is progressively larger at the lower mean electron energies $\langle\epsilon\rangle$ (see Fig. 4.3). Similarly, as T increases, $\sigma_a(\epsilon, T)$ increases and the electron energy position, ϵ_{max}, of the resonance maximum decreases (see Fig. 4.5). This behavior is analogous to that observed earlier for negative ions produced via dissociative electon attachment processes in diatomic and polyatomic molecules (*e.g.*, Fite and Brackmann, 1963; O'Malley, 1967; Christophorou, 1980; Christophorou *et al.*, 1984; Spyrou and Christophorou, 1985a, 1985b; Datskos and Christophorou, 1987). As indicated in Chapter 1, the resonance dissociative electron attachment process for a molecule may be visualized to proceed through a negative ion intermediate which dissociates and the cross section $\sigma_{da}(\epsilon, T)$ may be written as (see Chapter 1)

$$\sigma_{da}(\epsilon, T) = \sigma_c(\epsilon, T)\, e^{-\tau_s/\tau_a} \tag{4.4}$$

where $\sigma_c(\epsilon, T)$ is the cross section for the capture of the electron by the molecule, τ_s is the average separation time of the dissociation products and τ_a is the transient anion's average autodetachment lifetime. For diatomic molecules, the effect of increasing T on $\sigma_{da}(\epsilon, T)$ has been attributed to the population of higher vibrational levels of the neutral molecule, and the high sensitivity of $\sigma_{da}(\epsilon, T)$ to the range of nuclear motion; as higher vibrational levels are populated, the Franck-Condon region is broadened, the ϵ_{max} is lowered and the magnitude of $\sigma_{da}(\epsilon, T)$ is increased [principally because the survival factor $e^{-\tau_s/\tau_a}$ (Christophorou, 1971) for the transient anion is increased]. The large effect of T observed in this study for SO_2F_2 is similarly attributed to an increase in the survival factor with increasing T mainly because τ_s decreases as T increases. (Although the population N_v of the higher-lying vibrational levels is much smaller than the population $N_{v=0}$ of the ground

state the cross section, σ_{da}^{v}, for dissociative electron attachment at temperatures above ambient can be much larger so that $N_v\,\sigma_{da}^{v} \geq N_{v=0}\,\sigma_{da}^{v=0}$). The finding that for this molecule the cross section for the $\simeq 0.22\ eV$ dissociative electron attachment process under consideration in this study is much smaller than at $\simeq 3\ eV$ (Sauers *et al.*, 1984) indicates that the survival probability for the former is very small because τ_s is large due to the small amount of translational energy available to the separating fragments. A small change in T, then, can effect a large change in the survival probability.

In Fig. 4.6 the logarithm of $k_a(\langle\epsilon\rangle, T)$ is plotted as a function of $1/T$ for a number of values of $\langle\epsilon\rangle$. The $k_a(\langle\epsilon\rangle, T)$ data for the temperature range investigated follow closely (see Fig. 4.6) the relationship

$$k_a\left(\langle\epsilon\rangle, T\right) = C\left(\langle\epsilon\rangle\right) e^{-D(\langle\epsilon\rangle)/kT} \tag{4.5}$$

where k is the Boltzmann constant and $C\left(\langle\epsilon\rangle\right)$ is a constant at each value of $\langle\epsilon\rangle$. Then from plots of $\ln k_a$ versus $1/T$ the $D(\langle\epsilon\rangle)$ can be obtained from a linear least-squares fit. The quantity $D(\langle\epsilon\rangle)$ is plotted in Fig. 4.7 as a function of $\langle\epsilon\rangle$ and may be viewed [as did O'Malley (1967) in the case of O^- from O_2] as an average internal energy of the molecule which maximizes the effective dissociative attachment cross section which may be expressed as

$$\sigma_{da}\left(\epsilon, T\right) = \sum_{i=1}^{N}\sum_{v=0}^{\infty} B_v^i \sigma_{da}^{v,i}(\epsilon, T) \tag{4.6}$$

In Eqn 4.6 the $\sigma_{da}^{v,i}\left(\epsilon, T\right)$ are the cross sections for dissociative electron attachment from vibrational levels v of the vibrational mode i, N is the number of vibrational degrees of freedom, and $B_{v,i}$ are the corresponding Boltzmann factors which are given by

$$B_v^i = \frac{\mathrm{e}^{-\epsilon_v/kT}}{\sum_{v=0}^{\infty}\mathrm{e}^{-\epsilon_v/kT}} \tag{4.7}$$

Such an interpetation of $D\left\langle\epsilon\right\rangle$ would be consistent with the fact that $D\left\langle\epsilon\right\rangle$ is a function of $\langle\epsilon\rangle$ (Figs. 4.6 and 4.7).

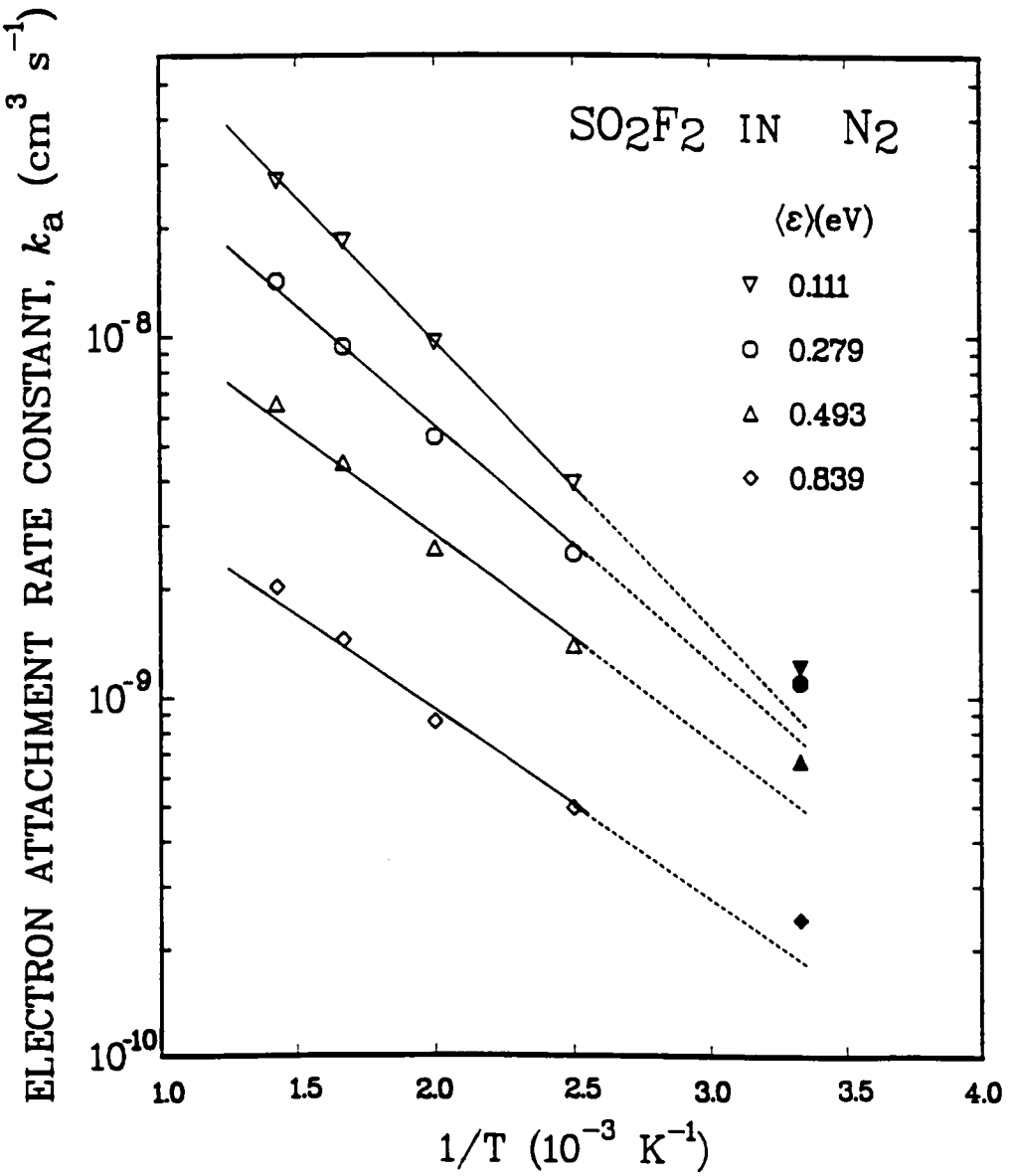

Figure 4.6: Total electron attachment rate constant $k_a(\langle\epsilon\rangle, T)$ as a function of $1/T$ for a number of mean electron energies.

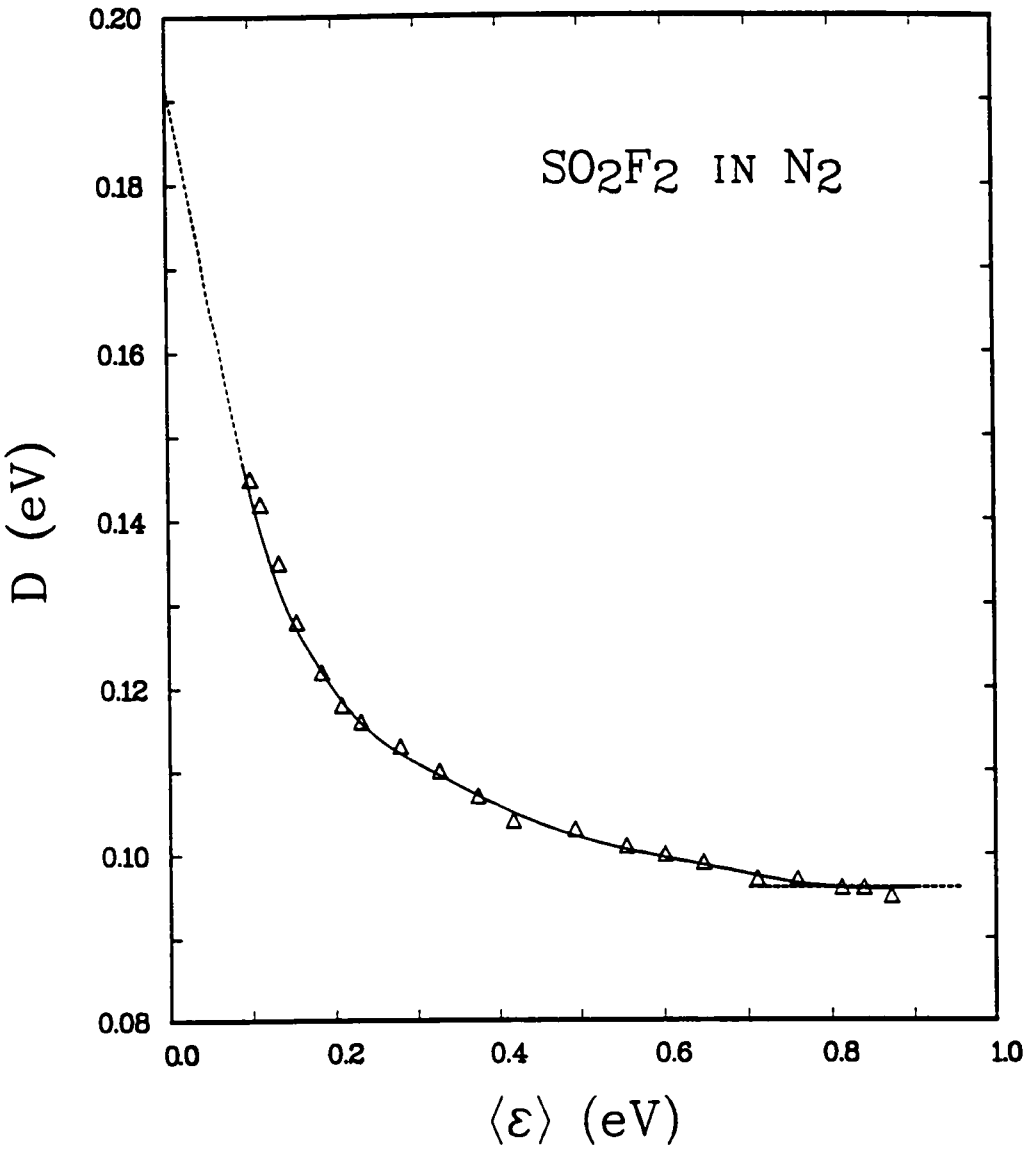

Figure 4.7: Variation of D with mean electron energy $\langle\epsilon\rangle$ for dissociative electron attachment to SO_2F_2 (see text).

4.5.2 Effect of Internal Energy of SO_2F_2 on $\sigma_{da}(\epsilon)$

This and earlier studies (Fite and Brackmann, 1963; O'Malley, 1967; Bardsley and Wadehra, 1979; Christophorou, 1980; Christophorou *et al.*, 1984; Spyrou and Christophorou, 1985a,b; Datskos and Christophorou, 1987; Christophorou *et al.*, 1987) demonstrate that the effect of T on $k_{da}(\langle\epsilon\rangle, T)$ and $\sigma_{da}(\epsilon, T)$ can be understood in terms of the increase of the total internal energy of the molecule with increasing T. In Fig. 4.8 the magnitude of the cross section $\sigma_{da}(\epsilon, T)$ at ϵ_{max} is plotted as a function of the total vibrational energy, $\langle\epsilon\rangle_{vibr}(T) - \langle\epsilon\rangle_z$, of the SO_2F_2 molecule in excess of its zero-point energy $\langle\epsilon\rangle_z$. The quantity $\langle\epsilon\rangle_{vibr}(T)$ was calculated from

$$\langle\epsilon\rangle_{vibr}(T) = \sum_{i=1}^{N}\sum_{v=0}^{\infty} B_{v,i}(v + 1/2)h\nu_i \tag{4.8}$$

where N is the number of vibrational degrees of freedom, ν_i is the vibrational frequency of the ith mode, and

$$B_{v,i} = \frac{e^{-(v+1/2)h\nu_i/kT}}{\sum_{v=0}^{\infty} e^{-(v+1/2)h\nu_i/kT}} \tag{4.9}$$

are the Boltzmann factors for each normal mode ν_i at a particular T. Using expressions 4.8 and 4.9 and the vibrational frequencies for SO_2F_2 reported by Shimanouchi (1972) the quantity $\langle\epsilon\rangle_{vibr}(T) - \langle\epsilon\rangle_z$ was determined (Table 4.7). If the small contribution of rotational excitation is neglected, the total internal energy of the molecule as a function of T is

$$\langle\epsilon\rangle_{int}(T) \simeq \langle\epsilon\rangle_{vibr}(T) - \langle\epsilon\rangle_z \tag{4.10}$$

In Fig. 4.8 besides $\sigma_{da}(\epsilon_{max})$ versus $\langle\epsilon\rangle_{int}$, the maximum thermal $s-wave$ electron capture cross section $(\sigma_a)_{s-wave}$ is also plotted as a function of $\langle\epsilon\rangle_{int}$. This quantity

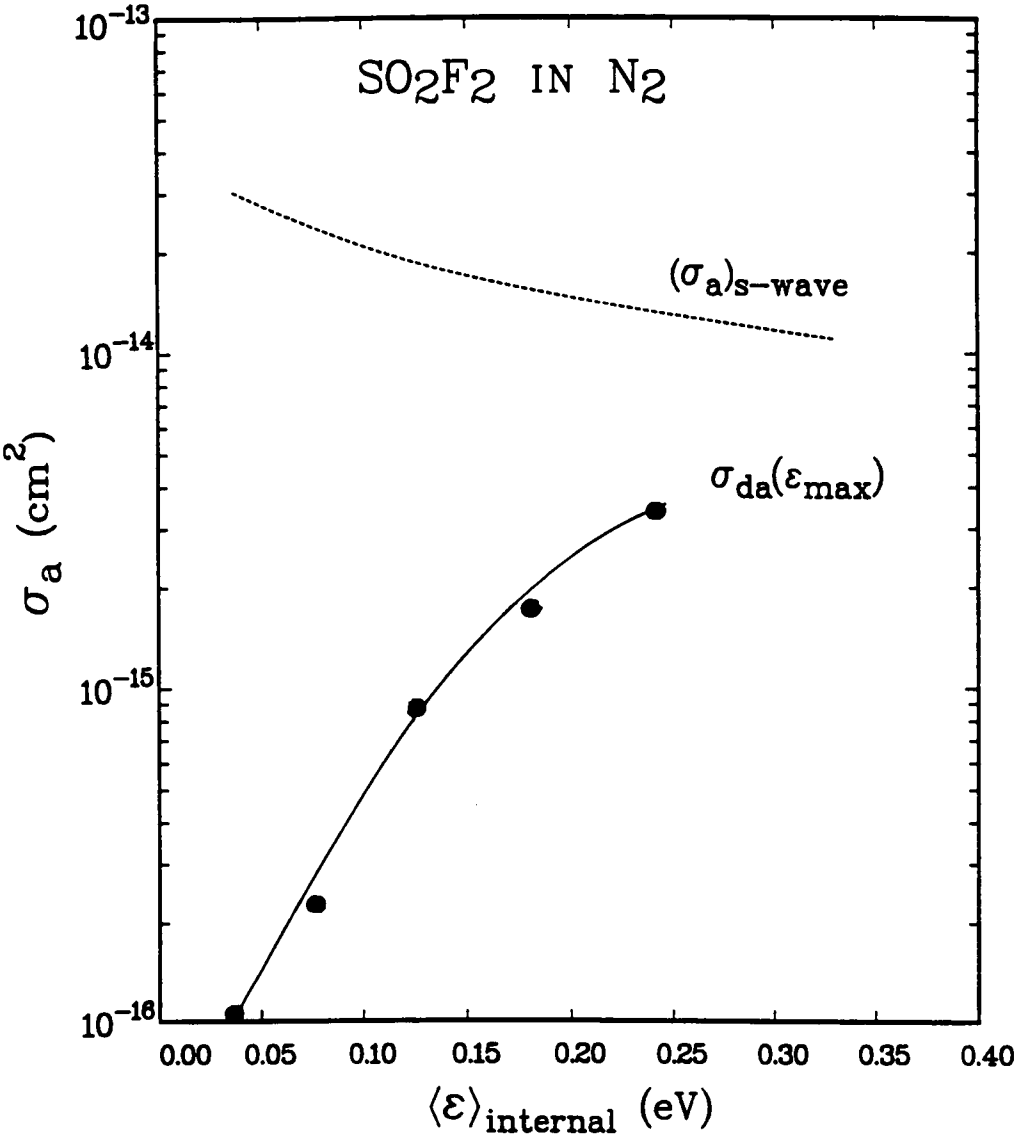

Figure 4.8: Variation of the peak value $\sigma_{da}(\epsilon_{max})$ of the dissociative electron attachment cross section for SO_2F_2 with internal energy $\langle\epsilon\rangle_{internal}$. The $(\sigma_a)_{s-wave}$ is the maximum $s-wave$ electron capture cross section determined at each T as discussed in the text.

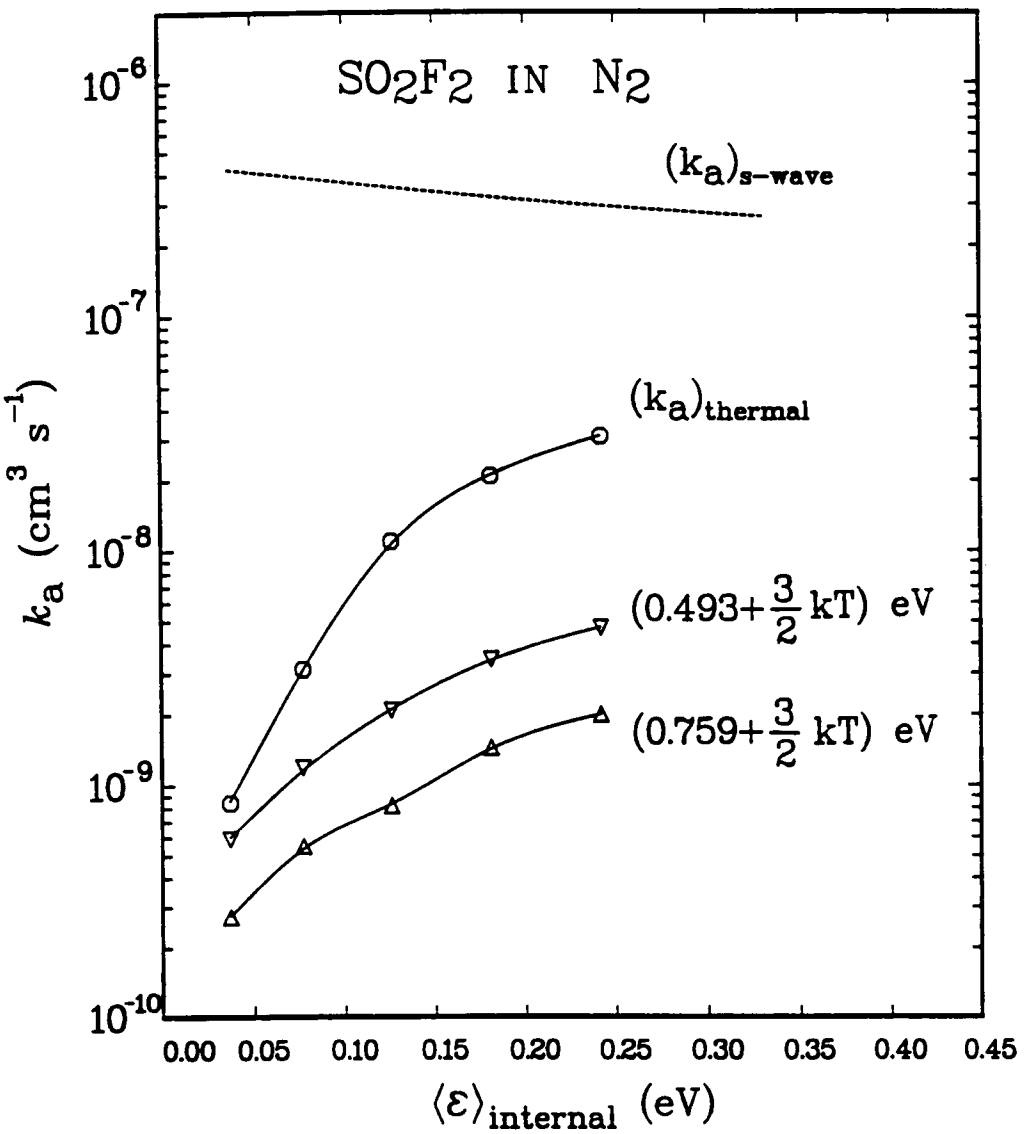

Figure 4.9: Plot of the electron attachment rate constant k_a for SO_2F_2 as a function of internal energy $\langle\epsilon\rangle_{internal}$ for the mean electron energies $\langle\epsilon\rangle = (3/2)kT$, $0.493 + (3/2)kT$, and $0.759 + (3/2)kT$ eV ($T = 300$, 400, 500, 600, and 700 K). $(k_a)_{s-wave}$ is the maximum $s-wave$ electron capture rate constant (see text).

Table 4.7: Values of $(\langle\epsilon\rangle_{int}$, $(\sigma_a)_{s-wave}(\frac{3}{2}kT)$, and $(k_a)_{s-wave}(T)$ for SO_2F_2 in N_2 (see the text and the footnotes for explanation)

T	$\langle\epsilon\rangle_{int}$[a]	$\frac{3}{2}kT$	$(\sigma_a)_{s-wave}(\frac{3}{2}kT)$[b]	$(k_a)_{s-wave}(T)$[c]	$(k_a)_{s-wave}(T)$[d]
(K)	(eV)	(eV)	$(10^{-14}cm^2)$	$(10^{-7}cm^3/s)$	$(10^{-7}cm^3/s)$
300	0.037	0.039	3.087	4.33	4.98
400	0.077	0.052	2.315	3.86	4.32
500	0.126	0.065	1.852	3.47	3.86
600	0.181	0.078	1.544	3.13	3.52
700	0.242	0.091	1.323	2.93	3.26
837[e]	0.330	0.108	1.100	2.67	2.98

[a]Internal energy of the molecule assumed to be equal to $\langle\epsilon\rangle_{vibr} - \langle\epsilon\rangle_z$ (see text)

[b]Maximum $s-$wave electron attachment cross section determined at each value of T from Eqn 4.11

[c]Maximum electron attachment rate constant as a function of T obtained using Eqn 4.12 and $f(\epsilon, \frac{3}{2}kT, T)$ for N_2

[d]Maximum electron attachment rate constant as a function of T obtained using Eqn 4.12 and a Maxwellian electron energy distribution function

[e]Temperature at which the internal energy of the molecule equals the vertical attachment energy for $T = 0\ K$

was determined from[a] (Mott and Massey, 1965; Christodoulides *et al.*, 1979)

$$(\sigma_a)_{s-wave} = \left(\frac{\pi\hbar^2}{2m}\right)\frac{1}{\epsilon} = \frac{1.197 \times 10^{-15}}{\epsilon\ (eV)}\ (cm^2) \tag{4.11}$$

where the electron energy ϵ was replaced by the mean thermal electron energy $\langle\epsilon\rangle_{thermal}\,[=(3/2)kT]$ for values for which $\langle\epsilon\rangle_{int}$ was determined and experimental data were taken. As T increases the $\langle\epsilon\rangle_{int}$ increases which results in a decrease in $(\sigma_a)_{s-wave}$. For each value of T corresponds a specific value of $(\sigma_a)_{s-wave}$ and $\langle\epsilon\rangle_{int}$ and hence $(\sigma_a)_{s-wave}$ can be plotted along with the experimental data as a function of $\langle\epsilon\rangle_{int}$. This plot shows how $\sigma_{da}\,(\epsilon_{max})$ approaches $(\sigma_a)_{s-wave}$ as the internal energy $\langle\epsilon\rangle_{int}$ of the molecule increases. Thus, as $\langle\epsilon\rangle_{int}$ approaches $(\epsilon_{max})_{T=0K} \simeq 0.33\ eV$, the $\sigma_{da}(\epsilon_{max})$ tends to level off toward the maximum $s-wave$ capture cross section value for $T \simeq 837\ K$, the temperature at which $(\epsilon_{max})_{T=0K} \simeq \langle\epsilon\rangle_{int}$. These findings indicate that the dissociative electron attachment process becomes exoergic at these temperatures because the internal energy of the negative ion exceeds the energy which is required for dissociative electron attachment to occur. In a similar manner, from plots of $k_a(\langle\epsilon\rangle, T)$ versus $\langle\epsilon\rangle_{int}$ (see Fig. 4.9) one can observe that the electron attachment rate constant does depend on the total internal energy of the molecule. As this internal energy is increased (by increasing the temperature), the dissociative electron attachment process becomes exoergic and $k_a(\langle\epsilon\rangle, T)$ tends towards saturation. Also shown in Fig. 4.9 for comparison is the maximum $s-wave$ electron capture rate constant determined as function of $\langle\epsilon\rangle\,[=(3/2)kT]$ from

$$\begin{aligned}(k_a)_{s-wave}(\langle\epsilon\rangle, T) &= \left(\frac{2}{m}\right)^{1/2}\left(\frac{\pi\hbar^2}{2m}\right)\int_0^\infty \epsilon^{-1/2} f(\epsilon, \langle\epsilon\rangle, T)d\epsilon \\ &= 7.1 \times 10^{-8}\int_0^\infty \epsilon^{-1/2} f(\epsilon, \langle\epsilon\rangle, T)d\epsilon \end{aligned} \tag{4.12}$$

using the electron energy distribution functions $f(\epsilon, \langle\epsilon\rangle, T)$ in N_2 for a number of

[a]Of course, one can determine an average of $(\sigma_a)_{swave} = (\pi\hbar^2)/(2m\epsilon)$ over a Maxwell-Boltzmann electron energy distribution function for the values of T at which the measurements were made. Such average values of the maximum thermal $s-wave$ electron capture cross section differ from the ones plotted in Fig. 4.8 by a factor of 3 and have the same functional dependence on $\langle\epsilon\rangle_{int}$.

$\langle\epsilon\rangle = (3/2)kT$. These values are shown in Table 4.7. Also in Table 4.7 are shown the values of $\langle\epsilon\rangle = (3/2)kT$ when a Maxwellian distribution function, $f_{MB}(\epsilon, T)$, is used. It can be seen that the values for $(k_a)_{s-wave}(T)$ obtained using the $f(\epsilon, \langle\epsilon\rangle, T)$ for N_2 and a Maxwellian electron energy distribution differ very little since

$$\lim_{\langle\epsilon\rangle \to \frac{3}{2}kT} f(\epsilon, \langle\epsilon\rangle, T) = f_{MB}(\epsilon, T) \tag{4.13}$$

The dependence of $\sigma_{da}(\epsilon, T)$ on the $\langle\epsilon\rangle_{int}$ observed in the present study for SO_2F_2 and similar earlier studies on other polyatomic [C_2F_6 (Spyrou and Christophorou, 1985a), C_3F_8 (Spyrou and Christophorou, 1985a) and n-C_4F_{10} (Datskos and Christophorou, 1987)] and diatomic molecules [O_2 (Fite and Brackmann, 1963; O'Malley, 1967), H_2 (Wadhera, 1984; Bardsley and Wadhera, 1979)] clearly exhibits the critical role that the molecule's internal (mostly vibrational) energy plays in dependence of the magnitude of $\sigma_{da}(\epsilon, T)$ on the temperature.

Chapter 5

Effect of Density and Temperature on the Ionization Threshold of TMPD in Ethane

5.1 Introduction

In this chapter the results of a multiphoton ionization conductivity study of the density and temperature dependence of the ionization threshold of TMPD (N,N,N′,N′-tetramethyl-p-phenylenediamene) molecules in ethane (C_2H_6) are presented and discussed.

The ionization threshold, I_f, of a molecule embedded in a medium, strongly depends on the effect that its environment has on charge-seperated states (electron-ion pairs, free and quasi-free electrons, Rydberg states, positive and negative ions) and as such it is of basic interest. The ionization threshold, I_f, of a molecule which finds itself in a liquid phase or dense fluid environment may be expressed as (see Chapter 1)

$$I_f = I_g + P^+ + V_o \tag{5.1}$$

where I_g is the gas-phase adiabatic ionization threshold, P^+ is the polarization energy of the positive ion created due to ionization) and V_o is the ground state energy of the excess electron in that environment. This relationship was first used to express the ionization potential of an impurity in a crystal (Lyons, 1957; Katz

et al., 1969) and was later extended to rare gas (Raz and Jortner, 1969) and hydrocarbon (Holroyd, 1972) liquids. On the basis of Eqn 5.1, it is expected that the changes in I_f (of TMPD) with density and temperature would reflect the effect that these quantities have on V_o and P^+, respectively, since I_g does not depend on T.

Earlier studies (Holroyd and Russell, 1974; Bullot and Gauthier, 1977) have shown that the ionization threshold, I_f, of TMPD in various nonpolar environments (liquids) depends on the temperature of the medium. These authors attributed the observed changes in I_f to the dependence of the V_o and P^+ on changes in the density of the liquid that was induced as the temperature of the medium was varied. Also separate studies (Noda *et al.*, 1975; Tauchert *et al.*, 1977; and Yamaguchi *et al.*, 1979) have shown that the "bottom" of the conduction band, V_o, in ethane depends on the total number density, N. In particular they demonstrated that V_o exhibits a decrease with increasing ethane density reaching a minimum $\simeq 0.2eV$ at a density $N = 6.0 \times 10^{21} molecules/cm^3$ and a subsequent increase for higher N and assumes even positive values (reflecting the localization of the excess electrons) for $N \geq 11 \times 10^{21} molecules/cm^3$. These works have established a general dependence of the V_o on the density of the host medium. They fail however to explicitly differentiate between the effect which is solely due to the density of the medium and that due to the temperature. This is intrinsic to the way these authors were varying the density of the host liquid (or fluid) by just increasing or decreasing it's temperature.

In the present study, the density of ethane was varied independently of the temperature and so was the temperature, allowing therefore to distinguish between their respective effects on the ionization onset of TMPD. The present work shows that the ionization threshold of TMPD embedded in ethane is a function of both the total number density of ethane, N, as well as the temperature, T. These dependencies result from the effect that N and T have on the "bottom" of the conduction band V_o, and on the polarization energy of the medium P^+.

5.2 Experimental Procedure

The procedure and apparatus employed in this study have been described earlier (see Chapter 2). In this work ethane was used as the "buffer" fluid which was obtained from Alphagaz with a minimum purity of 99%. Before use, however, the ethane gas was subjected to several vacuum distillation cycles, so that the air could be removed. The TMPD sample was synthesized by Aldrich Chemical Inc. with a stated purity of 99%. This TMPD sample was subjected to fractional distillation and to several freeze-pump-thaw cycles prior to the measurements.

Because of the low vapor pressure of TMPD (melting point = 323 K; vapor pressure $\approx$ 3 $Torr$ at 373 K) the gas phase measurements were caried out at $T \geq 323\ K$. The number density of TMPD was $\simeq 9.66 \times 10^{18}\ molecules/cm^3$ and the number density of ethane was in the range 0.09 to 8.00 $\times 10^{21}\ molecules/cm^3$. The number density of ethane at each temperature was determined by measuring the pressure at that temperature and then using a 32-term modified MBWR equation of state (Younglove and Ely, 1987) to establish the relationship between the pressure and number density established at each T. In this way the density of ethane was determined with an accuracy of $\pm 3\%$. In Fig. 5.1 the pressure is plotted as a function of the density for various temperatures.

5.3 Results

5.3.1 Photocurrent Signal, I_s, versus Laser Intensity, I_ℓ, Measurements

In the effort to determine the ionization threshold, I_f, and also understand the mechanism through which the ionization occurs, a series of "power measurements" were performed as follows: The photoionization signal I_s was measured as a function of the laser intensity I_ℓ at 5 nm laser wavelength intervals in the region where the two-photon ionization onset of TMPD was expected to lie (420 to 490 nm depending on the number density and temperature of ethane). From these

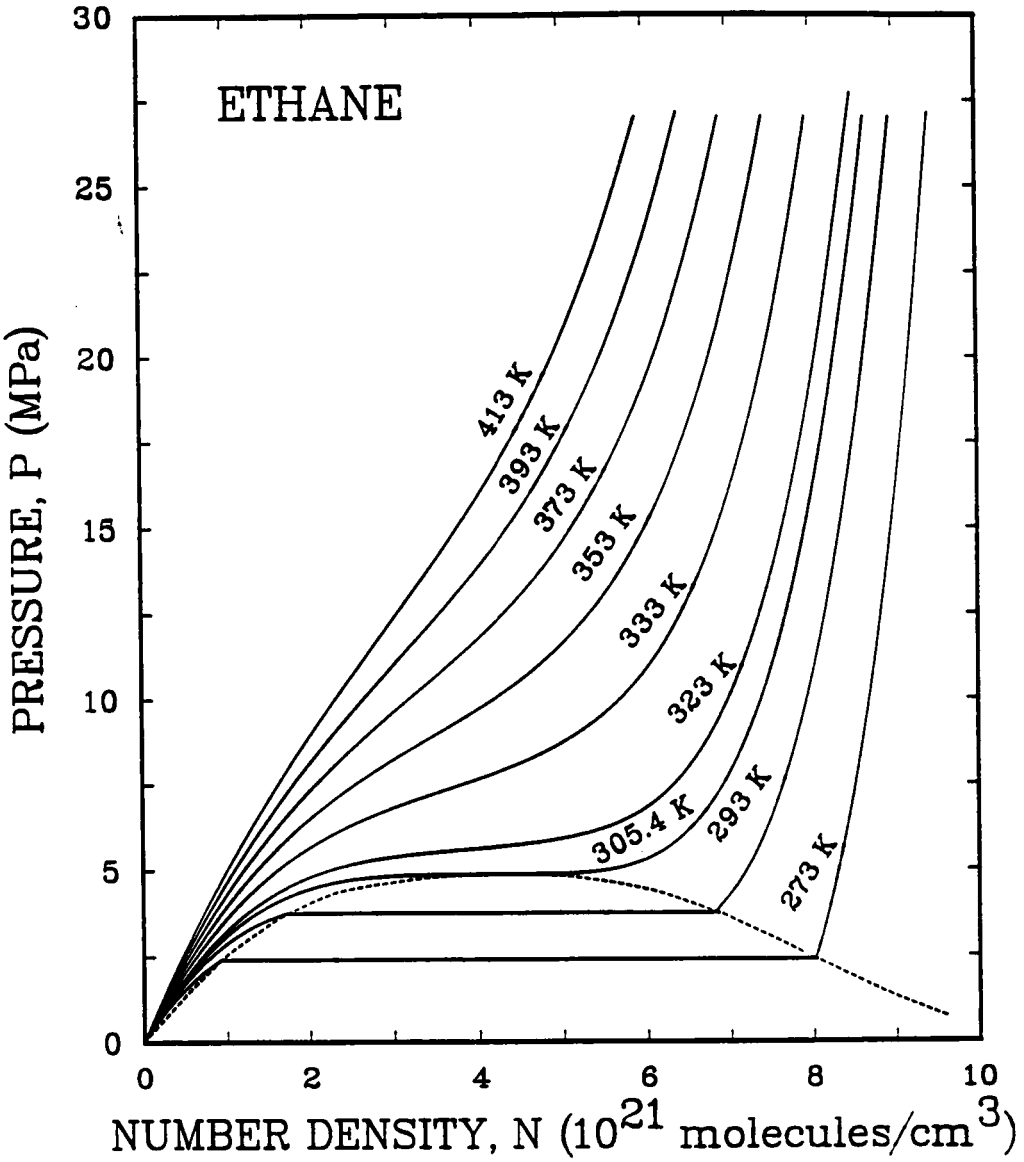

Figure 5.1: Pressure of ethane as a function of ethane number density at different temperatures.

measurements the $\log I_s$ was plotted versus the $\log I_\ell$ as is shown in Fig. 5.2 and the slope

$$S = d\log I_s / d\log I_\ell \tag{5.2}$$

was determined which yields the order of the MPI process (see Chapter 2). These slopes determined at laser wavelength intervals of 5 nm, were then plotted as a function of the laser wavelength λ_ℓ (see Fig. 5.3) for all the densities and temperatures studied. In Fig. 5.3 one can distinguish three laser wavelength regions where: (i) direct two-photon ionization occurs; (ii) two-photon excitation just above the ionization continuum takes place, leading to either direct ionization or relaxation to a lower-lying singlet state and subsequent ionization with the absorption of a third photon; (iii) stepwise three-photon ionization occurs consisting of two-photon excitation below the ionization continuum, relaxation to a lower-lying singlet state, and subsequent ionization with the absorption of a third photon. From plots such as that in Fig. 5.3 the two-photon ionization onset (and from that the value for I_f) was located at the longest wavelength for which a still measurable two-photon component was present in the observed photocurrent signal I_s [which was lying in the wavelengh region (ii)]. This laser wavelength (corresponding to a slope $S = 2.9$) could be determined with an accuracy of $\simeq 5$ nm ($\simeq 0.05$ eV for the I_f).

The measurements were carried out at such laser intensities I_ℓ and ionization signal I_s levels that space charge formation and laser volume saturation were not present.

5.3.2 Ionization Threshold $I_f(N,T)$ of TMPD as a Function of N and T

The ionization threshold $I_f(N,T)$ for TMPD in ethane has been measured as a function of N at 293, 323, 353, 373, 393 and 413 K and is listed in Table 5.1 and is also shown in Figs. 5.4 and 5.5. The ionization onset can be seen to monotonically decrease with increasing ethane density and reaching a minimum value at around 6.0×10^{21} $molecules/cm^3$. At higher number densities a subsequent increase with

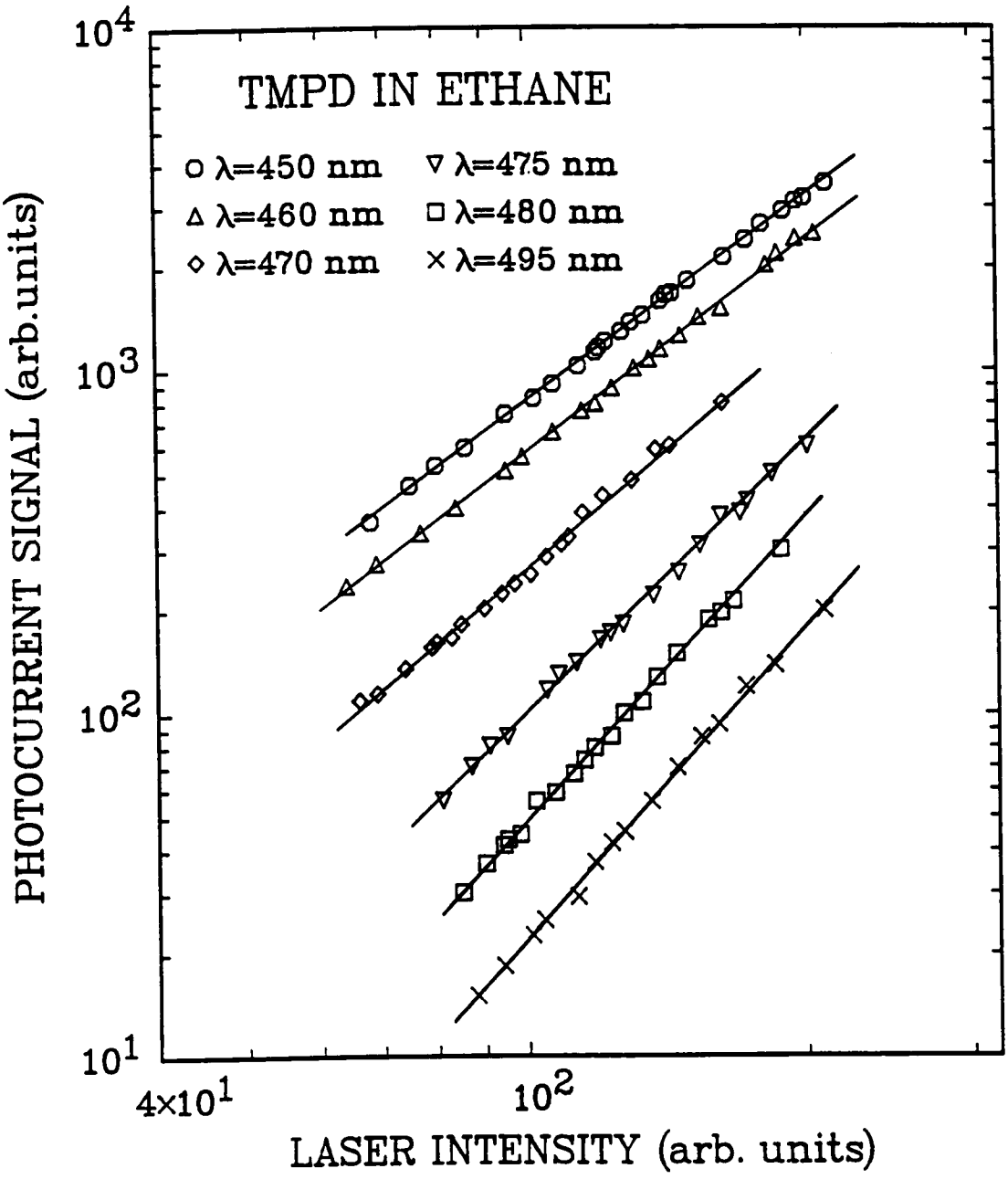

Figure 5.2: Ionization signal versus laser light intensity mesurements of multiphoton ionization of TMPD molecules in ethane at $T = 373\ K$ and $N = 5.18 \times 10^{21}$ $molecules/cm^3$. The slopes are $S = 2.00$ at $\lambda = 450nm$, $S = 2.08$ at $\lambda = 460nm$, $S = 2.30$ at $\lambda = 470nm$, $S = 2.54$ at $\lambda = 475nm$, $S = 2.84$ at $\lambda = 480nm$, $S = 3.03$ at $\lambda = 495nm$.

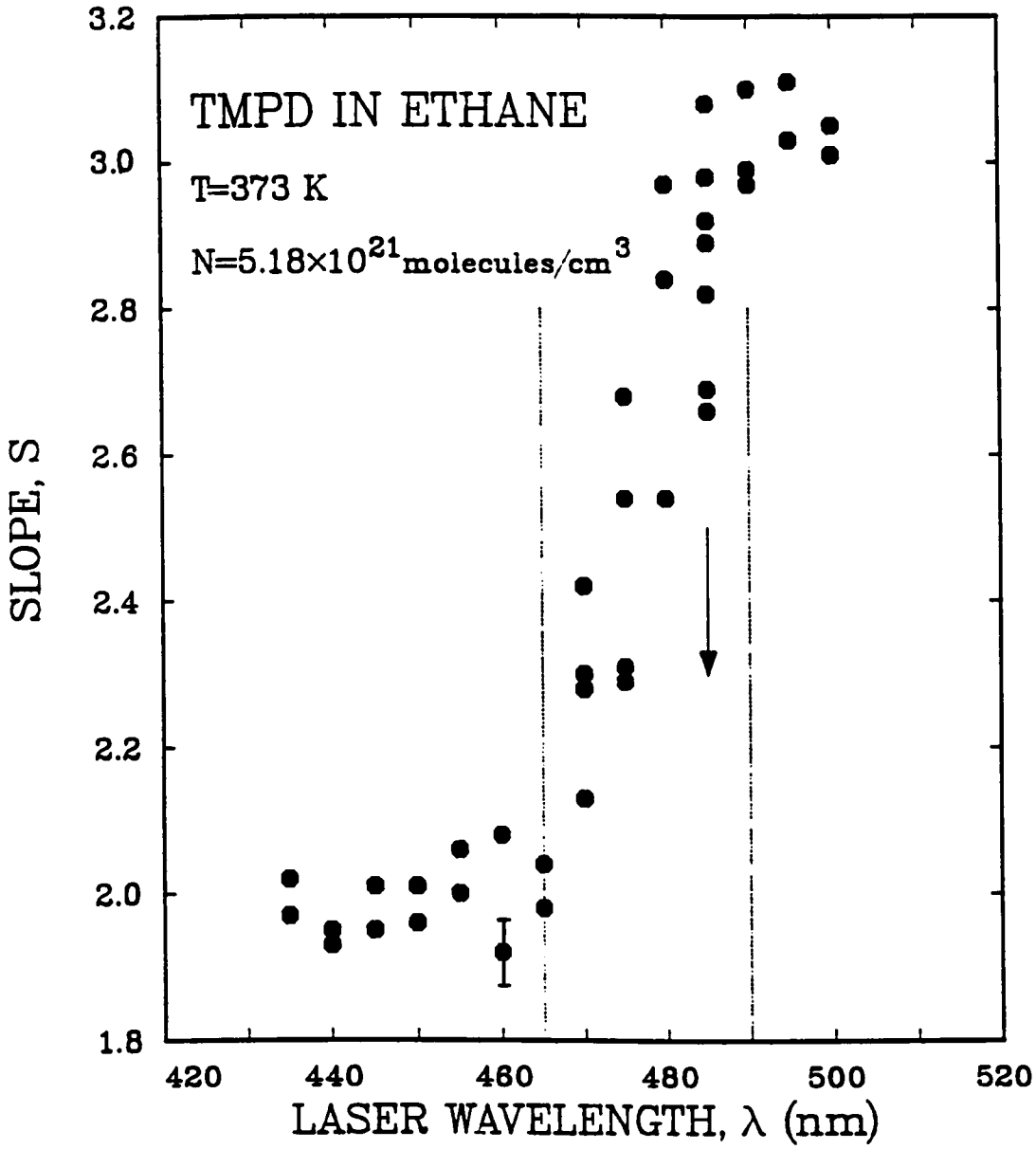

Figure 5.3: The slope S as a function of the laser excitation wavelength λ for TMPD in ethane at $T = 373\ K$ and $N = 5.18 \times 10^{21}\ molecules/cm^3$. The arrow points to the laser wavelength where the two-photon ionization onset is located.

Table 5.1: Ionization threshold of TMPD in ethane as a function of ethane number density N for various temperatures

	I_f (eV)						
N	$T(K)$						
$(10^{21} molecules/cm^3)$	293	323	333	353	373	393	413
0.09		5.90	5.90	5.90	5.90	5.90	5.90
0.06					5.77		
1.24					5.70		
1.33					5.64		
2.32					5.45		
2.35					5.51		
2.50					5.45		
2.65					5.39		
2.95		5.57					
3.25					5.28		
3.34					5.33		
3.55			5.45	5.39	5.33	5.22	5.11
4.43		5.33					
4.76					5.17		
5.18			5.22		5.11		
5.96		5.06					
6.84	5.11						
8.01	5.28						

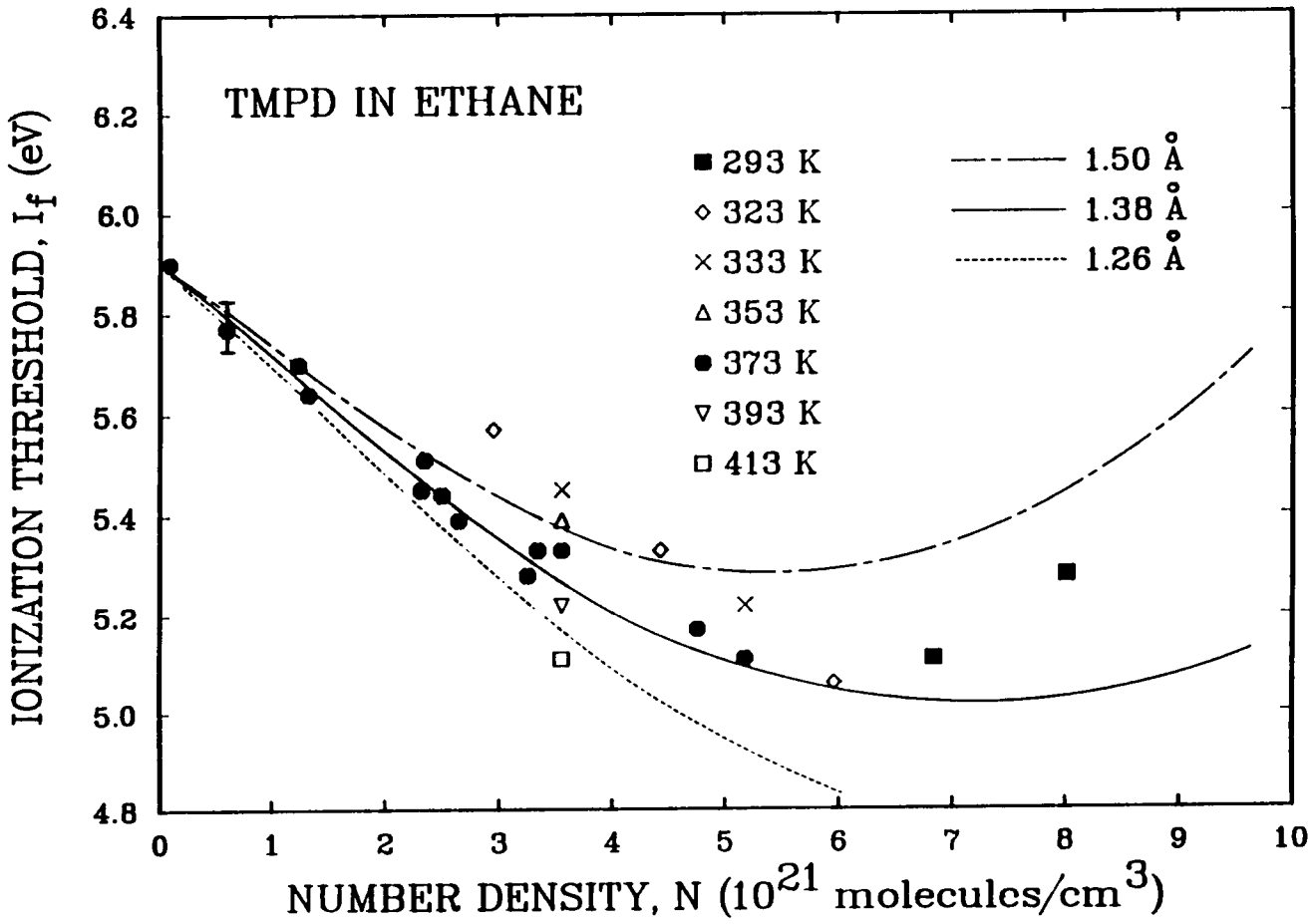

Figure 5.4: Ionization threshold I_f for TMPD in ethane as a function of ethane number density for various temperatures. The curves are the predicted values for I_f using "hard core" radii $\langle\alpha\rangle$: 1.26, 1.38, and 1.50 $\AA$ (see text). The solid squares (■) correspond to liquid phase ethane. The error in the determination of I_f is $\approx 0.05\ eV$.

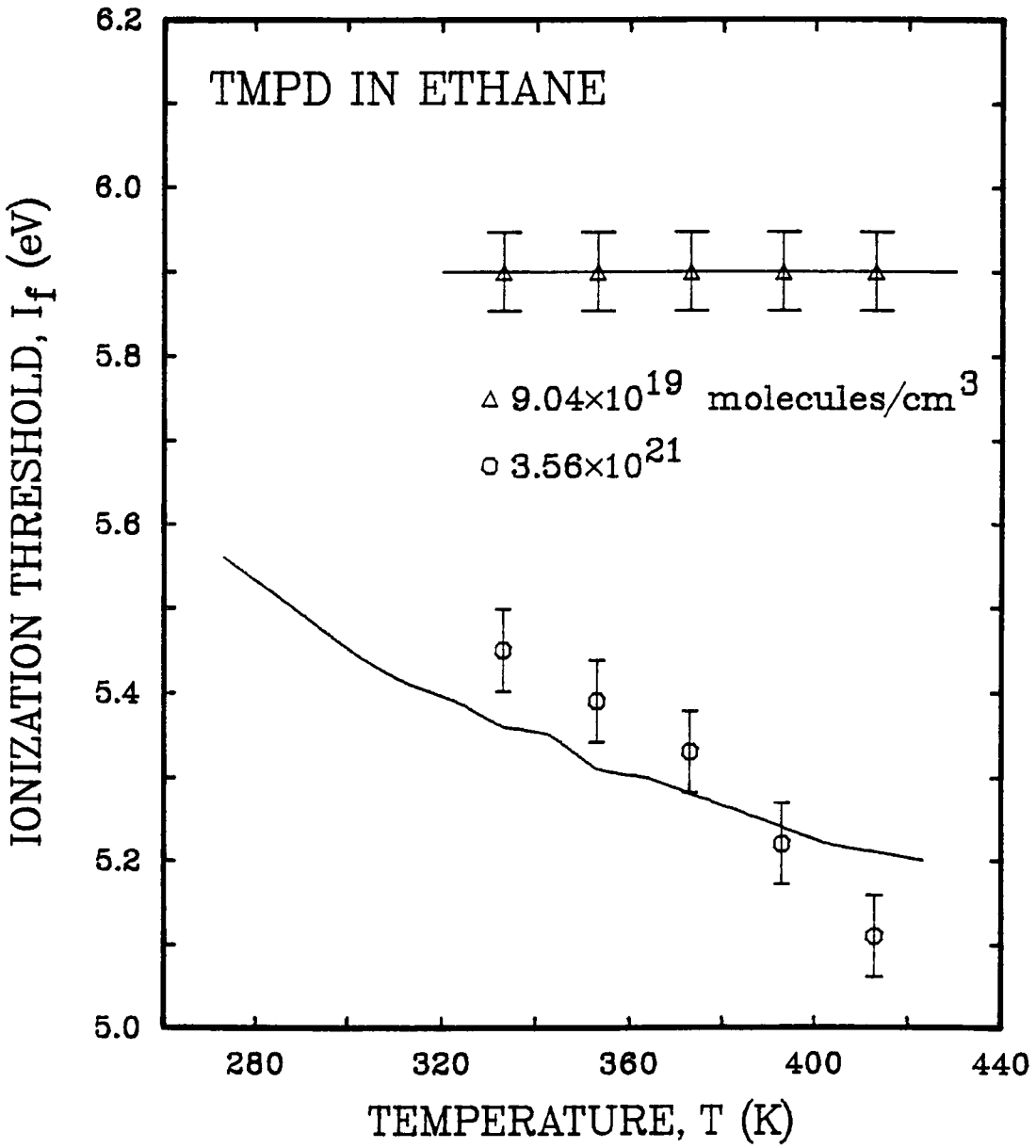

Figure 5.5: Ionization threshold I_f of TMPD in ethane as a function of temperature $T$and the ethane number density N, 9.04×10^{19} (△) and 3.56×10^{21} (○) $molecules/cm^3$. The curves are the predicted values for I_f (see text).

increasing N can be observed particularly at densities higher than 6.6×10^{21} $molecules/cm^3$ which corresponds to ethane in the liquid phase at $T = 293\ K$. The variation of I_f with N at $T = 373\ K$ exhibits a rather smooth behavior even at densities where a phase transition occurs (gas to liquid).

The value for I_f at the density $N = 9.04 \times 10^{19}$ $molecules/cm^3$ was considered to be the ionization potential of the gas phase I_g, since the value of V_o and P^+ can be shown to be very small at these densities. Measurements of the I_g in TMPD vapors were inhibited by the presence of space charge effects. In order to alleviate this problem ethane was added, increasing the total number density from 9.66×10^{18} $molecules/cm^3$ (which corresponds to the vapor pressure of TMPD at 323 K) to $9.04 \times 10^{19} molecules/cm^3$. This procedure yielded a value for I_g which was 5.90 eV. This value for I_g lies below the limit for the ionization onset of TMPD reported by Batley and Lyons (1967) and by Nakato *et al.*, (1971). They determined the ionization threshold from single-photon conductivity spectra of TMPD and reported an upper limit for the adiabatic value of I_g which was $\leq 6.2\ eV$. The difference between the present value and the upper limit for I_g is not inconsistent and can be understood because of the fact that in one-photon measurements the photoionization signal is increasing slowly with increasing photon energy near the region of the ionization onset (Batley and Lyons, 1967) introducing in this manner a difficulty in the determination of the I_g. The value of I_g was found to be independent of the temperature and is listed in Table 5.1 and is plotted in Fig. 5.5.

5.4 Discussion

5.4.1 Effect of Density on the Ionization Threshold of TMPD

The observed dependence of the ionization threshold on the number density of the environment can be understood to originate from the effect the density has on the V_0 and P^+ (see Eqn 5.1). The ground state energy V_o of an excess electron

in a nonpolar dielectric medium such as ethane can be calculated by solving the Schrödinger equation

$$\left(-\frac{\hbar^2}{2m_e}\right)\nabla^2\psi_k(\mathbf{r}) + U(\mathbf{r}) = E_k\psi_k(\mathbf{r}) \tag{5.3}$$

subject to the boundary condition discussed earlier in Chapter 1

$$\left.\frac{\partial\psi_k(\mathbf{r})}{\partial r}\right|_{r=r_s} \tag{5.4}$$

and using an effective potential given by (see Chapter 1)

$$\begin{aligned} U_{eff}(r) \;=\; & -\frac{\alpha e^2}{2}\frac{1}{(r^2+d^2)^2} - \frac{\alpha e^2}{2}\frac{N}{(1+\frac{8}{3}\pi N\alpha)}\left\{\frac{1}{2r}\ln\left[\frac{(r_s+r)^2+d^2}{(r-r_s)^2+d^2}\right]+\right. \\ & \left.\frac{1}{d}\left[\pi - \tan^{-1}\left(\frac{r_s+r}{d}\right) - \tan^{-1}\left(\frac{r-r_s}{d}\right)\right]\right\} \quad a \le r \le r_s \end{aligned} \tag{5.5}$$

where α is the molecular polarizability, a is the "hard core" of the molecule, d is a cut-off distance for the polarization potential ($\simeq 1\mathring{A}$) and r_s is the radius of the Wigner-Seitz cavity given by

$$r_s = \left(\frac{3}{4\pi N}\right)^{1/3} \tag{5.6}$$

The values for the $V_o(= E_{k=0})$ of ethane calculated by numerically solving the Schrödinger equation [with $\alpha = 4.48\mathring{A}^3$ (Kerl and Häusler, 1984) and $d = 1\mathring{A}$] are plotted in Fig. 5.6 as a function of the number density of ethane for various values for the "hard core" radius a. The V_o exhibits first a monotonic decrease with increasing N reaching a minimum and the following subsequent increase of V_o with increasing density results even to positive values for the V_o. It is apparent that the position and depth of the minimum and the location of the density at which the V_o starts becoming positive is very sensitive to the choice of the value of the "hard core". The behavior of V_o with the variation of density also reflects the fact that at high enough densities localization of the excess electrons in ethane occurs (density region for which $V_o \ge 0$).

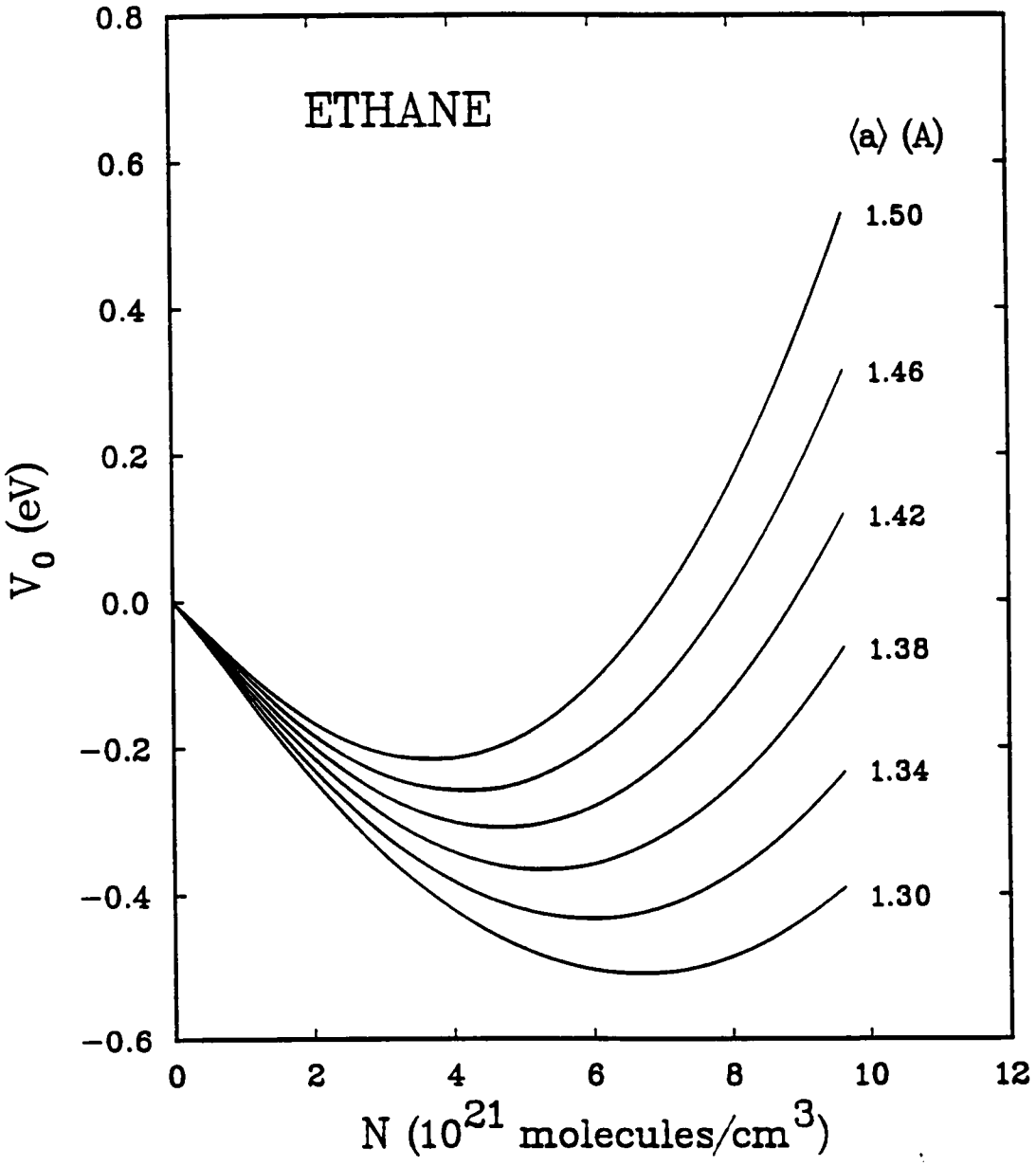

Figure 5.6: Electron Conduction Band energy V_o for ethane as a function of the number density calculated using the Wigner-Seitz method (see text) for "hard core" radii $\langle a \rangle$: 1.30, 1.34, 1.38, 1.42, 1.46, and 1.50 $\AA$.

The medium polarization energy P^+ which is due to the creation of the positive ion of TMPD following its photoionization was usually approximated by the Born formula (see Chapter 1)

$$P^+ = -\frac{e^2}{2r}\left(1 - \frac{1}{\epsilon}\right) \tag{5.7}$$

where e is the electronic charge, ϵ is the relative dielectric constant of the medium and r is the radius of the cavity in which the positive ion finds itself. Alternatively the expression derived earlier (see Chapter 1, subsection 1.3.2) can be employed, to estimate the values for P^+, viz.,

$$\begin{aligned} P^+ \;=\; & -\frac{3\alpha e^2 \pi N}{2(1+\frac{8}{3}\pi\alpha N)}\frac{1}{r_s}\frac{1}{x^3}\left\{\frac{1}{4}\left(x^2+1+y^2/3\right)\ln\left[\frac{(x+1)^2+y^2}{(x-1)^2+y^2}\right] - \right. \\ & \left. \frac{x^3+1}{3y}\tan^{-1}\left(\frac{x+1}{y}\right) + \frac{x^3-1}{3y}\tan^{-1}\left(\frac{x-1}{y}\right) - \frac{x}{3} + \frac{\pi x^3}{3y}\right\} \end{aligned} \tag{5.8}$$

where

$$x = \frac{r_o}{r_s} \qquad \text{and} \qquad y = \frac{d}{r_s} \tag{5.9}$$

where r_s is the "radius" of the cavity in which the TMPD molecule resides. Generally this quantity can be directly estimated by means of the relationship 5.3. When, however, the size of the Wigner-Seitz cavity in ethane is not large enough to "accomodate" the TMPD molecule then the cavity should be considered to have the dimensions of the TMPD molecule. Crystallographic studies (Ikemoto, 1979) of TMPD at 298 K have shown that the density or the crystallized TMPD is 1.09 g/cm^3 which corresponds to a "radius" of an equivalent spherical cavity $r_s = 3.91\mathring{A}$ which in turn corresponds to an ethane density $N_o = 3.61 \times 10^{21}\ molecules/cm^3$. Faidas *et al.*, (1988) have measured the density of liquid TMPD at 324 K and found a density 0.925 g/cm^3 which corresonds to $r_s = 4.09\mathring{A}$. In this work the the radius of the cavity where the TMPD molecule finds itself was assumed to be given by

$$r_s = \begin{cases} (3/4\pi N)^{1/3} & \text{if } N \leq N_o \\ 3.9\mathring{A} & \text{if } N \geq N_o \end{cases} \tag{5.10}$$

The calculated values for the P^+ are plotted in Fig. 5.7. They can be seen to decrease monotonically with increasing ethane density. There is, then, a density range where both the V_o and the P^+ decrease with increasing density resulting in a decrease of the ionization threshold with density. At higher densities where the V_o reaches a minimum, the P^+ is still decreasing with increasing density and hence at these densities the decrease in I_f is due to the decrease in P^+. Above that density the V_o is an increasing function of N while the P^+ is a decreasing function of N introducing in this way a competition between them which is reflected in the variation of I_f with N as can be seen in Fig 5.4.

5.4.2 Effect of Temperature on the Ionization Threshold of TMPD

The value of the energy of an excess electron at the "bottom" of the conduction band of ethane which was calculated in the previous subsection, does not show any direct dependence on the temperature. However, it is a delicate function of the "hard core" radius of the ethane molecule, a, as can be seen from Fig. 5.6. The a can be assumed to be related to the electron scattering cross section σ when only $s-$wave scattering is present (*i.e.*, at low electron energies) by

$$\sigma = 4\pi a^2 \tag{5.11}$$

The electron scattering cross section as a function of electron energy, $\sigma(\epsilon)$, has been reported by Dunkan and Walker (1974) and is plotted as a function of the incident electron energy in Fig. 5.8. If one assumes that the excess electrons in ethane produced by the photoionization of the TMPD molecule are distributed with a Maxwell-Boltzmann energy distribution function characteristic of the T of ethane, then an average electron scattering cross section can be obtained as a function of T, viz.,

$$\langle\sigma\rangle(T) = \frac{2}{\sqrt{\pi}(kT)^{3/2}} \int_0^\infty d\epsilon \epsilon^{1/2} \mathrm{e}^{-\epsilon/kT} \sigma(\epsilon) \tag{5.12}$$

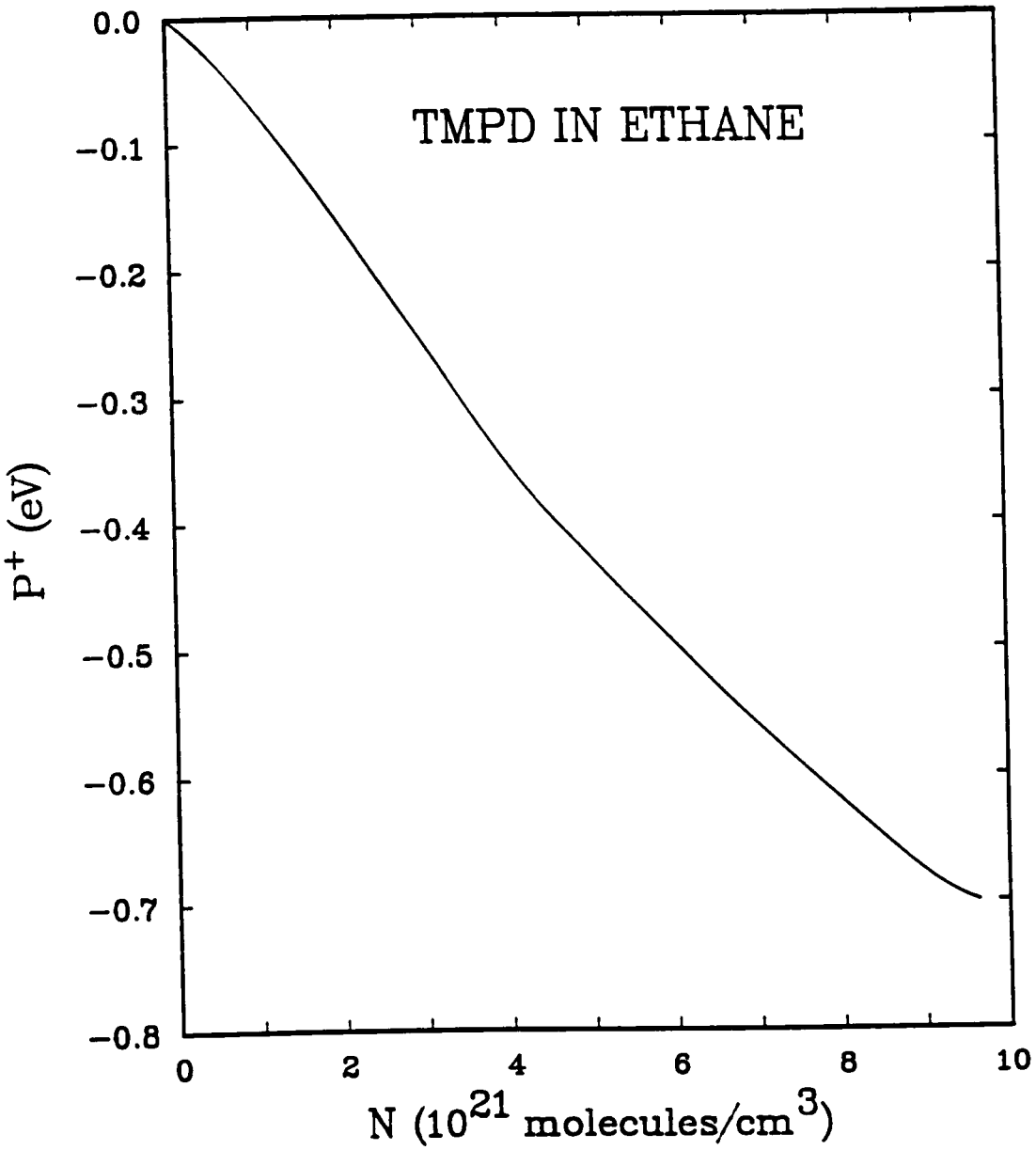

Figure 5.7: The polarization energy of ethane P^+ (due to the presense of $TMPD^+$) as a function of ethane density.

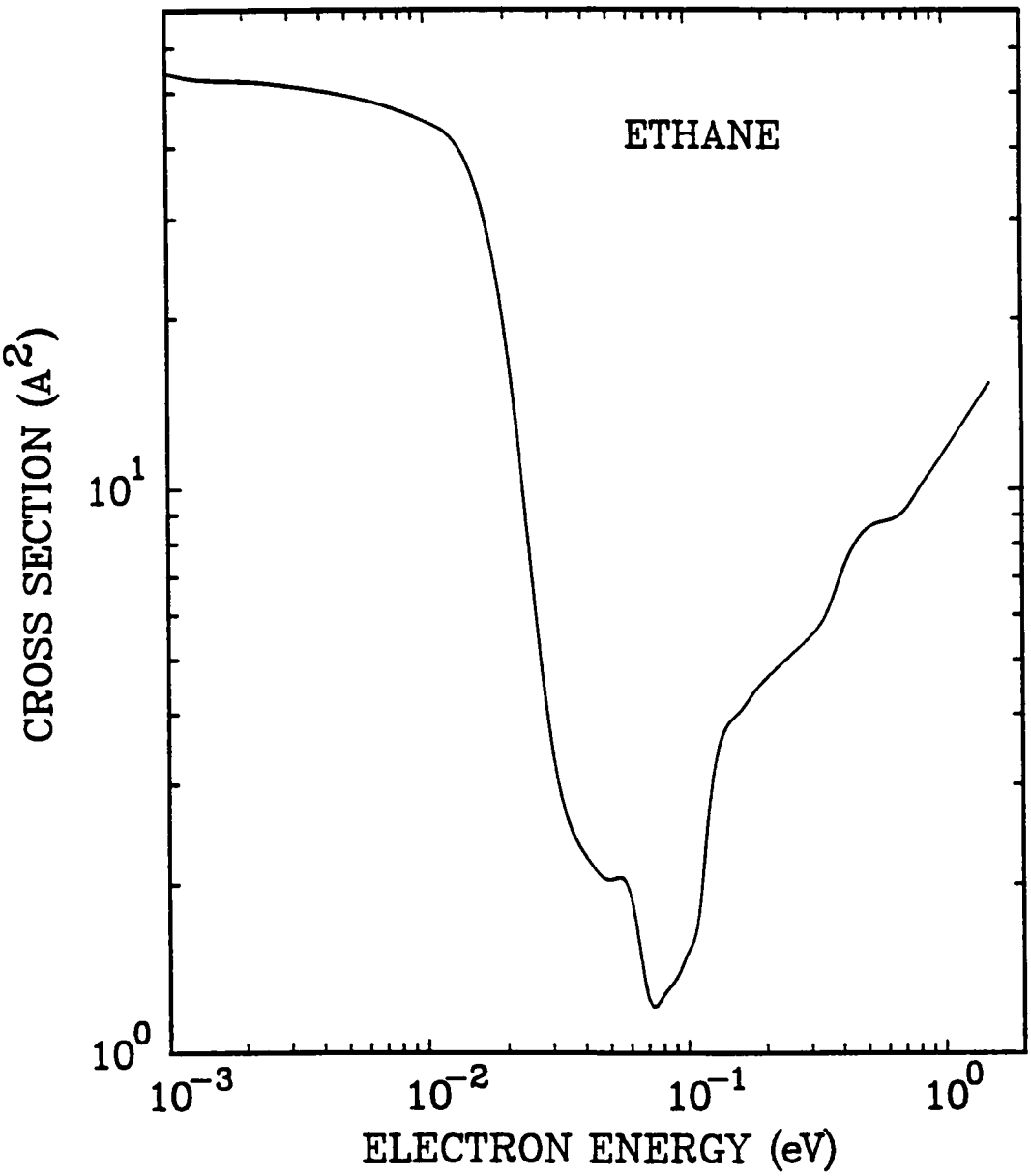

Figure 5.8: The electron scattering cross section σ deduced by Duncan and Walker (1974) from an analysis of low-energy transport data in ethane, as a function of the electron energy.

The calculated values of $\langle\sigma\rangle(T)$ for ethane determined in this way are listed in Table 5.2 for T values in the range 273 to 423 K and they can be seen to decrease with increasing T in this temperature range. The decrease of the mean thermal electron scattering cross section, $\langle\sigma\rangle(T)$, with T for ethane has been reported also by other authors (Christophorou *et al.*, 1976; Nishikawa *et al.*, 1980). The decrease in $\langle\sigma\rangle(T)$ for ethane can be undestood because electrons at higher T possess higher mean energies and so when they collide with ethane molecules the scattering cross section becomes smaller as can be seen from Fig. 5.8 as long as the electron energies are smaller than $\approx 0.08\ eV$ where the Ramsauer minimum occurs. Similarly, values for an average "hard core" radius $\langle a\rangle(T)$ can be obtained as a function of T and are listed in Table 5.2. It is clear that $\langle a\rangle(T)$ also decreases at T increases in this temperature range (273 to 413 K). The $\langle a\rangle(T)$ were normalized so that $\langle a\rangle = 1.40\mathring{A}$ at $T = 373\ K$. This was done because when the V_o was calculated as a function of N by solving Eqn 5.3 with $\langle a\rangle(T = 300K) = 1.40\mathring{A}$ then the determined I_f through Eqn 5.1 as a function for N, best fitted the experimental measurements on $I_f(N)$ (see Fig. 5.4). The normalized values for $\langle a\rangle$ in the temperature T range 273 to 423 K are listed in Table 5.2.

The medium polarization energy, P^+, can be seen to depend on the temperature through the dielectric constant ϵ (Eqn 5.7 or through the polarizability α (Eqn 5.8). Both of these quantities, for the temperature ranges studied, have been shown (Weber, 1976; Younglove and Ely, 1987; Kerl and Häusler, 1984) to depend so little on the temperature, that the effect of T on P^+ through them can be ignored. It should be pointed out, however, that in the derivation of Eqn 5.8 a step function was employed to approximate the pair distribution function (see Chapter 1) excluding in this way any possible effects on $g(r)$ (and through it on the P^+) due to the temperature.

Table 5.2: Temperature dependence of the average thermal electron scattering cross section and "hard core" for ethane

T (K)	$\langle\sigma\rangle$ $(\mathring{A}^2)$	$\langle a\rangle$ $(\mathring{A})$	$\langle a\rangle^a$ $(\mathring{A})$
273	17.04	0.97	1.68
293	15.93	0.93	1.61
303	15.43	0.91	1.57
313	14.96	0.89	1.54
323	14.51	0.88	1.52
333	14.09	0.86	1.49
343	13.69	0.85	1.47
353	13.31	0.83	1.43
363	12.96	0.82	1.42
373	12.62	0.81	1.40
383	12.31	0.79	1.37
393	12.00	0.78	1.35
403	11.72	0.77	1.33
413	11.45	0.76	1.31
423	11.19	0.75	1.30

[a] values of $\langle a\rangle$ normalized so that at $T = 373\ K$ $\langle a\rangle = 1.40\mathring{A}$

While the absolute values for $\langle a \rangle (T)$ may be uncertain, unequivocally the $\langle a \rangle (T)$ decreases with increasing T. Employing the normalized values for $\langle a \rangle (T)$, the V_o for $N = 3.55\ molecules/cm^3$ can be calculated as a function of T and since the P^+ is $T-$independent, the I_f can be determined as a function of T through Eqn 5.1. The predicted dependence of I_f on T is plotted in Fig. 5.5 and is represented by the solid line. It can be seen that clearly I_f decreases with increasing T in the T range 273 to 413 K. Then the experimentally observed changes in I_f with T, plotted in Fig. 5.5 and attributed to the decrease in V_o with increasing T can be rationalized.

Chapter 6

Summary and Conclusions

The effect of temperature and the total number density on the attachment of low-energy (0-10 eV) electrons to three polyatomic molecules ($n-C_4F_{10}$, $n-C_6F_{14}$, and SO_2F_2) has been studied using a High Temperature Electron Swarm technique (HTESA). Also the effect of temperature and density on the ionization threshold of a polyatomic molecule (N,N,N′,N′-tetramethyl-p-phenylenediamene) has been investigated using a Multiphoton Ionization Conductivity (MPIC) technique.

The total electron attachment rate constant $k_a(\langle\epsilon\rangle, T)$ for $n-C_4F_{10}$ and $n-C_6F_{14}$ has been measured in the buffer gas of Ar and over mean electron energy, $\langle\epsilon\rangle$, range 0.41 to 4.82 eV at the temperatures T: 300, 350, 400, 450, 500, 550, 600, 675, and 750 K and over the total gas number density range 2.25 to 12.88×10^{19} $molecules/cm^3$. From the measured $k_a(\langle\epsilon\rangle, T)$, the $\sigma(\epsilon, T)$ were determined for $n-C_4F_{10}$ and $n-C_6F_{14}$ at all the temperatures studied by employing the electron swarm unfolding technique. These polyatomic molecules were found to attach electrons both nondissociatively and dissociatively over wide mean electron energies (0.0 to 5.0 eV) and by comparing the results of the present studies with similar earlier work on C_2F_6 and C_3F_8 it was concluded that the mode of production of negative ions strongly depends on the molecular size for these perfluoroalkanes.

The $k_a(\langle\epsilon\rangle, T)$ for $n-C_4F_{10}$ were found to increase with increasing total gas number density N_t for $T \leq 500$ K. At 500 K, the $k_a(\langle\epsilon\rangle, T)$ depended on N_t only for $\langle\epsilon\rangle \leq 1.5eV$ and were found to be independent of N_t at higher values of

$\langle\epsilon\rangle$. The dependence of $k_a(\langle\epsilon\rangle, T)$ on N_t can be understood because as T increases the measured $k_a(\langle\epsilon\rangle, T)$ are increasingly dominated by the contribution of the dissociative electron attachment processes which do not depend on N_t. In the temperature range 300 to 500 K where there is a large contribution from the nondissociative electron attachment, the effect of N_t on $k_a(\langle\epsilon\rangle, T)$ is large, being more profound at higher $\langle\epsilon\rangle$ and T since the lifetimes of the transient negative ions decrease with both the $\langle\epsilon\rangle$ and T. At low $\langle\epsilon\rangle$ the $k_a(\langle\epsilon\rangle, T)$ are almost independent of N_t, because the lower the $\langle\epsilon\rangle$, the longer lived the parent negative ions are.

The $k_a(\langle\epsilon\rangle, T)$ for $n-C_6F_{14}$ did not exhibit any dependence on the total gas number density N_t. They were found, however, to show a delicate dependence on T. They initially increase with increasing T between 300 and 350 K, and this increase is due to the contribution of the dissociative electron attachment which results in the formation of fragment negative ions. At T between 350 and 550 K the contribution of the nondissociative electron attachment increases and this is reflected in the decrease in $k_a(\langle\epsilon\rangle, T)$ with T in this temperature range. At $T \geq 550$ K the dissociative electron attachment process predominates as is revealed by the increase in $k_a(\langle\epsilon\rangle, T)$ with T.

As a result of the delicate temperature dependencies of the nondissociative and dissociative contributions to the total electron attachment, the position of maximum of the total electron attachment rate constant changes little with increases in T as long as the nondissociative contribution is larger than the dissociative. When, however, the dissociative electron attachment process predominates, the position of the maximum shifts to lower mean electron energies with increasing T.

The $\sigma_a(\epsilon, T)$ for $n-C_4F_{10}$ first decreases with increasing T in the temperature range 300 to 500 K because in this temperature range it contains a large contribution from the nondissociative electron attachment (which decreases as T increases). Very interestingly, however, the $\sigma_a(\epsilon, T)$ for this molecule peaks at progressively higher electron energies in this $T-$range reflecting the preponderance of the parent anions as T increases. Above 500 K the competition between the nondissociative and dissociative electron attachment favors the latter which results in the increase

in the $\sigma_a(\epsilon, T)$ with increasing T, and the electron energy at which the maximum occurs in $\sigma_a(\epsilon, T)$ shifts to lower electron energies. For $n-C_6F_{14}$, the $\sigma_a(\epsilon)$ first increases with increasing T between 300 and 400 K, due to prevalence of the dissociative electron attachment and in this $T-$range the peak shifts to progressively lower ϵ. It then exhibits a precipitous decrease between 400 and 500 K revealing a large contribution from the parent negative ion formation, and the peak in $\sigma_a(\epsilon, T)$ shifts to higher electron energies. Subsequently it starts increasing for $T \geq 550$ K, as a higher-lying dissociative electron attachment process predominates in this temperature range, as expected; the peak position shifts to lower electron energies. The Full Width at Half Maximum (FWHM) for the dissociative electron attachment cross section $(\sigma_a)_d(\epsilon, T)$ increases with increasing T, demonstrating the broadening of the Franck-Condon region because of the population of higher vibrational levels with increasing T.

The total electron attachment rate constant, $k_a(\langle\epsilon\rangle, T)$, for SO_2F_2 has been measured in the carrier gas of N_2, in the mean electron energy range 0.07 to 0.911 eV at 300, 400, 500, 600, and 700 K and over the total gas number density range 2.25 to 6.44 $\times$ 10^{19} $molecules/cm^3$. The total electron attachment cross section $\sigma_a(\epsilon)$ was determined by unfolding the $k_a(\langle\epsilon\rangle, T)$ over the electron energy distribution function for N_2. The SO_2F_2 was found to attach electrons by forming both parent anions and fragment negative ions at $T = 300$ K. Above 300 K the formation of the parent negative ions disappears and SO_2F_2 attaches electrons exclusively though dissociative electron attachment processes.

The $k_a(\langle\epsilon\rangle, T)$ for SO_2F_2 were found to increase with increasing T and were not dependent on the total gas number density N_t. Again the increase in $k_a(\langle\epsilon\rangle, T)$ with T is attributed to the increase in the dissociative electron attachment. The deduced total electron attachment cross section at 300 K exhibits an increase below $\approx 0.1eV$ and a maximum at $\approx 0.22eV$. The former is attributed to formation of parent negative ions (nondissociative electron attachment) and the latter to the contribution of the dissociative electron attachment. The weak contribution to $\sigma_a(\epsilon, T)$ from the nondissociative electron attachment which is evident at 300 K

vanishes at higher temperatures. At 400 K the increase in $\sigma_a(\epsilon, T)$ below ≈ 0.1 eV as $\epsilon \rightarrow 0.0$ eV disappears and only a main peak in $\sigma_a(\epsilon, T)$ exists. This maximum moves toward smaller electron energies with increasing T, demonstrating the preponderance of the fragment negative ions.

The ionization threshold, I_f, of TMPD in fluid ethane (*i.e.*, the minimum photon energy required to produce an electron and a TMPD positive ion) was measured as a function of the ethane number density at 293, 323, 353, 373, 393, and 413 K. The I_f was found to be a function of both the ethane number density and the temperature. The I_f decreases with increasing N at $T = 373$ K reaching a minimum value of $5.11eV$ at $N = 6.0 \times 10^{21}$ $molecules/cm^3$. At higher number densities ($N \geq 6.6 \times 10^{21}$ $molecules/cm^3$) and at $T = 293$ K the I_f was found to increase with increasing N. The effect of N on the I_f results from the dependence of both the V_o on the ethane number density, which can be either negative (quasi-free excess electrons) or positive (localized electrons), and the dependence of the P^+, which is always negative, on the number density of ethane.

At a constant number density, $N = 9.66 \times 10^{19}$ $molecules/cm^3$, the measured $I_f = 5.90eV$ was $T-$independent and was considered to correspond to the ionization onset, I_g, of the gaseous phase. At $N = 3.56 \times 10^{21}$ $molecules/cm^3$ the I_f was found to decrease with increasing T in the temperature range 333 to 413 K. The effect of temperature on the I_f is attributed to the decrease in the mean electron scattering cross section which itself results from the decrease of the V_o with T between 333 and 413 K.

Finally, the following suugestions can be made regarding experiments that might provide additional information on the processes studied in this work:

a. Excitation of a particular vibrational mode of the molecule employing tunable lasers which could further clarify the role of each vibrational mode to the nondissociative and dissociative electron attachment.

b. Studies of the ionization threshold of a molecule over wider temperature ranges and in different media.

List of References

List of References

Adams, N. G., Smith, D., Alge, E., and Burdon, J., Chem. Phys. Lett. 116, 460 (1985).

Alge, E., Adams, N. G., and Smith, D., J. Phys. B 17, 3827 (1984).

Bardsley, J. N., Herzenberg. A., and Mandl, F., In Atomic Collision Processes. (M. R. C. McDowell, ed.). Amsterdam: North-Holland, 1964, pp. 415-427.

Bardsley, J. N., Herzenberg, A., and Mandl, F., Proc. Phys. Soc. London 89, 321 (1966).

Bardsley, J. N., and Wadehra, J. M., Phys. Rev. A 20, 1938 (1979).

Batley, M., and Lyons, L. E., Molecular Crystals, 3, 357 (1968).

Blatt, J. M., and Weisskopf, V. F., In Theoretical Nuclear Physics. New York John Willey and Sons, Inc., (1952)

Boesl, V., Neusser, H. ,J., and Schlag, E., W., J. Chem. Phys. 55, 193, (1981)

Born, M., Z. Phys. 1, 45, (1920).

Bortner, T. E., and Hurst, G. S., Health Phys. 1, 39 (1958).

Breit, G., and Teller, E., Astrophys. J. 91, 215 (1940).

Brooks, H. L., Hunter, S. R., and Nygaard, K. J., J. Chem. Phys. 71, 1870 (1979).

Bullot, J., and Gauthier, M., Can. J. Chem. 55, 1821, (1977).

Bunkin, F. V., and Prokhorov, A. M., Soviet Phys. JETP 19, 739 (1964)

Chantry, P. J., J. Chem. Phys. 51, 3369 (1969).

Chen, J. C. Y., Phys. Rev. 148, 66 (1966).

Chen, J. C. Y., and Peacher, J. L., Phys. Rev. 163, 103 (1967).

Chin, S. L., and Lambropoulos, P., In Multiphoton Ionization Processes of Atoms. New-York: Academic Press, 1984.

Christodoulides, A. A., Christophorou, L. G., Pai, R. Y., and Tung, C. M., J. Chem. Phys. 70, 1156 (1979).

Christophorou, L. G., In Atomic and Molecular Radiation Physics. New-York: Wiley-Interscience, (1971).

Christophorou, L. G., Adv. Electron. and Electron Phys. 46, 55 (1978).

Christophorou, L. G., Environ. Health Perspect. 36, 3 (1980).

Christophorou, L. G., In Electron-Molecule Interactions and their Applications. New York: Academic Press, 1984.

Christophorou, L. G., J. Chem. Phys. 83, 6543 (1985).

Christophorou, L. G., Contrib. Plasma Phys. 27, 237 (1987).

Christophorou, L. G., and Hunter, S. R., In Electron-Molecule Interactions and Their Applications. (L. G. Christophorou, ed.), Vol. 2. New-York: Academic Press, 1984, pp. 317-422.

Christophorou, L. G., Hunter, S. R., Carter, J. G., and Spyrou, S. M., In Swarm Studies and Inelastic Electron-Molecule Collisions. (L. G.Christophorou, Pitchford, B. V. McKoy, A. Chutjian, and S. Trajmar, eds.). New-York: Springer-Verlag, 1987, p.303.

Christophorou, L. G., Grant, M. W., and Pittman, D., Chem. Phys. Lett. 38, 100 (1976).

Christophorou, L. G., McCorkle, D. L., and Anderson, V. E., J. Phys. B 4, 1163 (1971).

Christophorou, L. G., McCorkle, D. L., and Christodoulides, A. A., In Electron-Molecule Interactions and Their Applications. (L. G. Christophorou, ed.), Vol. 1. New-York: Academic Press, 1984, pp. 477-617.

Christophorou, L. G., Grant, M. W., and Pittman, D., Chem. Phys. lett., 38, 100 (1976).

Christophorou, L. G., and Siomos, K. In Electron-Molecule Interactions and Their Applications. (L. G. Christophorou, ed.), Vol. 2, New-York: Academic Press, 1984, pp.221-316.

Compton , R. N., Christophorou, L. G., Hurst, G. S., and Reinhardt, P. W., J. Chem. Phys. 45, 4634 (1966).

Crance, M., In Multiphoton Ionization of Atoms. (S. L. Chin and P. Lambropoulos Eds.). New York: Academic Press, 1984, pp. 65-108

Dalgarno, A., Adv. Phys. 11, 281 (1962).

Datskos, P. G., and Christophorou, L. G., J. Chem. Phys. 86, 1982 (1987).

Duncan, C. W., and Walker, I. C., J. Chem. Soc. Faraday Trans. II 70, 577 (1974).

Faidas, H., Ph.D. Dissertation, University of Tennessee, Knoxville, 1985.

Faidas, H., and Christophorou, L. G., J. Chem. Phys. 86, 2505 (1987).

Faidas, H., and Christophorou, L. G., J. Chem. Phys. 88, 8010 (1988a).

Faidas, H., and Christophorou, L. G., Radiat. Phys. Chem. 32, 433 (1988b).

Faidas H., Christophopou, L. G., Datskos, P. G., McCorkle, D. L., J. Chem. Phys. (to be published).

Faidas, H., and Siomos, K., J. Chem. Phys. 87, 5097 (1987).

Fite, W. L., Brackmann, R. T., and Henderson, W. R., Proc. Fourth Int. Conf. on the Phys. of Electron and Atomic Coll. New-York: Science, Bookcrafters, Inc., Hastings-onHudson, 1965, p.100.

Gambler, W., Naturforsch, 40b, 782 (1985).

Goans, R. E., and Christophorou, L. G., J. Chem. Phys. 60, 1036 (1974).

Goeppert-Mayer, M., Ann. Phys. 9, 273 (1931).

Harland, P. W., and Thynne, J. C. J., Int. J. Mass Spectrom. Ion. Phys. 11, 445 (1973).

Hasted, J. B., Mathur, D., In Electron-Molecule Interactions and their Applications. (L. G. Christophorou ed.), Vol. 1. New York: Academic Press, 1984, pp. 403-475.

Henderson, W. R., Fite, W. L., and Brackmann, R. T., Phys. Rev. 183, 157 (1969).

Hernandez-Gil, N., Wentworth, W. F., Limero, T., and Chen, E. C. M., J. Chromatogr. 312, 31 (1984).

Herzenberg, A J. Chem. Phys. 51, 4949 (1969).

Holroyd, R. A., J. Chem. Phys. 57, 3007 (1972).

Holroyd, R. A., and Russel, L. R., J. Chem. Phys. 78, 2128, 1974.

Hunter, S. R., and Christophorou, L. G., In Electron-Molecule Interactions and Their Applications. (L. G. Christophorou, ed.), Vol. 2. New-York: Academic Press, 1984a, pp. 89-219.

Hunter, S. R., and Christophorou, L. G., J. Chem. Phys. 80, 6150 (1984b).

Hunter, S. R., Christophorou, L. G., McCorkle, D. L., Sauers, J., Ellis, H. W.,

and James, D. R., J. Phys. D 16, 573 (1983).

Hurst, G. S., and Bortner, T. E., Phys. Rev. 114, 116 (1959).

Huxley, L. G. H., and Crompton, R. W., In The Diffusion and Drift of Electrons in Gases. New-York: Willey (Interscience), 1974.

Ikemoto, I., Acta Cryst. B35, 2264 (1979).

Jortner, J., and Gaathan, A., Can. J. Chem. 55, 1801 (1977).

Katz, B., Brith, M., Sharf, B., and Jortner, J., J. Chem. Phys. 50, 5195 (1969).

Kerl, K., Häusler, H., Ber. Bunsenges. Phys. Chem. 88, 992 (1984).

Kittel, C., Introduction to Solid State Physics. New York: Jonh Willey & Sons, 1976.

Kivel B., Phys. Rev. 116, 926, 1959.

Landau L. D., and Lifshitz E. M., Quantum Mechanics. Oxford: Pergamon Press, 1977.

Lane, N. F., Rev. Mod. Phys. 52, 29 (1980).

Lekner, J., Phys. Rev. 158, 130, 1967.

Lorentz, H. A., The Theory of Electrons. New York: Dover Publications, 1952.

Luft, P. E., Description of a Backward Prolongation Program for Computing Transport Coefficients JILA Report No. 14, University of Colorado, Boulder, Colorado, 1975.

Lyons, E. E., J. Chem. Soc. PTVI, 5001, 1957.

Massey, H. S. W., In Negative Ions. London: Cambridge University Press, 1976.

Mott, N. F., and Massey, H. S. W., In The theory of Atomic collisions. Vol 2, Oxford: Oxford University Press, 1971.

Nakato, Y., Ozaki, M., Egawa, A., and Tsubomura, H., Chem. Phys. Lett., 9, 615 (1971).

Nishikawa, M., Holroyd, R. H., Sowada, U., J Chem. Phys. 72, 3081 (1980).

Noda, S., Kevan, L., Fueki, K., J. Chem. Phys. 79, 2866, (1975).

O'Malley, T. F., Phys. Rev. 150, 14 (1966).

O'Malley, T. F., Phys. Rev. 155, 59 (1967).

Oppenheimer, J. R., Phys. Rev. 32, 361 (1928).

Raz, B., and Jortner, J., Chem. Phys. Lett. 4, 155, 1969.

Reese, R. M., Dibeler, V. H., and Franklin, J. L., J. Chem. Phys. 29, 880 (1958).

Sauers, I., Christophorou, L. G., and Carter, J. G., J. Chem. Phys. 71, 1156 (1979).

Sauers, I., Christophorou, L. G., and Spyrou, S. M., In Gaseous Dielectrics IV (L. G. Christophorou and M. O. Pace, eds.). New York: Pergamon Press, 1984.

Shimanouchi, T., J. Phys. Chem. Ref. Data 1, 1 (1972).

Shimamori, H., and Fessenden, R. W., J. Chem. Phys. 70, 1137 (1974).

Shimoji, M., Liquid Metals. London: Academic Press, 1977.

Siomos, K., and Christophorou, L. G., Chem. Phys. Lett. 72, 43 (1980).

Smirnov, B. M., Negative Ions. New-York: McGraw Hill, 1982.

Smith, J., Adams, N. G., and Alge, E., J. Phys, B 17, 461 (1984).

Spence, D., Schultz, G. J., J. Chem. Phys. 58, 1800 (1973).

Springett, B. E., Jortner J., and Cohen, Morrel H., Phys. Rev. 48, 2720 (1968).

Spyrou, S. M., Ph.D. Dissertation, University of Tennessee, Knoxville, 1983.

Spyrou, S. M., and Christophorou, L. G., J. Chem. Phys. 82, 2620 (1985a).

Spyrou, S. M., and Christophorou, L. G., J. Chem. Phys. 83, 2829 (1985b).

Spyrou, S. M., and Christophorou, L. G., J. Chem. Phys. 82, 1048 (1985c).

Spyrou, S. M., Sauers, I., and Christophorou, L. G., J. Chem. Phys. 78, 7200 (1983).

Tauchert, W., Jungblut, H., and Schmidt, W. F., Can J. Chem. 55, 1860 (1977).

Yamaguchi, Y. I., Nakajima, T., and Nishikawa, M., J. Chem. Phys. 71, 550 (1979).

Younglove, B. A., and Ely, J. F., J. Phys. Chem. Ref. Data 16, 577 (1979).

Wadehra, J.M., Phy. Rev. A 29, 106 (1984).

Wang, J. S., and Franklin, J. L., Int. J. Mass Spectrom. 78, 7200 (1980).

Warman, J. M., Fessenden, R. W., and Bokale, G., J. Chem. Phys. 57, 2702 (1972).

Warman, J. M., and Sauer, M. C. Jr., Int. J. Radiat. Phys. Chem. 3, 273 (1971).

Weber, L. A., J. Chem. Phys. 65, 446 (1976).

Wegener, P. P., In Molecular Beams and Low Density Gasdynamics. New-York: Marcel-Dekker, 1974.

Wigner, E., Seitz, F., Phys. Rev. 34, 804, 1933.

Vita

Panagiotis G. Datskos was born in Larissa, Greece, on August 8, 1961. He graduated from high school in June, 1979. The following September he entered the Physics and Mathematics School of the University of Ioannina. He received a degree in Physics from that university in June, 1983.

In September, 1983 he entered the Graduate School of The University of Tennessee in Knoxville and received the Doctor of Philosophy degree in Physics in December, 1988.